

UNDERSTANDING SPACE WEATHERING OF ASTEROIDS AND THE LUNAR
SURFACE: ANALYSIS OF EXPERIMENTAL ANALOGS AND SAMPLES FROM
THE HAYABUSA AND APOLLO MISSIONS

by

Michelle Susan Thompson

Copyright © Michelle Thompson 2016

A Dissertation Submitted to the Faculty of the

DEPARTMENT OF PLANETARY SCIENCES

In Partial Fulfillment of the Requirements

For the Degree of

DOCTOR OF PHILOSOPHY

In the Graduate College

THE UNIVERSITY OF ARIZONA

2016

THE UNIVERSITY OF ARIZONA
GRADUATE COLLEGE

As members of the Dissertation Committee, we certify that we have read the dissertation prepared by Michelle Thompson, titled Understanding Space Weathering of Asteroids and the Lunar Surface, and recommend that it be accepted as fulfilling the dissertation requirement for the Degree of Doctor of Philosophy.

Thomas J. Zega Date: May 27, 2016

Shane Byrne Date: May 27, 2016

Dante S. Lauretta Date: May 27, 2016

Peter W. Reiners Date: May 27, 2016

Timothy D. Swindle Date: May 27, 2016

Final approval and acceptance of this dissertation is contingent upon the candidate's submission of the final copies of the dissertation to the Graduate College.

I hereby certify that I have read this dissertation prepared under my direction and recommend that it be accepted as fulfilling the dissertation requirement.

Dissertation Director: Thomas J. Zega Date: May 27, 2016

STATEMENT BY AUTHOR

This dissertation has been submitted in partial fulfillment of the requirements for an advanced degree at the University of Arizona and is deposited in the University Library to be made available to borrowers under rules of the Library.

Brief quotations from this dissertation are allowable without special permission, provided that an accurate acknowledgement of the source is made. Requests for permission for extended quotation from or reproduction of this manuscript in whole or in part may be granted by the head of the major department or the Dean of the Graduate College when in his or her judgment the proposed use of the material is in the interests of scholarship. In all other instances, however, permission must be obtained from the author.

SIGNED: Michelle Thompson

ACKNOWLEDGEMENTS

The road to a Ph.D. is long, and often feels like a solitary journey. In reality, there are many travelers who walk the road with you, supporting and encouraging you.

For me, the most constant companions have been my parents. For my Mom and Dad, who have been telling me for so long that I could be anything I wanted to be, that I never imagined I couldn't. You have been there every step of the way, helping me to achieve more and pushing me to be the best I can be. I wouldn't be where I am without you, and I love you. The dedication you taught me is in every page of this work. Thank you to my sisters and my brother, who inspire me every day with their own hard work and commitment. Thank you for the laughs, the love, and for always keeping me humble. Your pride and belief in me fills my heart and motivates me every day. I couldn't have done it without you.

Thank you to my friends at home and abroad, who have been understanding of me moving across the world in pursuit of this goal. Thanks for still trying to see me whenever you can, and for listening to me talk about boring space stuff. I appreciate you all. Especially, to Becky, for always being there, and to Lauren, for always listening.

Thank you to those who put me on this journey in the first place. Ron Peterson at Queen's and Kim Tait at the ROM, thanks for giving me my first opportunity and showing me what it meant to learn. Thank you to Sarah, Lindsay, and Roy. Sarah, you have inspired me more than you know. Lindsay, you are a true friend, and I couldn't have made it through the past five years without all that beer you bought me. Roy, I think we changed each other's lives, and as much as you will deny it, you got me here. When I first met you all, I didn't know I was finding a new family, but I'm so glad that I did.

For my comrades at LPL, we struggled together, and at times you were the only ones keeping me going. I have never met a group of people more brilliant, and each of you inspires me every day. You make me look forward to a lifetime of this work by being more than just colleagues, but my best friends. Thank you for everything, especially the manatee. To Kelly, there were times when I didn't think we would make it, but we started and finished this thing together. Thank you for your friendship.

Finally, I want to thank my adviser, Tom. I am proud to be your first student, and I think we both agree that you should probably quit now because you'll never find another one quite like me. You are the best teacher, mentor, advocate, and friend I could have asked for. While I might have been able to do it without you, I wouldn't have wanted to. Thank you for being my partner in this work and for inspiring me to be a better scientist.

To those who will come after, be encouraged, there are good things waiting at the end of the road.

DEDICATION

*For Canada, the homeland that bore me, raised me,
and shaped me into the person I am today.*

*It may feel as though I have left you in the pursuit of this dream,
but in reality, you are with me every day. You are in my blood
and my heart, the true north, strong and free.*

TABLE OF CONTENTS

LIST OF FIGURES	8
LIST OF TABLES	9
ABSTRACT	10
CHAPTER 1: INTRODUCTION	13
1.0 Introduction	13
1.1 Space Weathering Processes	14
1.2 Space Weathering Features	17
1.3 Optical Properties of Space Weathered Soils	24
1.4 Experimental Simulations of Space Weathering	27
1.5 Scope of this Work	31
CHAPTER 2: METHODS	34
2.1 Introduction	34
2.2 Sample Preparation	34
2.3 Image Formation	41
2.4 Electron Scattering	43
2.5 Selected Area Electron Diffraction	45
2.6 Energy-Dispersive X-Ray Spectroscopy	47
2.7 Electron Energy-Loss Spectroscopy	50
2.8 In Situ Heating	53
CHAPTER 3: MICROCHEMICAL AND STRUCTURAL EVIDENCE FOR SPACE WEATHERING IN SOILS FROM ASTEROID ITOKAWA	56
3.1 Introduction	56
3.2 Methods	59
3.3 Results	60
3.4 Discussion	68
3.5 Conclusions	75
3.6 Acknowledgements	75
CHAPTER 4: THE OXIDATION STATE OF NANOPHASE Fe PARTICLES IN LUNAR SOIL: IMPLICATIONS FOR SPACE WEATHERING	77
4.1 Introduction	78
4.2 Samples and Methods	81

TABLE OF CONTENTS – *Continued*

4.3 RESULTS	88
4.4 DISCUSSION	99
4.5 CONCLUSIONS	110
4.6 ACKNOWLEDGEMENTS	111
 CHAPTER 5: IN SITU EXPERIMENTAL FORMATION AND GROWTH OF NpFe PARTICLES AND VESICLES IN LUNAR SOIL	 112
5.1 Introduction	113
5.2 Methods	117
5.3 Results	120
5.4 Discussion	130
5.5 Conclusions	140
5.6 Acknowledgements	140
 CHAPTER 6: SUMMARY, IMPLICATIONS, AND FUTURE WORK	 141
6.1 Summary	141
6.2 Implications and Future Work	143
 APPENDIX A: CAMERA CONSTANTS DETERMINED FOR JEOL 2010 AT ASU	 147
 APPENDIX B: LINEAR, LEAST-SQUARES FITTING PROGRAM	 149
 APPENDIX C: HAPKE REFLECTANCE MODEL OF THE OPTICAL EFFECTS OF SPACE WEATHERING ON LUNAR SOILS	 161
 APPENDIX D: LIST OF PUBLICATIONS	 173
D.1 Peer-Reviewed Publications	173
D.2 Conference Abstracts	173
 REFERENCES	 176

LIST OF FIGURES

2.1 Trimming of the epoxy bullet	35
2.2 Slicing of the epoxy bullet	37
2.3 Images of TEM grids	38
2.4 Preparing a FIB section	39
2.5 Ray diagram of the TEM	42
2.6 Indexing a diffraction pattern	46
2.7 Example EDS spectrum	49
2.8 Schematic of TEM and EELS spectrometer	51
2.9 Example EELS spectrum showing ZLP, Low- and High-Loss Regions	52
2.10 Example EELS spectrum for Fe $L_{2,3}$ core-loss edge	53
2.11 Schematic of Hitachi heating chip	54
3.1 TEM data for particle RA-QD02-0042-02	61
3.2 TEM data for orthopyroxene and plagioclase rims	63
3.3 TEM and EDS data for multilayer rims in orthopyroxene	64
3.4 TEM and EDS data for other space weathering features	66
3.5 TEM and EDS data for nanophase Fe particles	67
4.1 STEM imaging and EELS spectra for nanoparticles in lunar soil	89
4.2 Quantified EELS spectra of nanoparticles	90
4.3 Ternary plot of nanoparticle compositions	92
4.4 TEM data for a core-shell nanoparticle	94
4.5 STEM images of hollow nanoparticles	95
4.6 High resolution STEM images of nanoparticles	96
4.7 Simulated reflectance spectra of lunar soil	98
5.1 TEM data of slow heating experiments of lunar soil grains	122
5.2 TEM and EDS data of grains that underwent slow heating	123
5.3 TEM data from grains that underwent single thermal shocks	124
5.4 TEM and EDS data of nanoparticles	125
5.5 TEM data for grain 79221-R2	126
5.6 TEM data for grain 79221-R1	127
5.7 Particle size distributions for npFe grains in 79221-R1 and -R2	127
5.8 TEM and EELS data for npFe particles	129
5.9 Quantified EELS spectrum for an npFe particle	130
A1 Comparison of 2013 and 2015 Camera Constants	148

LIST OF TABLES

4.1 Measured d -spacings of npFe in lunar soil	97
A1 2013 Camera Constants for Image Size 2688 x 2672 px	147
A2 2015 Camera Constants for Image Size 1344 x 1336 px	147
A3 2015 Camera Constants for Image Size 2688 x 2672 px	147

ABSTRACT

Grains on the surfaces of airless bodies are continually being modified due to their exposure to interplanetary space, a phenomenon known as *space weathering*. This dissertation uses a multi-faceted approach to understanding space weathering of the lunar and asteroidal surfaces. Chapters 1 and 2 provide an introduction to space weathering and a discussion of the methods employed in this work, respectively.

Chapter 3 focuses on the analysis of returned samples from near-Earth asteroid Itokawa using the transmission electron microscope (TEM) and contributes to the first-ever comparison of microstructural and chemical features of space weathering in returned samples from two different airless bodies. This research uses high-resolution imaging and quantitative energy-dispersive x-ray spectroscopy (EDS) measurements to analyze space weathering characteristics in an Itokawa soil grain. These analyses confirm that space weathering is operating on the surface of Itokawa, and that many of the resulting features have similarities to those observed in lunar soils. Results show that while there is evidence that both major constituent space weathering processes are operating on the surface of Itokawa, solar wind irradiation, not micrometeorite impacts, appears to be the dominant contributor to changes in the microstructure and chemistry of surface material.

Chapter 4 presents a detailed study of nanophase Fe (npFe) particles in lunar soil samples. For the first-time, the oxidation state of individual npFe particles was directly measured using electron energy-loss spectroscopy (EELS) in the TEM. The results show that npFe particles are oxidizing over their time on the lunar surface, and that the amount of oxidized Fe in the nanoparticles is correlated with soil maturity. The EELS data are also coupled to atomic-resolution imaging, which is used to determine the structure of the

nanoparticles, confirming their mineral phase. This work challenges the long-standing paradigm that all npFe particles are composed of metallic Fe and that the chemical composition of these features remains static after their formation. A theoretical modeling investigation of the influence that npFe particles of different oxidation states have on the spectral properties of the material is also presented. The model results show that varied Fe-oxidation states of the nanoparticles can produce subtle changes in the optical properties of the soils, including the degree of reddening and the attenuation of characteristic absorption bands. These findings should be accounted for in future modeling of reflectance spectra.

Chapter 5 presents a novel technique for simulating space weathering processes inside the TEM. Using an in situ heating holder, lunar soils were subjected to both slow- (~minutes) and rapid-heating (<seconds) events to simulate micrometeorite impacts. The slow-heating experiments show that npFe forms at ~575 °C, providing a temperature constraint on initial npFe formation. Lunar soil grains that were subjected to a single, rapid, thermal pulse show the development of npFe particles and vesiculated textures near the grain rim. The vesicles were imaged and the npFe particles were imaged and then mapped with EDS. The oxidation state of the npFe particles was confirmed to be Fe⁰ using EELS. Several lunar soil grains were subjected to multiple thermal shocks to simulate longer exposure times on the lunar surface. With each heating cycle, the number and size distribution of the npFe particles changed. The average size of npFe particles increased, and the size distribution became more gaussian after multiple heating events, versus the asymmetric distribution present after only one heating event. These results

provide insight into the particle growth dynamics for space weathered soils and could offer a new way to place relative age constraints on grains in lunar soil.

Chapter 6 provides a summary of the work presented here, discusses its implications for understanding space weathering processes across the solar system, and presents a perspective on the future of space weathering studies.

CHAPTER 1

INTRODUCTION

1.0 Introduction

Grains on the surfaces of airless bodies are continually being modified due to their exposure to interplanetary space, a process known as *space weathering*. Several individual mechanisms contribute to this alteration of surface material on planetary bodies, including: micrometeorite impacts, the interaction of surface material with energetic particles from the solar wind and galactic cosmic rays, comminution of material and the formation of agglutinate particles through impact events, and the rate of resurfacing on planetary bodies (Hapke 2001). Each of these processes can alter the morphology, microstructure, and chemistry of grains on airless body surfaces. The features that develop as a product of space weathering manifest in surface soils on macro- to atomic-scales. These changes, in turn, effect the optical properties of surface materials, which are observed with remote sensing spacecraft and telescopes (Hapke 2001; Hapke et al. 1975). As a result, the effects of space weathering impact our ability to determine and understand the chemical composition of planetary surfaces from remote sensing data. Similarly, space weathering processes are theorized to contribute to the discrepancies between meteorite reflectance spectra and their asteroidal parent bodies, complicating the matching meteorite samples to their sources, e.g., ordinary chondrites and S-type asteroids (Binzel et al. 1996). Investigations into the nature of space weathering processes are typically performed in three ways: (1) through the analysis of returned samples from airless bodies for microstructural and chemical characteristics of these processes; (2) by

experimentally simulating space weathering processes in the laboratory and subsequently analyzing the resultant analog materials; and (3) through measurements and modeling of reflectance properties for both returned and experimentally generated samples. Each of these techniques provide a new perspective on space weathering and are fundamental for understanding the evolution of airless body surfaces and their surface mineralogy from remote sensing data.

1.1 Space Weathering Processes

The factors that drive space weathering processes vary significantly across the solar system. As such, the nature and concentration of the resultant features that develop in grains on airless body surfaces and the rate at which they form also varies. Each of the major constituent weathering mechanisms is described below.

1.1.1 Micrometeorite Bombardment

Micrometeorite impacts on airless body surfaces cause melting and vaporization of target material, and its subsequent recondensation on local grain surfaces, which can result in chemical differentiation (Hapke 2001). The flux and average impact velocity of micrometeorites varies across the solar system. In the asteroid main belt, the flux of impactors is higher than at 1 AU, but the impact velocity is lower (~5 km/s compared to ~15 km/s) (Bottke et al. 1994; Cintala 1992). These impact fluxes have been measured by dust detectors aboard various spacecraft traveling through the inner solar system (Grün et al. 1991). Lower velocity impacts have a reduced ability to generate melt or vapor

products, but can still cause the mechanical breakdown or comminution of surface material (Cintala 1991; Heiken et al. 1991).

1.1.2 Solar Wind Irradiation

Energetic ions from the solar wind, predominantly H^+ and He^+ at energies of ~1 keV and 4 keV, respectively, are implanted into surface material, causing amorphization on the outer ~100 nm of surface grains (Bradley et al. 1996; Keller and McKay 1997). Solar wind irradiation can also cause preferential sputtering of material from grain surfaces where sputtered atoms may recondense on adjacent regolith grains (Christoffersen et al. 2012; Hapke 2001). Higher energy particles resulting from solar flares penetrate deeper into surface soils, between 1 mm to 1 cm, creating a path of ionization damage in the solids they interact with, known as solar flare tracks (Blanford et al. 1975). The solar wind intensity decreases as a function of distance ($\sim 1/R^2$) from the Sun, and so the location of the airless body in the solar system affects the resulting solar wind damage its grains experience.

1.1.3 Comminution

Grains on the surfaces of airless bodies are mechanically broken down over time. This process can be driven by micrometeorite impacts and by thermal weathering of material resulting from diurnal temperature cycling (Heiken et al. 1991). The comminution of material exposes new, fresh surfaces of grains to space weathering processes and changes the size distribution of grains in airless body soils as a function of exposure time.

1.1.4 Agglutinate Formation

Agglutinate particles are aggregates of mineral fragments bonded together with glassy material. They are formed as a product of melting and mixing of material during micrometeorite impacts (Heiken et al. 1991). The agglutinate glass is typically quenched before it can chemically homogenize or form long-range order to become crystalline. Agglutinates can compose a large proportion of lunar soils (up to 60% by volume) and often exhibit nanophase Fe particles (discussed below) which affect the optical properties of lunar soil material (Heiken et al. 1991).

1.1.5 Resurfacing

Resurfacing reduces the exposure time of surface soils, which decreases the accumulation of space weathering effects in grains. Small bodies such as near-Earth asteroids may experience higher resurfacing rates due to gravitational perturbations from planetary close approaches, impact-induced seismic shaking, or YORP spinup (Keane and Matsuyama 2013, Connolly Jr. et al. 2015). Lower surface gravity on these bodies, as opposed to the Moon, may increase the frequency of grain escape due to these impact events, reducing the exposure of grains on the surface.

Grain morphologies also change as a result of space weathering processes. Communitation mechanically breaks down material and exposes fresh surfaces, creating angular grains, whereas impact events cause melting and may serve to make grains more rounded and/or spherical. In addition to melting, other processes can serve to round surface grains. Recent analyses of samples from asteroid Itokawa show that some rounded grains have young CRE ages, suggesting short surface exposure times (Connolly

et al. 2015). The grains may have become rounded in recent YORP resurfacing events or tidal encounters which are driving regolith gardening events.

Each of these space weathering processes is operating continuously and simultaneously on the surfaces of airless bodies. The effect or efficiency of many of these mechanisms depend on the initial chemical composition and crystal structure of grains on the surface. These properties affect, e.g., the radiation hardness of grains or the relative volatility of material and its likelihood to recondense during a melting or vaporization event. As a result, the types of space weathering features that develop and their prevalence are tied to the target material (Hapke 2001). Consequently, the changes to soil optical properties also vary accordingly. The proportional contribution of each constituent process to overall space weathering across different types of planetary surfaces is not well known.

1.2 Space Weathering Features

Space weathering features were initially recognized by studying returned samples, particularly in the fine size fraction of lunar soils returned by the NASA Apollo missions (Keller and McKay 1995; Keller and McKay 1993, 1997; Keller et al. 1998; Taylor et al. 2001; McKay et al. 1991). Since this discovery, similar characteristics have since been identified in lunar brecciated meteorites and asteroidal brecciated meteorites (Noble et al. 2005; Noble et al. 2011). Most recently, space weathering features have been identified in returned soil grains from near-Earth asteroid Itokawa by the Japanese Aerospace Exploration Agency (JAXA) Hayabusa mission (Keller et al. 2016; Keller and Berger 2014; Noguchi et al. 2014; Noguchi et al. 2011), in part through the work presented here

in Chapter 3 (Thompson et al. 2014). Space weathering processes, described in section 1.1, result in both microstructural and crystal chemical changes in surface samples. Understanding the nature of these characteristics requires a technique that is capable of providing information on chemistry and crystal structures of materials down to the atomic scale: transmission electron microscopy (TEM). Studies of space weathering features typically use TEM to identify individual features that result from these processes, including returned samples from the Moon and Itokawa, brecciated meteorites, and experimentally space weathered materials. The results of these analyses are described below.

1.2.1 Partial and Complete Amorphization

Solar wind irradiation causes the disruption of the crystal structure in materials on airless body surfaces. Implanted H^+ and He^+ ions break down long range atomic order and create zones of either partial or complete amorphization on the outer rims of surface grains. The thickness of these rims and the degree of amorphization is dependent upon the exposure time the material has experienced, and the inherent radiation hardness of the target material (Christoffersen et al. 2010; Christoffersen and Keller 2011; Keller et al. 2016). The rims may extend a uniform depth into the sample, or appear as irregular, undulating interfaces with underlying crystalline material. The amorphization extends <100 nm into the grain surface, which is the penetration depth for ions with typical solar wind energies (Thompson et al. 2014). These amorphous zones typically do not show any chemical differentiation in major elements relative to the underlying crystalline material, only a loss of long-range order. They may occur in localized regions of the grain rim, not

necessarily across the entire three-dimensional surface of the grain, depending on the particle's exposure history. These features were reported in both lunar soils and grains from Itokawa, as well as analog samples subjected to experimental space weathering conditions.

1.2.2 Chemically Heterogeneous Rim Deposits

Many grains that have experienced space weathering exhibit amorphous or nanocrystalline deposits on the grain surface that are chemically distinct and sit in topographic relief from the underlying material (Keller and McKay 1993, 1997; Thompson et al. 2014). These regions of the grain rim may contain constituent elements not native to the mineral/glass substrate on which they are hosted. Chemically and structurally heterogeneous grain rims have been attributed to several space weathering processes. They may form as a result of redeposition of sputtered material that has been removed from the surface of an adjacent grain through irradiation processes. This sputtering may result in the preferential loss of constituent volatile elements, in particular, oxygen, creating a relatively reduced vapor deposit and sputtered surface as a result. If there is a compositional difference between the sputtered surface of a grain, and the grain where the sputtered vapor material is subsequently redeposited, an amorphous or nanocrystalline rim that is chemically distinct from the underlying material will be formed (Keller and McKay 1997). In addition to radiation processes, chemically and structurally heterogeneous rims may form through micrometeorite bombardment processes as well. If an impact event melts or vaporizes material from a soil grain with different composition from its neighbors, this vapor or melt may be deposited onto an

adjacent grain, where it is quenched before it can become crystalline. This will result in vapor deposited rims, or melt splashes on grain rims resulting from impact events. The deposits can range between a few nm to several 10s of nm in thickness. These features have been reported in returned samples from the Moon and Itokawa, and in experiments performed to simulate both solar wind irradiation and micrometeorite impacts (Christoffersen and Keller 2011; Keller and McKay 1993, 1997; Noguchi et al. 2014; Noguchi et al. 2011; Thompson et al. 2014; Zhang and Keller 2010).

1.2.3 Vesiculated Textures

Vesicles are theorized to develop either through solar wind irradiation or through ion implantation in correlation with a heating event. H^+ and He^+ ions in the material, implanted by the solar wind, are thought to coalesce to form voids or bubbles in the grain rims of surface samples. These features have been reported in lunar soils and are also pervasive in samples returned from Itokawa (Matsumoto et al. 2015a; Matsumoto et al. 2015b; Noguchi et al. 2014; Thompson et al. 2014). Vesicles between 5 to 30 nm in size were detected in the outer 50 nm of the rims of Itokawa grains as seen in cross section, as well as being visible on grain surfaces. Vesiculated textures have also been identified in lunar and asteroidal regolith brecciated meteorites (Noble et al. 2005; Noble et al. 2011). Vesicles have also developed in experimental analog samples subjected to high doses of irradiation.

1.2.4 Solar Flare Tracks

High-energy particles resulting from solar flares cause tracks of ionization damage in surface soils. The density of solar-flare tracks in returned samples correlates with exposure time. A production rate for these tracks at 1 AU has been calculated by analyzing lunar rock samples whose age was determined through independent dating methods, and is estimated to be $6 \times 10^5 \text{ year}^{-1} \text{ tracks/year/cm}^2$ (Blanford et al. 1975). By measuring the density of solar flare tracks in lunar soil grains, their exposure time on the surface can be estimated, and this method has recently been expanded for use in Itokawa samples (Keller et al. 2016). Solar-flare tracks have been observed in returned samples from the Apollo missions and Hayabusa samples.

1.2.5 Grain Surface Features

Several features consistent with micrometeorite impact events have been observed in secondary electron imaging on the surfaces of whole grains returned from both the Moon and asteroid Itokawa. These include nano- and microcraters exhibiting melt ejection rims, molten splashes, and adhering particles that exhibit a size distribution consistent with collisional disruption (Nakamura et al. 2012; Heiken et al. 1991).

1.2.6 Nanophase Iron Particles

Nanophase iron particles, npFe, typically range in size from a few nm to >100 nm (Heiken et al. 1991; Morris 1980). NpFe particles have been identified in lunar soils and samples returned from Itokawa, and in minor concentrations in asteroidal brecciated meteorites (Keller and McKay 1997; Noble et al. 2011; Noguchi et al. 2014; Thompson

et al. 2014). The composition of nanoparticles in lunar soils appear to be primarily Fe, whereas there is S and Mg associated with many nanoparticles observed in Itokawa samples (Noguchi et al. 2014; Noguchi et al. 2011). The Fe is traditionally thought to be metallic Fe, or an oxidation state of Fe^0 , due to the reducing nature of airless body surfaces (Hapke 2001; Keller and Clemett 2001). This topic will be revisited in detail in Chapter 4.

NpFe particles are produced in surface samples through several space weathering processes. One such proposal is that hydrogen (H^+) is implanted into soils by solar-wind irradiation and functions as a reducing agent for Fe in the crystal structure during the melting or vaporization of a micrometeorite impact event (Hapke 2001). NpFe particles in agglutinate grain interiors may be formed through this mechanism. However, Fe nanoparticles also occur in amorphous rims of plagioclase grains, which have no native Fe that could otherwise be reduced, suggesting other processes must be occurring on airless body surfaces to develop npFe (Keller and McKay 1997).

As discussed previously, the ion-irradiation of surface grains results in sputtering and redeposition of material onto adjacent grains. If O atoms are preferentially sputtered, a localized reducing environment is created on the surface of the particle, which can cause the Fe in the residual material to become reduced. If the O, which has a low sticking coefficient, does not adhere to any adjacent surfaces, it may be lost from the system. Consequently, if cations from the target are sputtered and redeposited onto that adjacent surface, another reducing environment is created on the target substrate, causing the reduction of redeposited Fe and the formation of nanoparticles (Hapke 2001).

Similarly, oxide molecules are vaporized in the target material during an impact event, e.g., SiO, MgO, FeO. In this vapor cloud, FeO molecules have the lowest binding energy and consequently dissociate, resulting in independent Fe and O atoms (Hapke 2001). O, being the more volatile species, will prefer to stay in the vapor, whereas Fe will condense as nanoparticles in the surrounding glassy matrix. Each of these mechanisms is likely producing npFe grains in airless body surface samples.

The concentration of metallic npFe particles in lunar soil grains has been measured using the ferromagnetic resonance (FMR) technique (Morris 1978). The FMR intensity of a lunar soil, I_s on an arbitrary scale, is correlated to the presence of npFe. This measurement has been used to develop a maturity index for lunar soils, related to their exposure time on the lunar surface. Soils are classified as mature, submature, or immature, with more npFe grains in mature samples, resulting in a higher I_s value (Morris 1978). The concentration of npFe is assumed to increase with exposure time, as the grains have had longer time to experience the processes described above. Mature grains have more implanted H to behave as a reducing agent during melting or vaporization events and also have had longer exposure time increasing the likelihood of experiencing impact events and sputtering of material via irradiation. In addition, a higher initial Fe concentration in a soil would allow for the eventual production of more npFe particles. In order to standardize this maturity index across different soil compositions, the scale uses I_s/FeO values, where FeO represents the total Fe content of the soil. I_s/FeO values of 0-30 units are classified as immature, 30-60 are submature, and >60 are mature soils (Morris 1978).

Changes in the optical properties that are characteristic of space weathered soils are caused by the development of nanophase Fe particles. The contributions that npFe have to reflectance spectra of soils on airless bodies has been shown experimentally and through theoretical modeling, e.g., Hapke (2001).

1.3 Optical Properties of Space Weathered Soils

Space weathering was initially identified as an airless body surface process by studying the spectral evolution of excavated material surrounding recent craters on the Moon. Craters that were determined to be young based on stratigraphic relationships often had characteristic ‘rays’ of bright reflective material, relative to the surrounding landscape, radiating from the central basin feature. Older craters were surrounded by material with uniform reflectance properties, indicating processes were operating to darken fresh material on the lunar surface (Gold 1955). Comparing the ages of known craters to the optical maturity of the freshly excavated and preexisting weathered surface material indicates that the rate the material space weathers is dependent on several factors, e.g., crater size and shape and geologic setting/material composition (Lucey et al. 2000). This work showed that the optical maturation of surface material saturates close to ~900 Ma.

Space weathering was confirmed, later, when samples were returned by the Apollo missions. The reflectance spectra of lunar soil did not match those of pulverized material from lunar rocks of the same composition, but were indeed much darker than the interior of a rock that had not experienced exposure to interplanetary space (Conel and Nash 1970; Gold et al. 1970; Hapke et al. 1970).

The darkening, or reduction in intensity, of the overall reflectance spectrum of weathered soils is evident in the high UV, visible, and near-IR wavelengths (0.2 μm to 2 μm). In addition to darkening, space weathering processes cause soil spectra to redden, which increases their reflectance at longer wavelengths. Finally, characteristic absorption bands are attenuated as a result of the production of nanophase Fe. Most notable among these absorption bands is the 1.0 μm silicate feature which is caused by the excitation of an Fe^{2+} atom in that is in a coordinated environment with 6 oxygen atoms, a very common structure in silicate mineral structures, e.g., pyroxene (Hapke 2001). During the formation of npFe particles, through the processes described above, Fe^{2+} atoms are reduced to Fe^0 , making them ineffective photon absorbers at the 1.0 μm wavelength, resulting in attenuation of this absorption band (Hapke 2001). Each of these changes to the optical properties of surface soils makes it difficult to determine their composition from remote sensing spacecraft spectrometers.

Space weathering processes have been proposed to explain the resulting spectral differences between Q- and S-type asteroids, the former type thought to be fresh and the latter their weathered counterparts. While the link between S-type asteroids to ordinary chondrites was confirmed via returned samples from the Itokawa mission, Binzel et al. (2001) successfully matched the Itokawa spectrum most closely to reddened LL chondrites using spectral modeling techniques.

1.3.1 Theoretical Modeling of Space Weathering Effects on Soil

The effect of npFe particles on soil reflectance spectra has been investigated through theoretical modeling and experimental techniques, the former of which will be

described in section 1.4. Hapke developed a methodology for simulating a reflectance spectrum based on the optical characteristics, e.g., the absorption coefficients, of a material (Hapke 2001, 2012). This technique allows for the addition of different proportions of nanometer-sized Fe particles to the surfaces of grains composed of an unweathered substrate material, e.g., a mixture of glass and mineral fragments representing the average composition of lunar soils. The overall optical properties of this new, weathered material are then used to generate a theoretical reflectance spectrum, which has shown to be similar to measured spectra from returned samples. The amount, by volume, of npFe that is added to the simulated fresh sample spectrum in order to mimic weathered materials is between 0.1 to 2%, depending on the maturity of the target soil (Hapke 2001). This modeling technique was successfully employed in this work, as discussed in Chapter 4.

Hapke's work showed that npFe particles can cause the changes to reflectance spectra observed in weathered returned samples. However, the scattering principles that guide this methodology are only applicable for the very finest size fraction of npFe particles, preventing simulated spectra from matching real observed spectra at all wavelengths. Simulations deviate from measured spectra in particular at longer wavelengths, towards the near-IR regime, where the models are often more red than the natural samples. Lucey and Noble (2008) improved on the Hapke model by including the effects of Mie scattering, which are relevant for larger inclusions, such as npFe grains in the tens to hundreds of nm size range, commonly found in agglutinate particles. This Hapke-Mie hybrid methodology provides a better match for reflectance spectra between simulated and real soils at longer wavelengths. In addition to this theoretical modeling

work, experimental simulations have been completed in the laboratory to understand how the chemical and structural characteristics, and in turn, the optical properties, evolve in airless body surface samples as a result of space weathering processes.

1.3.2 Combining Spectral Analyses with Geological Interpretation

Spectral studies of asteroidal surfaces using remote sensing spacecraft enable the investigation of surface composition and geologic processes, including space weathering, that occur on airless bodies. Spectral analyses of the Psyche crater on Asteroid Eros by the NEAR mission showed differences in brightness between regions of high (bright) and low (dark) slope of the crater wall (Clark et al. 2001), thought to be attributed to differences in exposure of the material to space weathering processes. The variations in albedo were shown to be a product of the exposure of fresh, unweathered surfaces, likely through downslope movement of material in steeper areas of the crater wall. These observations provided further evidence for the effect of space weathering processes on the spectral properties of surface material. Additionally, those remote sensing results also highlight the complex nature of airless body surfaces, which are being shaped by an intimate interplay of processes including both terrestrially-analogous geologic processes, like mass-wasting, and phenomena specific to airless bodies, such as space weathering.

1.4 Experimental Simulations of Space Weathering

Several techniques for simulating space weathering processes in the laboratory were developed in order to understand the changes in chemical and microstructural characteristics, and as a result, optical properties, occurring in soils on the surfaces of

airless bodies. These experiments simulate the two space-weathering processes thought to be the most important: solar wind irradiation and micrometeorite impacts.

1.4.1 Ion Irradiation Simulations of Solar Wind Bombardment

The solar wind is composed primarily of energetic H^+ and He^+ ions with 1 keV/amu. The flux for the solar wind at 1 AU is 4.1×10^8 ions/cm²/s (Loeffler et al. 2009; McFadden et al. 2006). These ions bombard airless body surfaces and cause irradiation damage through amorphization of crystalline materials. Ion irradiation has been performed in the laboratory using a variety of ion species and energies, some more appropriate simulants for solar wind than others. These experiments include 1 keV H^+ , 4 keV He^+ irradiations and higher energy Ga and Ar ions. These experiments are typically performed under vacuum, using a variety of substrates including individual mineral slabs or meteorite samples, and simulate total doses between 10^{16} to 10^{18} ions/cm², after which the spectral effects appear to be saturated in the near-IR wavelength regime (Christoffersen et al. 2012; Dukes et al. 1999; Keller et al. 2015; Loeffler et al. 2009; Yamada et al. 1999). Ion irradiation is often coupled to reflectance spectroscopy measurements to observe the reddening and darkening of the sample with continued exposure, and these results have suggested that experiments accurately replicate the spectral trends we observe in naturally space weathered samples, as discussed above. Unfortunately, ion irradiation experiments are often not coupled to microstructural and chemical characterization. In addition to analyzing spectral changes, obtaining a fundamental knowledge of the chemical and structural changes as well are important for understanding space weathering processes as a whole. Recent TEM work was performed

on irradiated samples and has shown the development of vesiculated textures, the reduction of oxidized Fe in the material and the formation of nanoparticles, and amorphization of crystalline material (Christoffersen et al. 2012; Keller et al. 2015). These results indicate that ion irradiation is generating features similar to what is expected in naturally space weathered samples, including those analyzed here.

1.4.2 Pulse-Laser Irradiation

In contrast with ion irradiation experiments, simulating micrometeorite impacts inside the laboratory presents a different set of challenges. Impacts on the surfaces of airless bodies such as the Moon occur at high velocities (15-20 km/s), which are difficult to replicate in the laboratory. As a result, two distinct techniques were developed to provide analogous processes to impact events: pulse-laser irradiation, discussed here, and light-gas gun impacts, described in section 1.4.3.

Pulse-laser irradiation experiments bombard an analog sample, typically a mineral or meteorite, with short-duration laser pulses lasting <10 nanoseconds (Christoffersen et al. 2016; Gillis-Davis et al. 2015; Gillis-Davis et al. 2013; Sasaki et al. 2001; Yamada et al. 1999). The energy imparted by the laser is equated to the energy transferred to a particle during a micrometeorite impact event, assuming an impactor of a certain size and velocity. This technique has successfully reproduced the spectral characteristics, both reddening and darkening, that are observed in naturally space-weathered materials (Sasaki et al. 2001). The number of laser shots can be equated to exposure timescales for airless body surfaces, assuming a known impactor flux at a specific location. In addition to spectral characterization, some samples subjected to

pulse-laser irradiation have also been analyzed for chemical and microstructural changes using TEM. These investigations have revealed the development of npFe particles as a result of the irradiation, ranging in size from a few nm to over 100 nm in size (Christoffersen et al. 2016; Sasaki et al. 2001). In addition to Fe nanoparticles, these samples show the development of melted and glassy material. While the energy deposited into the sample through pulse-laser deposition is equivalent to that of a micrometeorite impact, there is a limited understanding of the physical mechanisms that are generating the space weathering features observed microstructurally and spectrally, e.g., the temperature change experienced by the sample.

1.4.3 Light-Gas Gun Impacts

A second methodology for simulating micrometeorite impact events is using a light-gas gun impactor. This technique accelerates a projectile at high velocities, up to 5 to 7 km/s, at a target material that can be retrieved after impact for analysis (Cintala et al. 2015). These velocities are appropriate for impact velocities in the asteroid belt, though are significantly slower than those occurring at 1 AU for e.g., the Moon or near-Earth asteroids. The resultant products have been characterized chemically and microstructurally and show the development of several features consistent with space weathering, including glassy melted regions similar to lunar agglutinate particles (Christoffersen et al. 2013).

While these experimental techniques have associated limitations, each has provided immense insight into our understanding of how space weathering processes operate on airless body surfaces. Work presented in Chapter 5 builds on these

experiments, offering a new methodology for simulating micrometeorite impact events in the laboratory.

1.5 Scope of this Work

While the community has made significant advances in our understanding of space weathering, many aspects of this phenomenon remain poorly understood. Until the recent return of the Hayabusa mission, we were unable to analyze space weathering features in returned samples from an airless body other than the Moon. How does space weathering vary across the inner solar system? What does space weathering look like on Itokawa or on other asteroids? Were the microstructural and chemical characteristics similar or did they vary across different planetary surfaces? What can the detailed chemical and structural analysis of space weathering features tell us about these processes? Can we gain new insight into space weathering by analyzing characteristics in returned samples at the nanoscale with techniques not previously possible? Are there novel methods for simulating space weathering in the laboratory? Is it possible to provide a more detailed understanding of the chemical and microstructural changes that result from space weathering processes through these simulations?

The above questions provided the motivation for my research. The goal of this work was to provide insight into how space weathering features vary in returned samples from the Moon and Itokawa, and to provide a detailed analysis of the structural and chemical characteristics in those returned samples using cutting-edge TEM techniques. This research moves beyond only analyzing returned samples, and develops a new method for simulating micrometeorite impact events in the laboratory, providing insight

into the chemical and structural effects of space weathering on surface soils. The emphasis for this work was on providing data for a more comprehensive understanding of space weathering across the inner solar system.

The TEM was used for each aspect of this work. It provided the platform from which to collect structural and chemical information on space weathering features in returned samples using cutting-edge microscopy techniques. It also served as the laboratory for performing in situ experiments simulating space weathering processes and enabled the analysis of resulting features. TEM capabilities were an integral part of this work and facilitated its completion.

This dissertation is divided into six chapters. Chapter 2 provides a brief overview of the TEM and associated techniques used in this work, including: image formation, high-resolution imaging, energy-dispersive x-ray spectroscopy, and electron energy-loss spectroscopy and the quantification of these spectra. Chapter 3 provides a detailed chemical and microstructural characterization of space weathering features in soils returned from asteroid Itokawa, comparing them to lunar soils and discussing implications for the variability of space weathering processes across airless body surfaces. Chapter 4 presents an in-depth analysis of the structure, chemistry, and oxidation state of individual npFe in lunar soils of varying maturities using cutting-edge electron energy-loss spectroscopy techniques. This chapter discusses the implications for the results in the context of the development and of evolution of space weathering features in airless body samples. Chapter 5 develops and applies a new methodology for simulating micrometeorite impacts, by performing the first observed, dynamic, in situ heating experiments of lunar soils inside the TEM. This chapter provides a detailed

analysis of samples subjected to simulated weathering, comparing the structure and composition of the resulting features with natural samples, and providing insight into how and the rate at which space weathering features develop in surface soils. Chapter 6 summarizes the dissertation, discusses the broad-scale implications of the research, and outlines potential future work to be performed. Chapters 3 and 4 were published in *Earth, Planets and Space*, and *Meteoritics and Planetary Science*, respectively. Chapter 5 has been submitted to *Meteoritics and Planetary Science*.

CHAPTER 2

METHODS

2.1 Introduction

The transmission electron microscope (TEM) enables the analysis of sample crystal structure and chemistry, down to the atomic scale. These analyses are made possible by electron-specimen interactions that occur inside the TEM. Understanding electron scattering is fundamental to performing the TEM techniques employed in this work and interpreting the resultant data.

The following chapters consist of two published and one submitted paper that contain abbreviated methods sections. These chapters present data acquired through several TEM techniques, including: electron diffraction, imaging in both TEM and scanning TEM (STEM) modes, high-resolution imaging, energy-dispersive x-ray spectroscopy, electron energy-loss spectroscopy, and in situ heating. This chapter provides a description of the relevant theory and experimental procedures used for this work. A more detailed consideration of the theoretical principles and their applications to sample analyses can be found in Williams and Carter (1996), Egerton (1996), and Cowley (1995).

2.2 Sample Preparation

Adequate sample preparation for the TEM is critical for obtaining useable data. Specimens must be electron transparent in thickness, which is typically <100 nm. Two

techniques, ultramicrotomy and focused-ion beam scanning electron microscopy, were used to prepare electron-transparent sections for this work.

2.2.1 Ultramicrotomy

An ultramicrotome operates by mechanically moving a specimen past a knife blade to slice off electron-transparent sections, which are then deposited onto a TEM grid for analysis (Bradley 1988). To prepare the sample for slicing, it is first embedded in a low-viscosity epoxy and then cured for several days at $\sim 60^\circ\text{C}$. The sample could be a singular grain or specimen, or multiple grains clustered together. The specimen sits at the tip of the epoxy bullet, called the block face. The epoxy material surrounding the sample of interest is then trimmed away using a diamond trimming knife, leaving a narrow section of the block face containing the sample ready to be sliced (Fig. 2.1). This trimming makes the width of the sample to be sectioned narrower than the width of the slicing knife blade, ensuring the entire sample will be sectioned each time it passes the

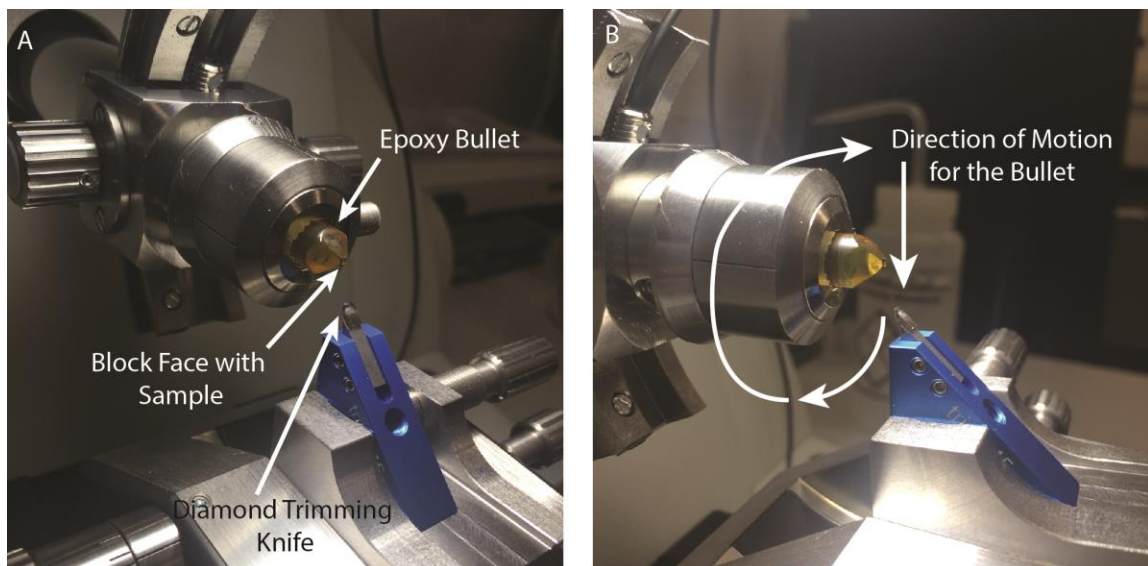


Figure 2.1: Trimming the epoxy bullet. (A) The block face of the bullet and the location of the sample and the diamond knife used for trimming. (B) The direction of motion the bullet takes to pass by the trimming knife.

cutting knife, and it will remain coherent, not fragmenting into many pieces. While trimming and cutting knives can be made of materials such as glass (common for biological sections), diamond knives were used for this work, as the blades must be composed of material harder than the samples they are slicing, i.e., the hard lunar and Itokawa soils investigated here.

After trimming, the epoxy stub is then repeatedly moved past the diamond cutting knife, which is held stationary (Fig. 2.1). This motion can be performed mechanically by the user or can be automated by the digital controls of the ultramicrotome. If automated, a slice thickness is set, e.g., 20 nm to 1 μm . This thickness dictates how far forward the block face moves towards the knife after each pass. As a result, this value determines the thickness of the sample sliced off with each pass. Typical thickness values are ~ 60 nm, but anything less than 100 nm should create electron-transparent sections (Williams and Carter 1996). However, for certain TEM techniques, e.g., electron energy-loss spectroscopy (discussed in section 2.7), samples even at 60 nm may be too thick to achieve good signal. With each motion past the knife a thin section of the epoxy containing the sample is sliced off. This motion continues and, like slicing a loaf of bread, produces serial thin sections of the sample. The desired specimen thickness value that is set in the microtome is optimal, but in practice the slices are often thicker than this value because of the heterogeneous and hard nature of samples prepared in this work.

The cutting blade is situated at the topmost edge of a vessel with a hollowed-out reservoir known as the boat (Fig. 2.2). During slicing the boat is filled with deionized water, and as the sections are sliced serially by the knife, they float off the blade into the water bath. If the sample is sliced coherently by the blade with each stroke, a long chain

of connected sections will remain intact. This chain of sections can be detached from the knife blade and extracted from the water bath using a tool called the ‘perfect loop’. This loop uses surface tension to extract a droplet of water containing the sections and to deposit the droplet onto a waiting TEM grid, typically resting on absorbent paper, e.g.,

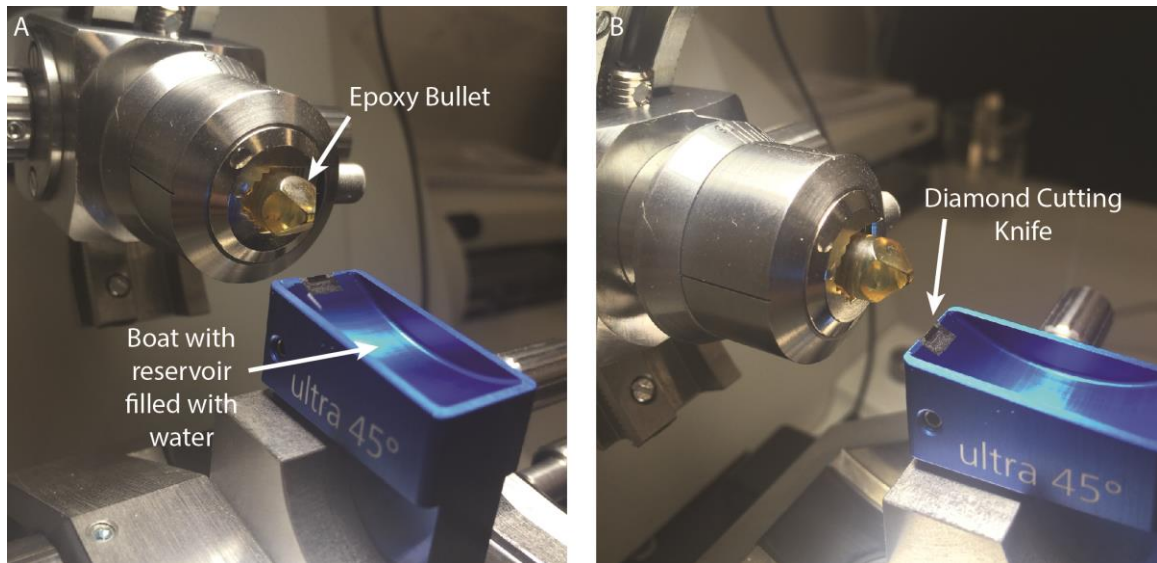


Figure 2.2: Slicing of the epoxy bullet. (A) the block face of the bullet and the boat filled with water, and (B) the diamond cutting knife.

filter paper. The water droplet soaks into the paper, depositing the sections onto the TEM grid for analysis. Several chains of sections can be placed on the same grid (Fig. 2.3).

A variety of TEM grid styles are available for use. In this work, sample grids are 3 mm in diameter (the standard width for TEM sample holders) and composed of a fine Cu or Mo mesh. The grid is coated with a thin, transparent layer of amorphous carbon, which allows for the sample sections to be suspended between the grid bars for analysis in the TEM. The grid bars themselves are too thick to be electron transparent, and so all sample analysis occurs on material that is suspended on the carbon film windows.

Ultramicrotomy is an effective sample preparation technique for grains $<50\ \mu\text{m}$ in diameter. Hard samples larger than this have a tendency to fragment after contacting the

knife as the size of the block face creates a high cutting pressure, a phenomenon known as ‘chattering’ (Zolensky et al. 2008). This can create difficulties in preserving context or the location of certain features in relation to the grain as a whole. For analyses of space-weathered samples, the characteristics of which are typically found in the outer 100 nm

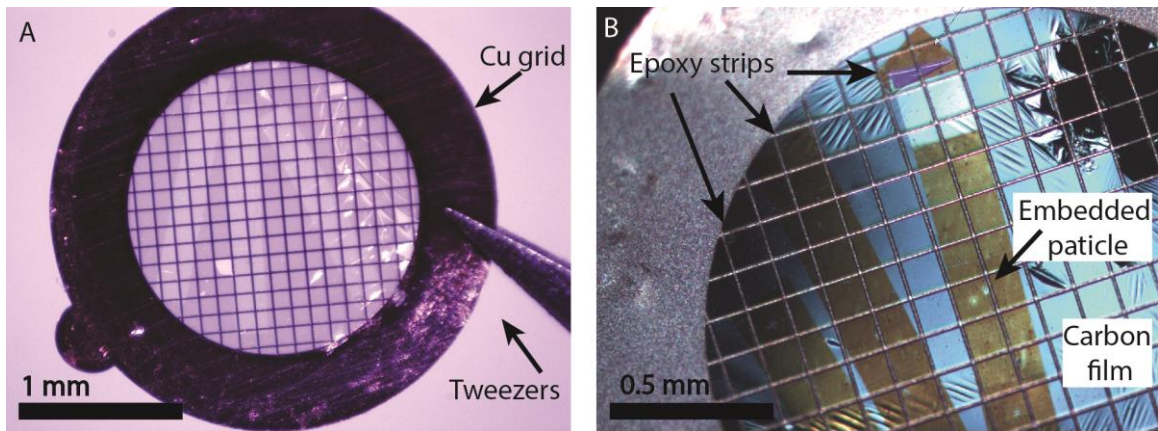


Figure 2.3: Transmitted light image of (A) a Cu TEM grid, and reflected light image of (B) Three epoxy strips with embedded particles sitting on C film of the TEM grid.

of the grain rim, context is important. Ultramicrotomy is also not site specific, and so the entire specimen/grain will be sliced, regardless of whether the user is interested in features from a localized area. A significant fraction of the samples analyzed in this work were prepared by ultramicrotomy. In Chapter 3, samples from the near-Earth asteroid Itokawa were prepared by the Hayabusa mission curation team using this method. In Chapter 4, each of the lunar soil samples was prepared using the ultramicrotome in the Environmental Health Sciences Center at the University of Arizona. Two out of three Fe standards used for the work in Chapter 4 were prepared in a similar fashion. The third standard was prepared using the focused ion beam, discussed below in section 2.2.2. In Chapter 5, samples were prepared by a different methodology, discussed in section 2.8.

2.2.2 Focused Ion Beam Scanning Electron Microscopy

The focused ion beam scanning electron microscope (FIB) enables site-specific extraction of material from a sample for thinning to electron transparency. The FIB couples the nondestructive imaging and analytical capabilities of a scanning electron microscope (SEM) with an ion beam able to sputter away material with <10 nm precision (Gianuzzi and Stevie 2005). Using this unique combination of capabilities, an electron transparent thin section can be created in three stages: coarse cutting, in situ extraction, and in situ thinning.

After the region of interest (ROI) in the sample has been selected, a protective strap, typically Pt or C in composition, several μm in thickness and ~ 10 μm in length, is deposited over the ROI to protect the underlying sample from damage, i.e., ion implantation and irradiation, during sputtering. A section, or lamella, is created by removing the material from either side of the strap with a focused beam of Ga^+ ions. A

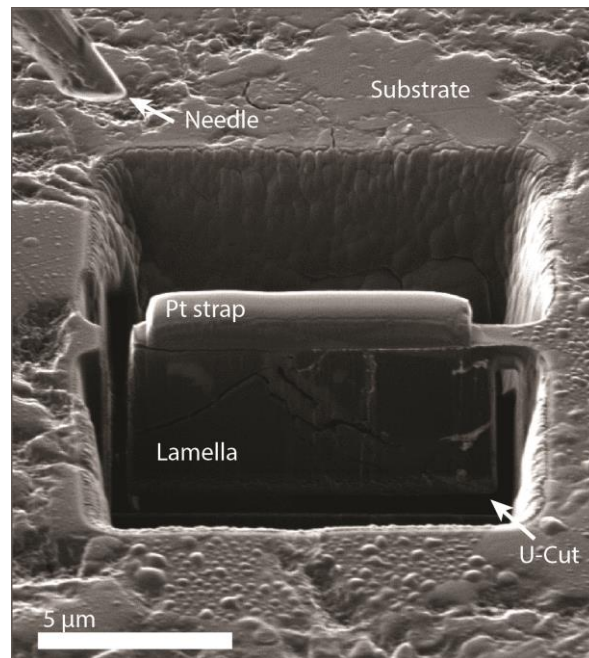


Figure 2.4: Secondary electron image of the lamella with protective strap, the milled material on either side, the U-cut to detach the lamella, and the incoming needle.

milling pattern is set, typically a stair-step or ramp shape extending several microns from the strap in either direction (Fig 2.4). Once this material has been milled, the lamella is thinned to $\sim 0.5 \mu\text{m}$ in thickness, while still attached to the surrounding material (Zega et al. 2007).

The section is then extracted from the surrounding substrate by using a ‘u-cut’. This cutting pattern mills away the connection to the substrate along one side, undercuts the base, and mills most of the material from the other side. The u-cut leaves only a small section of the lamella at the uppermost corner attached to the surrounding substrate (Fig. 2.4). A tungsten needle, affixed to a micromanipulator, is then inserted into the field of view, and moved into contact with the corner of the section. The needle is welded to the section, and the final remaining notch connecting the sample lamella to the surrounding substrate is milled away. The needle is slowly retracted, pulling the section free from the surrounding substrate. The section is then attached to the post of a TEM grid, welded in place, and the needle detached. The lamella can then be thinned to electron transparency by shaving material from either side of the section iteratively using the Ga^+ ion beam. The end result is an electron-transparent thin section of material attached to a TEM grid, free of any underlying film.

Only one sample for this work, the Fe metal standard discussed in Chapter 4, was prepared using FIB. This sample was made using the FEI Nova 200 NanoLab FIB at Arizona State University.

2.3 Image Formation

In the TEM, electrons are emitted from a source cathode and pass through the condenser lenses and aperture, which adjust the convergence angle and current of the beam. The TEM can operate with the beam parallel to the optic axis of the instrument, referred to as conventional TEM, or with the beam converged into a fine size probe which is rastered across the sample, called scanning TEM or STEM mode. In TEM mode after transmission through the sample, electrons pass through the objective lens, which focuses diffracted beams in its back focal plane, forming a diffraction pattern. Those diffracted beams are recombined to form an image in the image plane of the objective lens. The electrons are magnified by the intermediate lens and then projected onto the viewing screen by the projection lens (Fig. 3).

A diffraction pattern can originate from the illuminated area of the sample if encompassing the field of view, or from a specific region of the specimen, which can be isolated by inserting a selected-area aperture. This aperture is inserted into the image plane of the objective lens to select the localized region of the sample and form a selected-area electron-diffraction (SAED) pattern (Fig. 2.5). The process for indexing such patterns will be described in Section 2.5.

Electrons exiting the sample, when considered as waves, can have different amplitudes and phases. These wave properties determine the image contrast, creating either phase-contrast or amplitude-contrast images. Phase-contrast images, i.e., high-resolution images (HRTEM), are formed when all or nearly all of the diffracted electrons are allowed to interfere with one another and transmit to the image plane. The phase of the electron wave is determined by the atomic positions in the specimen, and so HRTEM

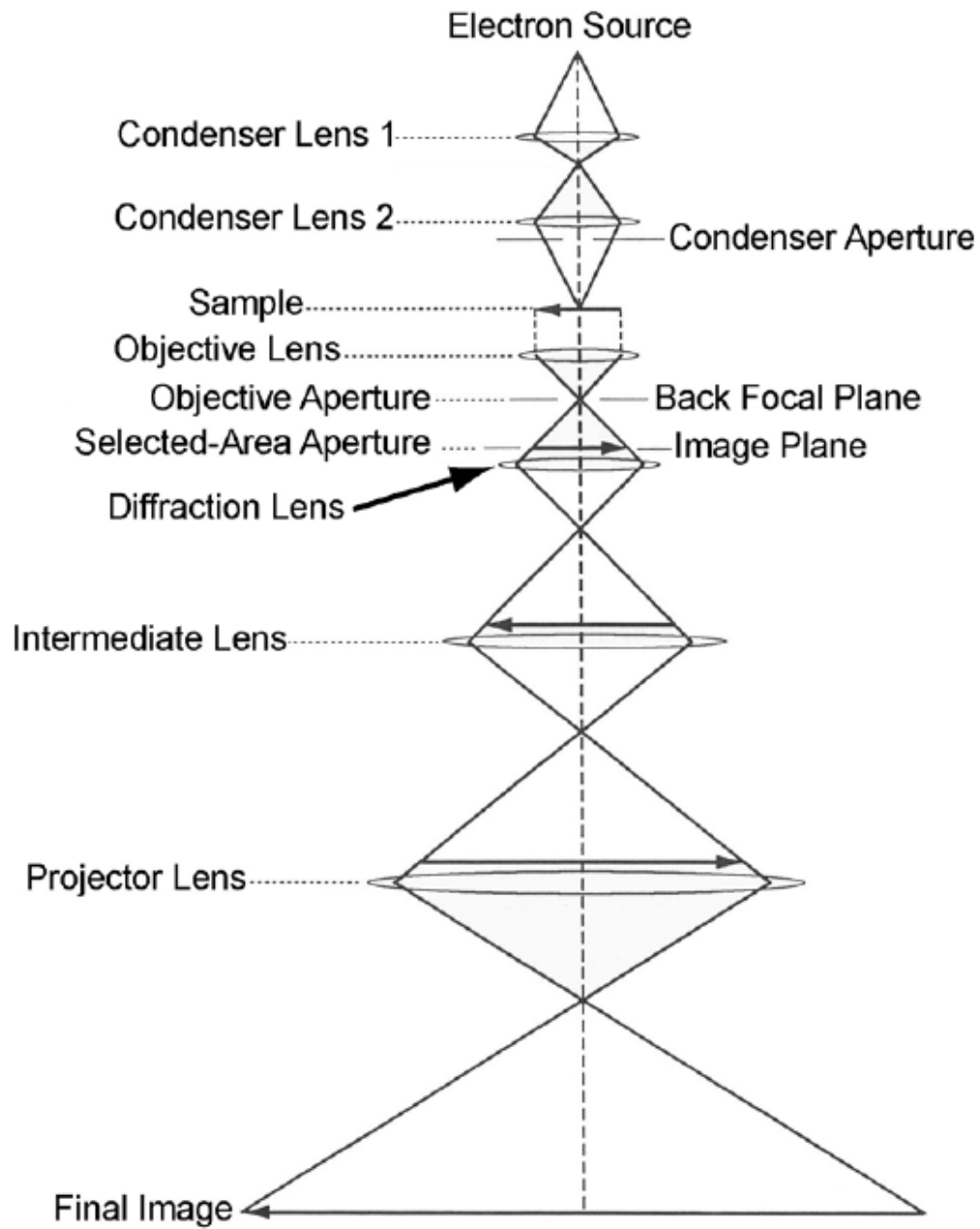


Figure 2.5: Ray diagram of a TEM showing the objective aperture in the back focal plane of the objective lens, and the selected-area aperture in the image plane of the objective lens, from Zega (2003) and after (Buseck and Allen 1992).

images provide information on the crystal structure of the specimen, revealing lattice fringes representative of the spacing of atomic planes in the material (if it is crystalline) (Williams and Carter 1996). In comparison, forming amplitude-contrast images requires the insertion of an objective aperture into the back focal plane of the objective lens. This aperture restricts diffracted waves from interfering with one another. Therefore, only amplitude information is transferred to the image, forming an amplitude-contrast image, e.g., a bright-field (BF) image (Williams and Carter 1996). Several types of images can be obtained in conventional TEM mode (Fig. 2.5). A BF image is formed when an aperture is used to select only the direct beam (not diffracted beams) for image formation. A dark-field (DF) image is formed when diffracted electrons are selected to contribute to image formation. In STEM mode, BF and DF images can also be formed, but they depend on the scattering angle of the electrons and the detector used to collect them, as discussed in section 2.4.

2.4 Electron Scattering

Electrons transmitted through the sample encounter and interact with other electrons and atomic nuclei in the specimen. If such interactions do not cause the incident electrons to lose any energy, these electrons are elastically scattered and contribute contrast to TEM images. In STEM mode, electrons that are scattered between 0 to 10 mrad, relative to the optic axis, are elastically scattered and can be detected to form a BF STEM image.

If, however, the incident electrons lose energy as a result of their interactions with the sample, they are inelastically scattered. In STEM mode, electrons that are

scattered to high angles, >50 mrad, can be detected to form high-angle annular dark-field (HAADF) images, in which brightness is proportional to atomic number, i.e., Z^2 . Inelastic scattering can also produce X-rays, used for energy-dispersive x-ray spectroscopy (EDS), and energy-loss electrons, used for electron energy-loss spectroscopy (EELS).

To understand the generation of X-rays and energy-loss electrons, we refer to the Bohr model of atomic structure in which nuclei are surrounded by orbiting electrons located in discrete shells. If an incident electron has enough energy to penetrate the outer shells of an atom in the sample, it can collide with an electron orbiting in an inner core-shell electron shell. This collision imparts some energy to the core-shell electron, which if greater than or equal to the critical ionization energy, will eject the electron from its orbit.

After the ejection of the core-shell electron, the atom from which it came is then in an unstable, ionized state. To return to its ground state, an electron from an outer shell will fill the hole left by the ejected electron. This transition is accompanied by the emission of energy in the form of an X-ray. The energy of that X-ray is specific to the energy difference between the electron shells, and as a result is characteristic of the particular atom from which it is emitted. The number of X-rays and their energies that are generated by these interactions can be measured by a detector and can provide quantitative compositional information about the sample, discussed further in section 2.6. In addition, the amount of energy that incident electrons lose as a result of inelastic scattering can also be measured. This energy-loss is also characteristic of the specific atom the electron encountered, and can provide compositional and structural information about the specimen, discussed in detail in section 2.7.

Other electrons, loosely held in the valence and conduction bands of the specimen can also be ejected from the sample. These electrons are known as secondary electrons, and can be collected by a detector and used to analyze the surface topography of the sample, known as secondary electron imaging (SE). Chapter 5 presents SE imaging of lunar soil grains.

2.5 Selected Area Electron Diffraction

Electron-diffraction patterns can provide microstructural information about the sample. When electron waves are diffracted from ordered crystal planes in a structure, they produce a pattern of spots. Measuring the distance between the resulting diffraction spots, known as reflections, provides information about the atomic-plane spacing, or d -spacing, of the specimen material. The relationship between the diffraction spots (Fig. 2.6) and the d -spacing, is given by:

$$(2.1) \quad Rd = \lambda L$$

where R is the distance measured between the reflections, in e.g., units of pixels for digital images; d is the interplanar spacing for the material (\AA); λ is the wavelength of the electrons being accelerated at the sample (\AA); and L is the camera length used to record the diffraction pattern, in e.g., cm (Williams and Carter 1996). Rather than input each variable independently, however, λL together is known as the camera constant, and can be determined for the operating voltage of a TEM at each available camera length using a set of standards with known d -spacings. For the research described herein, camera constants were determined using powdered Al standards for the JEOL 2010 TEM

microscope at ASU, where the SAED for this work was performed. The constants, measured in $\text{px} \cdot \text{\AA}$, are provided in Appendix A.

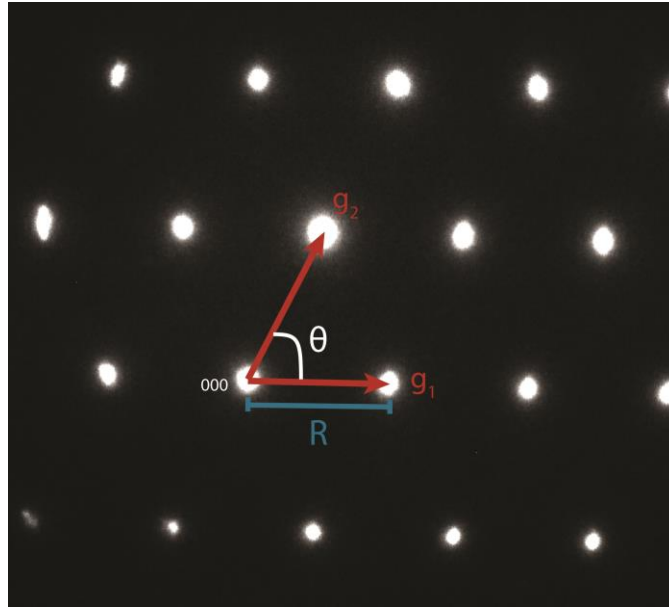


Figure 2.6: Diffraction pattern showing reflections (white spots) and the radius (R) measured between the origin and a reflection. Two vectors, g_1 and g_2 indicate candidate radii to be measured and the angle between them is indicated by theta.

Knowing the camera constant λL , and measuring spacing between spots, R , enables the calculation of the d -spacing in the unknown material. This spacing can be compared to standard values for different candidate mineral phases, which can be found in databases, e.g., the American Mineralogist Crystal Structure Database. From this, Miller indices can be identified and ascribed to a family of planes giving rise to a set of reflections.

The angle between reflections can be used in conjunction with the d -spacings to identify candidate phases for the specimen. After identifying candidate d -spacings for reflections in the pattern, the angle between those corresponding spots can be measured (Fig. 2.6). This measurement can be compared to the theoretical angle that would exist between the identified spacings, which can be calculated using the dot product. For

example, the angle between two planes with Miller indices of $(h_1k_1l_1)$ and $(h_2k_2l_2)$ would be calculated via:

$$(2.2) \quad \cos \theta = \frac{h_1h_2+k_1k_2+l_1l_2}{\sqrt{h_1^2+k_1^2+l_1^2} + \sqrt{h_2^2+k_2^2+l_2^2}}$$

If the theoretical and the measured angles match, then the indexing is a good solution for the diffraction pattern. The crystal orientation can then be calculated using from the indexed reflections via the cross product:

$$(2.3) \quad (h_1k_1l_1) \times (h_2k_2l_2) = (k_1l_2 - k_2l_1) - (h_1l_2 - h_2l_1) + (h_1k_2 - h_2k_1)$$

The cross product provides the upward foil normal vector to the crystal surface through which the electron beam propagates. Indexing and determination of orientation allows for the identification of phases through SAED patterns, as was done for part of the work on samples from near-Earth Itokawa, presented in Chapter 3.

In order to efficiently identify candidate microstructures, it is common and useful to collect chemical information from the sample as well, often done by energy dispersive x-ray spectroscopy.

2.6 Energy-Dispersive X-Ray Spectroscopy

Energy-dispersive X-ray spectroscopy (EDS) analyzes the energy of the x-rays that are produced through inelastic scattering processes described above. The spectrometer is composed of a semiconductor, commonly made of Si doped with Li, which detects X-rays. When the X-ray hits the detector, a charge pulse is generated, which is proportional to the energy of the incoming X-ray. That pulse is converted to a voltage and amplified, and stored in a channel assigned to that specific energy. These

pulses are presented on the display as a histogram of the number of pulse counts versus x-ray energy (in keV) (Williams and Carter 1996).

The X-ray spectrum consists of Gaussian-shaped peaks on a continuous background, the intensity of which decreases as energy increases, following a known and predictable trend (Fig. 2.7). The background energy, known as braking or Bremsstrahlung radiation, arises when incident electrons are slowed or stopped entirely as a result of interactions with specimen nuclei (Williams and Carter 1996). The amount of background radiation produced can be mathematically modeled by:

$$(2.4) \quad N_E = KZ \frac{(E_0 - E)}{E}$$

where N_E is the number of photons produced at energy E , Z is the average atomic number of the specimen, E_0 is the beam energy (keV) and E is the X-ray energy (keV). K is a constant that accounts for the collection and processing efficiency of the detector, and the absorption of X-rays within the specimen. This background radiation should be removed in order to quantify the EDS spectra, which can be done by modeling its intensity, as discussed in Williams and Carter (1996).

For quantification of EDS spectra, the intensity data (counts) can be used to determine the percent composition, based on the Cliff-Lorimer relationship (Cliff and Lorimer 1975). For example, in a binary system, the intensity of component 'A' relative to component 'B' can be determined by:

$$(2.5) \quad \frac{C_A}{C_B} = k_{AB} \frac{I_A}{I_B}$$

and

$$(2.6) \quad C_A + C_B = 100\%$$

where I_A and I_B are the intensities of the collected X-rays, C_A and C_B are the concentrations of the elements under investigation, and k_{AB} is a sensitivity factor which varies depending on the particular spectrometer, microscope, and analytical conditions.

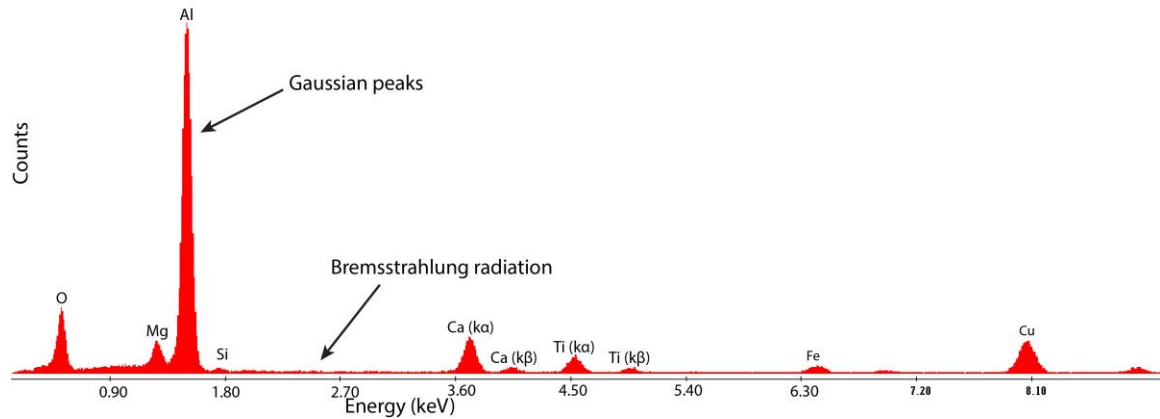


Figure 2.7: Example EDS spectrum showing the Gaussian peaks for each element present in the sample (here, hibonite $\text{CaAl}_{12}\text{O}_{19}$) and the background, Bremsstrahlung radiation.

The sensitivity factor, known as a k-factor, is determined for particular elements, usually relative to Si for geological and planetary science applications, from standards with a known composition that was determined by other methods. The k-factors for the JEOL 2500 SE microscope at Johnson Space Center, where all quantitative EDS was performed, were determined from standards by their in-house TEM manager. These sets of equations can then be solved simultaneously to determine quantitatively the composition of the sample.

EDS measurements can take the form of individual point analyses, linescans, qualitative maps, or quantitative spectral images. This work primarily relied on collection of qualitative and quantitative maps, which are presented as parts of Chapters 3 and 4.

In addition to EDS measurements, compositional information from a sample can be measured using other techniques, including electron energy-loss spectroscopy.

2.7 Electron Energy-Loss Spectroscopy

Inelastically scattered electrons can be detected and their energy-loss measured with an electron energy-loss spectrometer. The spectrometer has an entrance aperture, focusing coils, a magnetic prism, and a detector. Electrons enter the spectrometer through the entrance aperture, which can vary in size from 1 to 5 mm and is used to control the collection angle, and travel through the magnetic prism, where they are deflected depending on their velocity (lower velocity having smaller radius of curvature) (Egerton 1996). Differences in velocity are due to the variable interactions the electrons had with the specimen, and are thus characteristic of composition of the material. The spectrometer focuses the electrons onto the detector, ordered by their radius of curvature, to produce a spectrum of counts versus energy loss (eV) (Fig. 2.8). This energy loss spectrum has several components: 1) Zero-loss peak (ZLP), 2) Low-loss region, and 3) High-loss region (Fig. 2.9).

The ZLP is produced by electrons that have lost little to none of their incident energy as they transmit through the specimen. The low-loss region (<50 eV) is produced primarily by electrons that have interacted with conduction and/or valence band electrons in the specimen, known as plasmons. The high-loss region (>50 eV) is produced from inelastic scattering of electrons when they encounter the inner or core-shell electrons of the specimen. This high-loss region contains core-loss edges, described below, that sit atop a background signal. The background is produced by electrons that experience plural (>1) and multiple (>20) scattering events, the frequency of which depend on the sample thickness (Williams and Carter 1996).

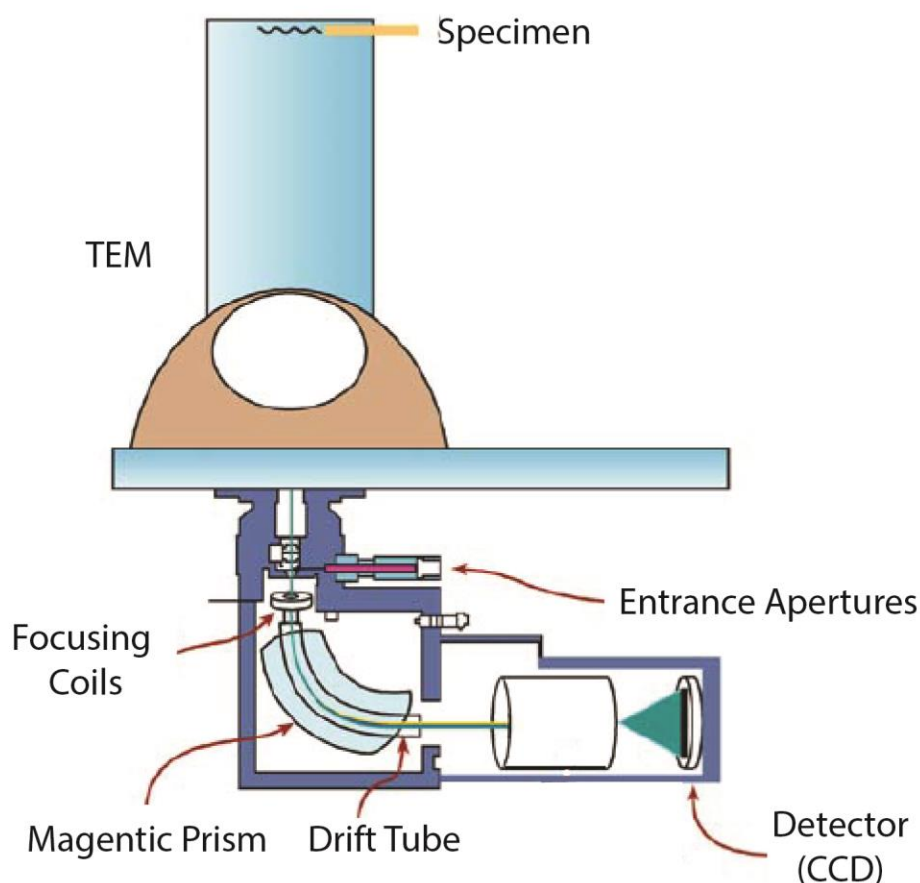


Figure 2.8: Schematic of a TEM with attached EELS spectrometer. The focusing coils are used to align and focus the ZLP. The magnetic prism and lenses focus the beam. The electrons are detected by the CCD. Adapted from Williams and Carter (1996).

The energy profile of a core-loss edge is characterized by the edge onset (critical ionization energy), a sharp rise to maximum and a more gradual decrease to the background level, giving the overall edge a roughly triangular shape (Fig. 2.10). The core-loss edge can contain fine-scale structure near the edge-onset, called energy-loss near-edge structure (ELNES), which provides information on oxidation state and bonding environments. The edge can also contain small intensity oscillations ≈ 50 eV away from the edge, called extended energy-loss fine structure (EXELFS), which provides information on nearest neighbors (Alamgir et al. 2003).

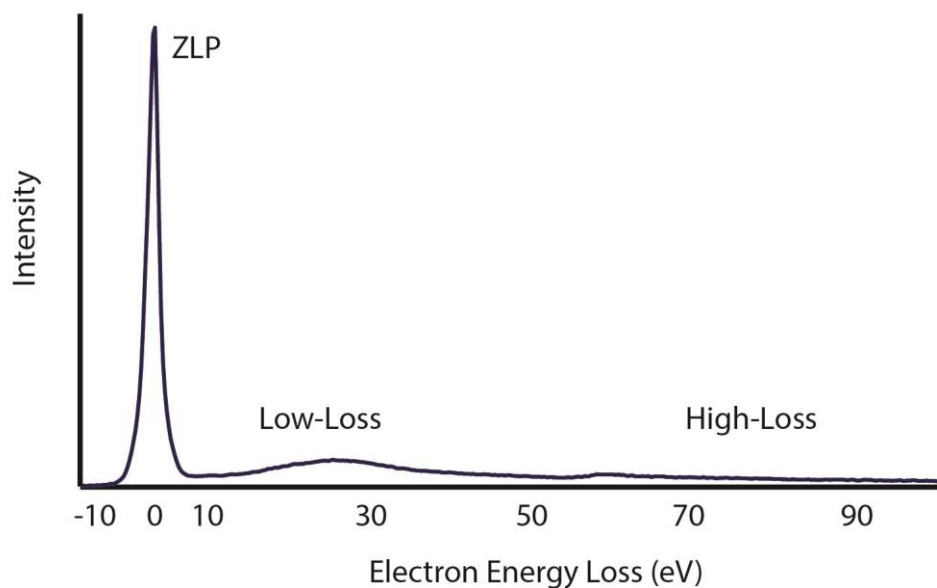


Figure 2.9: Example EELS spectrum showing the ZLP, the low-loss region (<50 eV) and the high-loss region (>50 eV).

The background signal must be removed from the spectrum to obtain quantitative information from the core-loss edge. The background signal has an energy-dependence following a power-law function in the form of AE^{-r} . The background can be removed by defining an energy window prior to the edge onset to fit this function, and then subtracting it from the spectrum (Egerton 1996).

EELS measurements can be collected from individual spots, linescans, or spectral images. This work collected EELS linescans of npFe particles in Chapters 4 and 5. After the collection of an EELS spectrum from the unknown sample, the edge-onset position and shape and fine structure of the edge can be compared to measured standards to identify, e.g., the oxidation state of the material in the sample. In this work, we compared the nanoparticle spectra to those collected from standards for Fe^0 , Fe^{2+} , and Fe^{3+} . A linear, least-squares fitting routine was developed to compare the unknown spectrum to

the measured standards and determine the quantitative contributions from each oxidation state. The MATLAB code used for spectral quantification is shown in Appendix B.

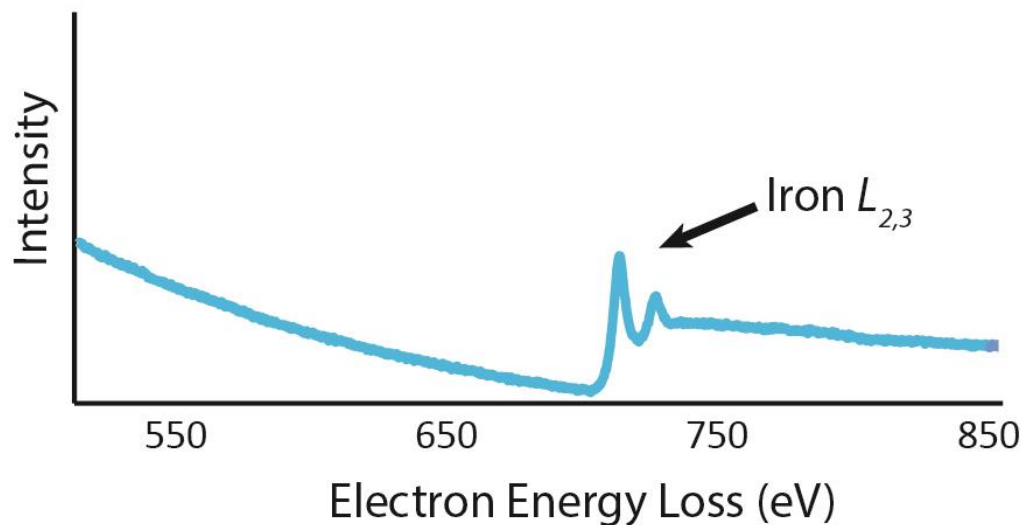


Figure 2.10: Example EELS core-loss edge for the Fe $L_{2,3}$ edge, showing a roughly triangular shape.

The EELS measurements in this work were performed on two types of samples:

- 1) Fe nanoparticles produced by natural space weathering processes in lunar soils, and 2)
- Fe nanoparticles produced experimentally via in situ rapid-heating of lunar soil grains to mimic micrometeorite impacts.

2.8 In Situ Heating

The capabilities for performing in situ experiments inside the TEM have improved dramatically in recent years. Experiments can include electrochemical reactions, gas-mixing reactions, and slow- and fast-heating. Several companies have developed specialized sample rods and chips to perform these experiments. Hitachi has developed one such holder that is designed to expose samples to temperature changes

inside the TEM while enabling the observation of changes in chemistry and microstructure (Fig. 2.11).

A sample is deposited onto a reusable heating chip composed of silicon nitride (SiN) which can be loaded into the heating holder. These chips are capable of both extremely rapid thermal shocks, e.g., up to 1200 °C in $\ll 1$ second, and slow temperature ramps/cycles. The heating chip is designed and micro-fabricated on a microelectrochemical system (MEMS) platform with multiple ultrathin (30nm) SiN membrane windows for sample viewing in TEM. The ultrathin SiN windows provide high-electron-transmission rate through the sample, ensure temperature uniformity, and serve as the sample support platform during the heating experiment.

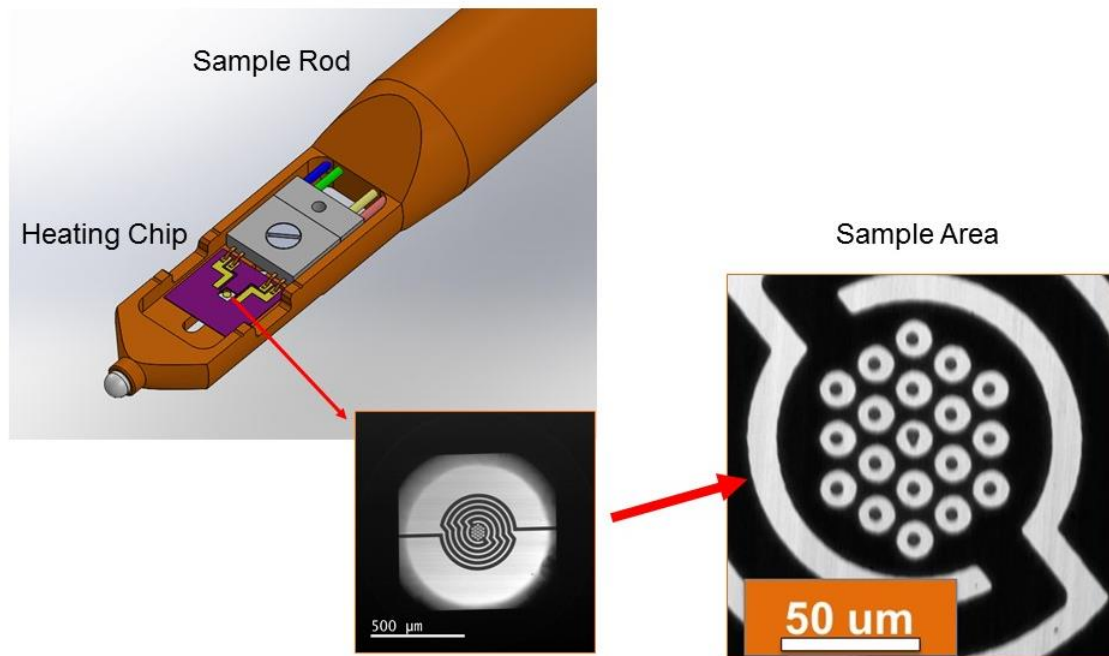


Figure 2.11: Schematic of the Hitachi sample rod and heating chip. The sample area is composed of SiN.

The actual temperature change is achieved by running a current through a wire built into the heating chip, which corresponds to a near instantaneous change in temperature. The resistance across the chip is measured during the experiment and can also be related to temperature, to provide an independent measurement of the actual temperature reached by the chip. For rapid thermal shocks, as are described for the work in Chapter 6, the temperature reached by the chip is within ~ 20 °C of the programmed level.

A slow-heating stage was also used in the work presented in Chapter 6. This stage is capable of increasing the temperature of a standard TEM grid (composed of Cu or Mo, as was used in these experiments) over a longer period of time. The temperature change is achieved by similar method described above.

CHAPTER 3
MICROCHEMICAL AND STRUCTURAL EVIDENCE FOR SPACE
WEATHERING IN SOILS FROM ASTEROID ITOKAWA

Abstract

Here we report microchemical and microstructural features indicative of space weathering in a particle returned from the surface of asteroid Itokawa by the Hayabusa mission. Space weathering features include: partially and completely amorphous rims, chemically and structurally heterogeneous multilayer rims, amorphous surface islands, vesiculated rim textures, and nanophase iron particles. Solar wind irradiation is likely responsible for the amorphization as well as the associated vesiculation of grain rims. The multilayer rims contain a nanocrystalline outer layer that is underlain by an amorphous inner layer, and both have compositions that are distinct from the underlying, crystalline orthopyroxene grain. The multilayer rim features could be derived from either radiation-induced sputter deposition or vapor deposition from micrometeorite-impact events. The amorphous islands on grain surfaces have a distinctive morphology and composition suggesting they represent surface deposits of melt derived from micrometeorite impact events. These observations indicate that both irradiation damage and micrometeorite impacts play a role in surface modification and space-weathering on asteroid Itokawa.

3.1 Introduction

Due to their exposure to interplanetary space, the surfaces of airless bodies are continually being modified by solar ions, predominantly from the solar wind, and through

micrometeorite impacts. These modifications are collectively known as space weathering and they cause changes in the chemistry, mineralogy, microstructure, and morphology of soils exposed on airless body surfaces. The culmination of these processes alters the optical properties of surface materials by reddening and darkening soil reflectance spectra and attenuating characteristic absorption bands (Chapman 2004; Clark et al. 2002; Hapke 2001). Understanding these spectral changes is important as they are theorized to contribute to the discrepancies between reflectance spectra acquired from meteorites and asteroids that prevent us from matching meteorite samples to their parent-body sources, e.g., ordinary chondrites and S-type asteroids (Binzel et al. 1996). Investigation of the nature of the space weathering process and quantification of its effects can provide information fundamental to understanding the evolution of airless body surfaces from remote sensing data.

Space weathering processes are occurring on the surfaces of airless bodies across the solar system, including the Moon and both near-Earth and main-belt asteroids. Until the recent return of the Hayabusa mission from S-type asteroid Itokawa (Nakamura et al. 2011), sample-based studies of space weathering focused exclusively on lunar soils returned from the Apollo missions and select asteroidal and lunar regolith breccia meteorites (Bernatowicz et al. 1994; Bibring et al. 1972; Hapke et al. 1975; Keller and McKay 1993, 1997; Noble et al. 2005; Noble et al. 2011; Pieters et al. 2000; Taylor et al. 2001). These investigations indicated that space-weathering features form as a product of two primary processes: (i) solar wind ion irradiation, which can cause partial or complete amorphization of material and possible chemical changes in grain rims, as well as erosion, transport and re-deposition of material on grain surfaces induced by ion-sputtering, and (ii)

micrometeorite impact events which promote melting, vaporization, and the recondensation of the target and impactor material. Each of these processes has the potential to produce reduced iron nanoparticles (npFe^0), which can be formed through vapor or sputter deposition onto the rims of surface grains and also as interior particles in lunar agglutinate glass grains. This npFe^0 contributes to the changes in optical properties we see in space-weathered materials (Noble et al. 2007).

The Hayabusa mission successfully returned thousands of dust particles from the surface of S-type asteroid Itokawa (Nakamura et al. 2011). Mineralogical analysis of several particles revealed compositions consistent with LL5-6 chondrites (Nakamura et al. 2011). The link between these particles and LL chondrites was further confirmed by oxygen isotope analyses (Nakashima et al. 2013; Yurimoto et al. 2011). The return of these samples has provided the strongest evidence yet for the long-held idea that the ordinary chondrites, the most common meteorites in our collections, are sourced from the populous S-type asteroids. The dissimilarity, however, between the reflectance spectra of Itokawa's surface and LL-type chondrites (mainly reddening in the asteroid spectrum) suggests that space weathering processes have occurred on the surface of Itokawa (Hiroi et al. 2006).

Previous investigations of Hayabusa particles for detection of space weathering features were initially completed on ten particles, five of which exhibited characteristics consistent with space weathering processes (Noguchi et al. 2011). A further detailed analysis of 12 particles was performed and these results have shown that several grains exhibit space weathering features including: radiation-damaged rims (partially and completely amorphous), Fe nanoparticles, vesiculated textures, and chemically distinct, surface-deposited rims (Noguchi et al. 2014). Thus far, Noguchi et al. (2014) suggest that

the primary mechanism for surface alteration on asteroid Itokawa is solar wind irradiation including sputtering and ion implantation. However, given the small number of particles examined, further detailed investigation is required for a comprehensive understanding of space weathering processes on Itokawa as well as other airless bodies. Here we report on previously unrecognized space weathering characteristics in a particle returned from the surface of Itokawa.

3.2 Methods

We investigated three samples (RA-QD02-0042-01, -02, and -03) of one particle, which was collected from Room A of the sample catcher on the Hayabusa spacecraft. These samples were prepared for analysis using ultramicrotomy by the Hayabusa mission curation team. The grain, originally measuring 96 μm in diameter, was sliced into many ultrathin (<100 nm) sections. Each sample contains multiple slices that were placed on C-coated Cu-support grids for analysis using transmission electron microscopy (TEM). The original particle was exposed to the atmosphere during its preparation for analysis in the TEM, but its total exposure time was less than six hours (Noguchi et al. 2014). These samples, and a subset of the space-weathering features they exhibited, were described in previous investigations (Noguchi et al. 2014; Noguchi et al. 2011).

We investigated the samples using several analytical scanning transmission electron microscopes (STEM instruments) including: 1) a 200 keV FEI Osiris ChemiSTEM equipped with a high brightness field-emission gun (X-FEG), quad-annular silicon drift detector (SDD) for energy-dispersive X-ray spectroscopy (EDS), and both dark-field (DF) and bright-field (BF) STEM detectors previously located at FEI

Headquarters (Portland, OR); 2) a 200 keV JEOL 2500SE analytical STEM at NASA Johnson Space Center equipped with a Thermo thin window Li-drifted Si [Si(Li)] EDS detector and BF and DF STEM detectors, and 3) a 200 keV JEOL 2010F STEM at Arizona State University equipped with a DF STEM detector and EDAX thin-window Si(Li) EDS system. Analysis of the assemblages within the slices included imaging via conventional TEM techniques, STEM BF and DF and high-angle annular-dark-field (HAADF). Phase identification was determined using selected-area electron-diffraction (SAED) patterns and high-resolution TEM (HRTEM) imaging. All SAED patterns were measured both manually with Adobe Photoshop and with the Crystallographic Processing Software Package (CRISP) based on calibrated camera constants. Indexing of SAED patterns was based on appropriate lattice constants and verified through simulated patterns calculated with the CrystalMaker software package. Grain compositions were measured with EDS on the JEOL 2500SE and the JEOL 2010F using spectral imaging with scanned probe sizes between 1 to 3 nm, count rates varying between 5200 – 20 000 cps, and a dwell time of 50 μ s for both instruments. EDS spectra were quantified using the Cliff-Lorimer method, with K-factors determined from in-house standards.

3.3 Results

3.3.1 General Petrography

The particle studied here is primarily composed of an orthopyroxene grain that exhibits high strain contrast with smaller, subsidiary grains of olivine (<5 μ m) and plagioclase (<15 μ m) attached to the orthopyroxene. These minerals are traceable through adjacent slices in the microtome sections. There are also Fe- and Fe-Ni sulfide minerals

(<1 μm in size) both embedded within the pyroxene grain and located on its periphery, in multiple adjacent slices on the grid. Individual grains of Fe-Ni metal, identified as kamacite, were also found on the exterior rim of this assemblage. The presence of each phase was confirmed with EDS spectral imaging and SAED (Fig. 3.1). The lath-like nature of this assemblage (shards separated by void space) is characteristic of chattering, an artifact produced during microtome sample preparation and, in this respect, is similar to samples observed from the STARDUST mission (Zolensky et al. 2006).

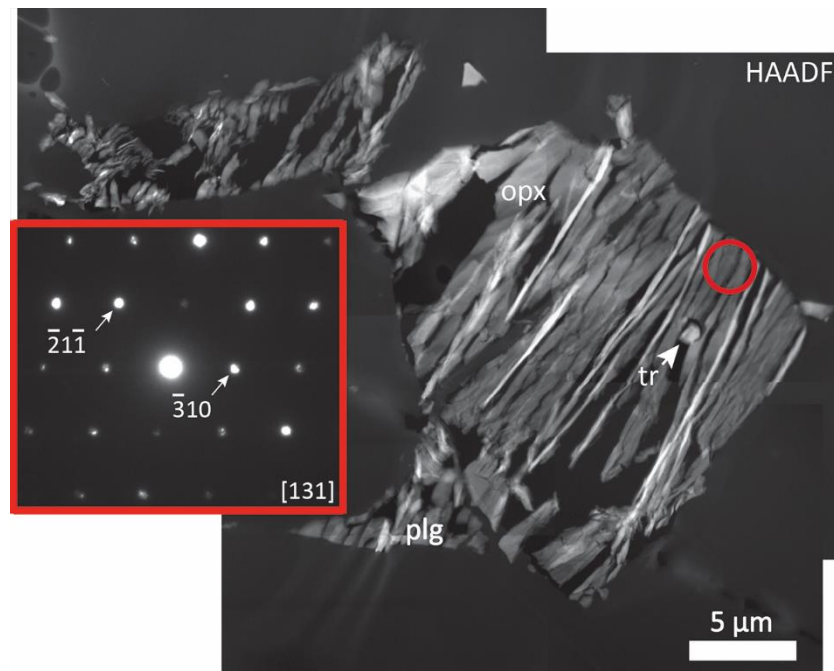


Figure 3.1: TEM data and EDS maps of particle RA-QD02-0042-02. HAADF image of one slice of the assemblage. The particle is primarily composed of orthopyroxene (opx) with minor plagioclase (plg), and troilite (tr). The lathic morphology is a result of chattering, a common texture observed in ultramicrotomed samples of small particles. The SAED pattern (inset) was collected from the region outlined by the red circle on the HAADF image, and is indexed to orthopyroxene.

3.3.2 Space Weathering Features

We analyzed over 30 individual slices for microchemical and microstructural evidence of space weathering. We observed several features indicative of space weathering

that occur in very close spatial proximity to one another along the outer rims of the grains that collectively comprise the particle within these slices. Nearly all the individual slices that we examined exhibit some degree of space weathering. While space weathering features occur in several different mineral types, the extent and degree of their manifestation differs significantly. We discuss the space weathering features in detail below.

3.3.3 Partial Amorphization

There are zones in the particle rim that have characteristics consistent with partial-to-complete solid-state amorphization of the underlying crystalline grains. The width and nature of these zones varies significantly depending on the mineralogy of the underlying grain. The partially amorphous regions are not continuous over the entire rim of the particle but instead occur in localized regions that extend laterally along the rims of individual grains in this assemblage for hundreds of nanometers (Fig. 3.2). In the low-Ca orthopyroxene grain, there is a partially amorphous zone that forms an irregular boundary with the underlying crystalline grain and extends between 10 to 60 nm into the interior (Fig. 3.2b). Within these zones there are localized nanocrystalline regions which range from 5-15 nm size. Amorphous material locally surrounds and intermixes with the crystalline domains. EDS mapping shows that the partially amorphous rims on the orthopyroxene have compositions identical to the underlying crystalline material, indicating that their only difference from the underlying material is their lack of long-range structural order. In addition, these zones of partial amorphization contain isolated Fe nanoparticles, the details of which we describe below.

3.3.4 Complete Amorphization

An outer rim of complete amorphization occurs on the plagioclase grain which contrasts to the zones of partial amorphization found on the orthopyroxene. This rim is also thinner than that on the orthopyroxene, extending only ~20 nm from the outer edge into the crystalline material, and is of more uniform thickness (Fig. 2c,d). The composition of the plagioclase rim is identical to the underlying crystal.

We note that we looked for solar flare tracks in both the orthopyroxene and plagioclase grains, but none were observed.

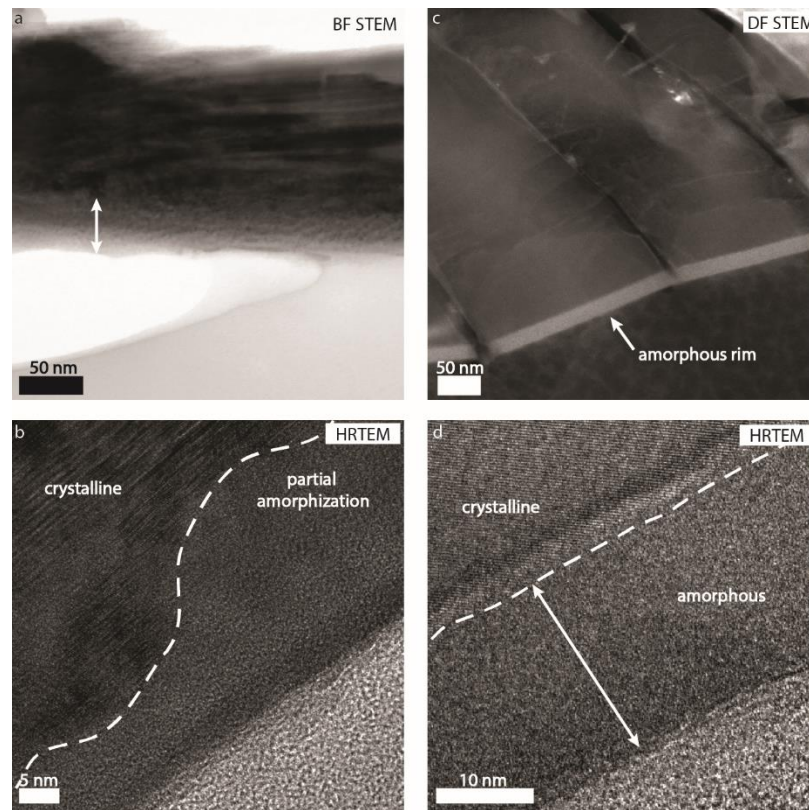


Figure 3.2: TEM data on the orthopyroxene and plagioclase grains, (A) BF STEM image of a region of the rim of orthopyroxene with arrow indicating the zone of partial amorphization, (B) HRTEM image of the highly variable depth and degree of amorphization within the orthopyroxene, (C) DF STEM image of the amorphous rim on the plagioclase grain, indicated by the arrow, and (D) HRTEM image of the rim of complete amorphization showing the uniform thickness.

3.3.5 Multilayer Rims

Local regions along the outer margin of the orthopyroxene grain are comprised of altered rim material with both underlying and overlying layers, each 2 to 5 nm thick (Fig. 3.3a,b). Laterally, the layers extend over tens to hundreds of nm of the grain rim. The multilayer feature is traceable through multiple adjacent slices and occurs in the same region of the grain rim in each slice. EDS spectral imaging shows that the outer and inner layers have compositions that differ from one another and from the underlying grain

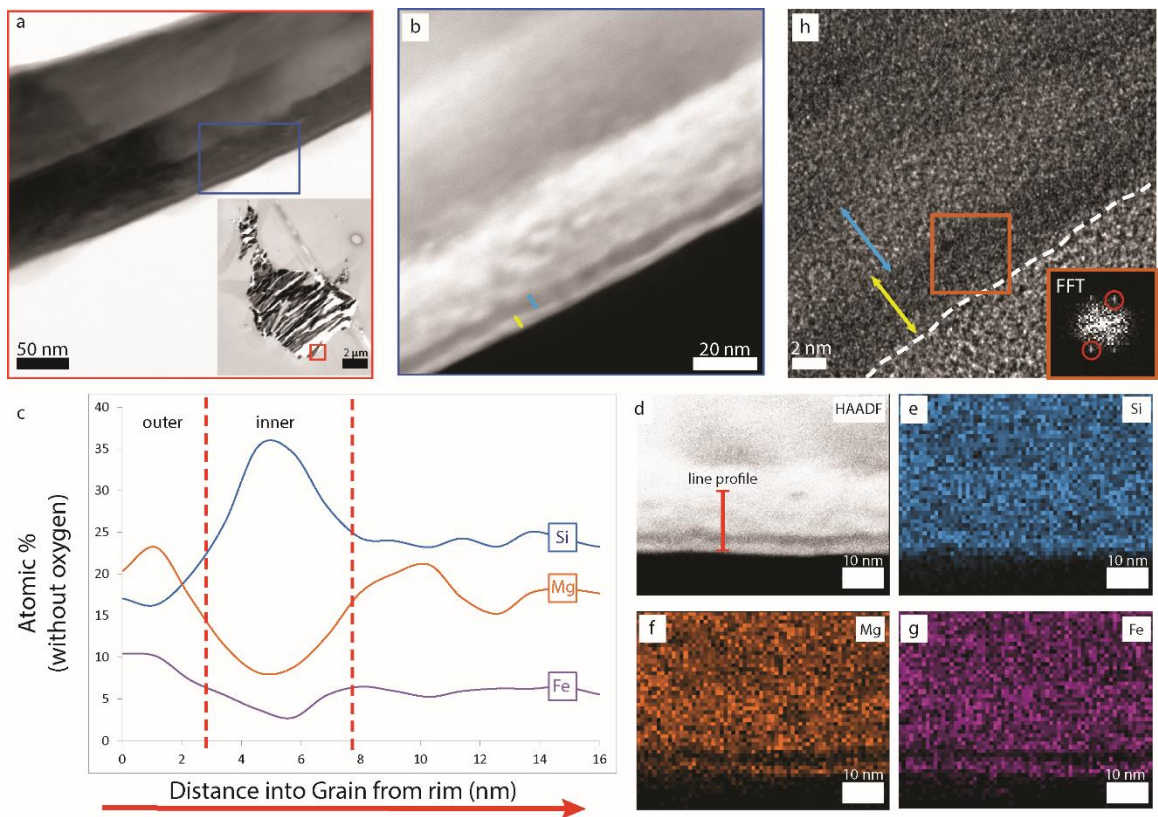


Figure 3.3: TEM and EDS data of the multilayer rims on orthopyroxene. (A) BF image of the multilayer rim on the edge of the pyroxene grain, (B) HAADF image of the rim with outer and inner layers indicated by arrows, (C) Line profile acquired from the edge of the grain, through the multilayer rim to the interior. Red dashed lines indicate boundaries between layers on the grain exterior and the underlying grain interior, (D) HAADF image of the multilayer rim and location of the line profile, (E-G) EDS spectral images of the multilayer rim, (H) HRTEM image of the multilayer rim with yellow arrows indicating the zone of nanocrystallinity and blue arrows indicating amorphous region. White dashed line indicates the edge of the grain and the inset FFT shows discrete reflections measuring 0.223 nm, indicating nanocrystalline nature of the outermost layer.

interior (Fig. 3.3). Quantified compositional profiles were extracted from EDS spectral images along a line through the rims and into the grain interior (cf., Fig. 3.3c, d-g). The outermost layer in the multilayer rim displays a ~ 7 at% depletion in Si relative to the bulk crystal interior and ~ 4 at% enrichments in both Fe and Mg. In contrast, the inner layer has a ~ 10 at% enrichment in Si, a ~ 3 at% depletion in Fe, and a ~ 10 at% depletion in Mg relative to the grain interior. The estimated errors are <1.7 at% (1σ) without an absorption correction.

The multilayer rim exhibits microstructural heterogeneity that correlates with the chemical differences. The outer, Si depleted, Fe, Mg-enriched layer is composed of nanocrystalline domains, as shown in the HRTEM image in Fig. 3.3h. Fourier transform diffractograms of several HRTEM images of this nanocrystalline region give reflections with d -spacings of 0.223 nm, which is close (within error) to several orthopyroxene spacings, e.g., (122), olivine spacings, e.g., (140) or (122), Fe metal spacings, e.g., (101), or MgO spacings, e.g., (111) or (200). HRTEM images show that the underlying Si-enriched layer is completely amorphous and abruptly transitions into the crystalline grain interior.

3.3.6 Amorphous Islands

In localized areas of the grain rim, there are isolated regions of material that protrude tens of nanometers from the grain surface. These island-like regions are superimposed on top of the Si-enriched layer of the multilayer rims, suggesting that they were deposited on top of the grain edge. The chemical composition of these islands is different from the underlying bulk crystal (Fig. 3.4 b-e). The islands contain significant S

(~4 at%) that is not present in the grain interior. In addition, EDS spectral imaging reveals that the islands are enriched in Fe and Mg and depleted in Si relative to the underlying bulk crystal (Fig. 3.4 b-e). HRTEM images of these islands show that they are completely amorphous.

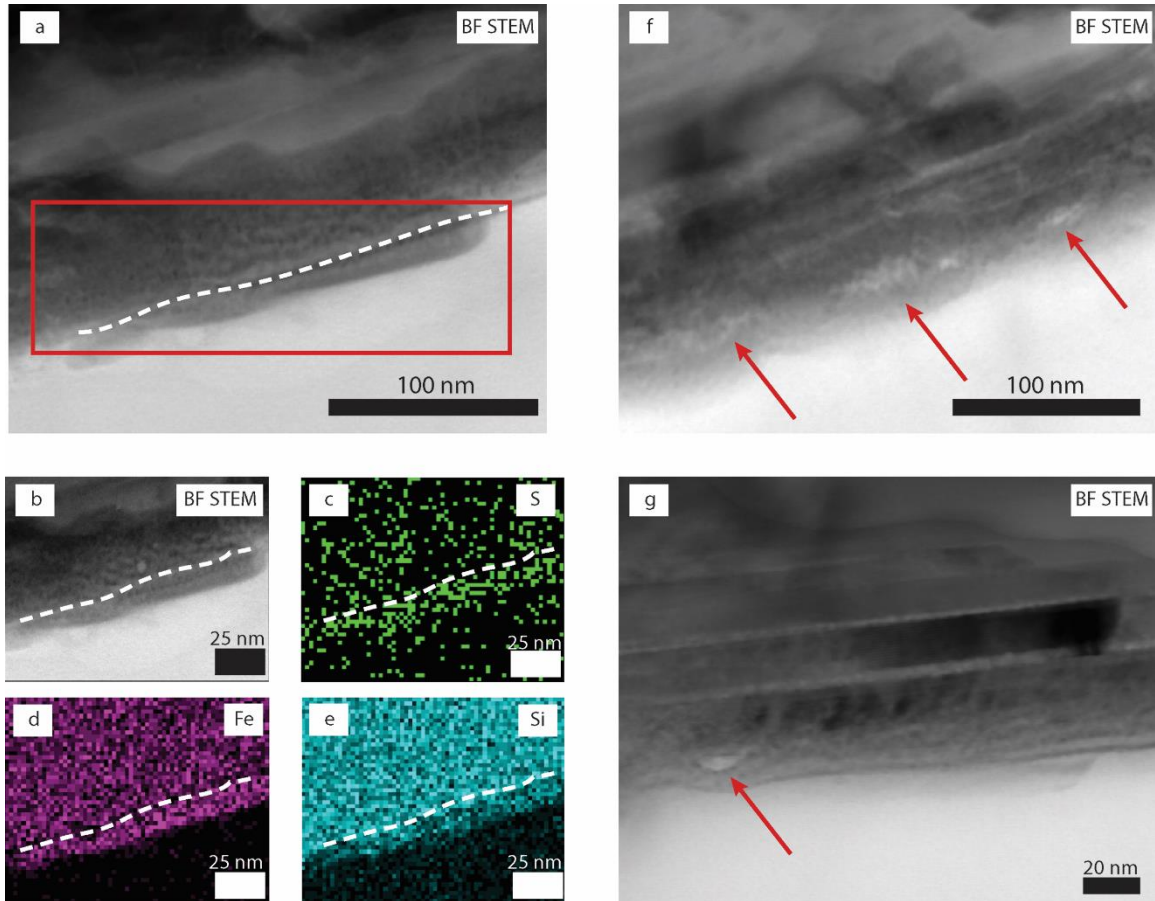


Figure 3.4: TEM and EDS data of other space weathering features in these grains. (A) BF STEM image of the amorphous island deposited on the grain rim. White dashed line indicates the original grain surface, (B-E) BF STEM and EDS spectral images of the island feature showing enrichments in Fe and S relative to the underlying grain, as located by the red box in panel (A), (F) BF STEM image of poorly developed vesicles, as indicated by arrows in the partially amorphous matrix of the orthopyroxene rim, (G) BF STEM image of a well-developed vesicle, indicated by red arrow in the partially amorphous orthopyroxene rim.

3.3.7 Vesiculated Textures

There are both well and poorly developed vesicles in the partially amorphous rim

of the orthopyroxene grain (Fig. 3.4f,g). These vesicles occur 10 to 30 nm below the grain rim surface and vary in size between 5 to 20 nm. The well-developed vesicles are emplaced in a partially amorphous matrix and cause bulging of the grain rim around them. These features are not the product of sample preparation or beam damage, having been identified in pyroxene, a relatively beam stable mineral in the TEM, in both ultramicrotomed and focused-ion beam sections. These vesicles are present in very low concentrations, occurring in localized regions of only a few slices.

3.3.8 Nanophase Iron Particles

In three of the individual slices analyzed, Fe nanoparticles were identified in high resolution EDS spectral mapping in regions of the orthopyroxene rim, but were not identified in any other mineral type sections. These findings indicate the overall abundance of Fe nanoparticles in the analyzed sample as a whole is low (e.g. Fig. 3.5). Where they

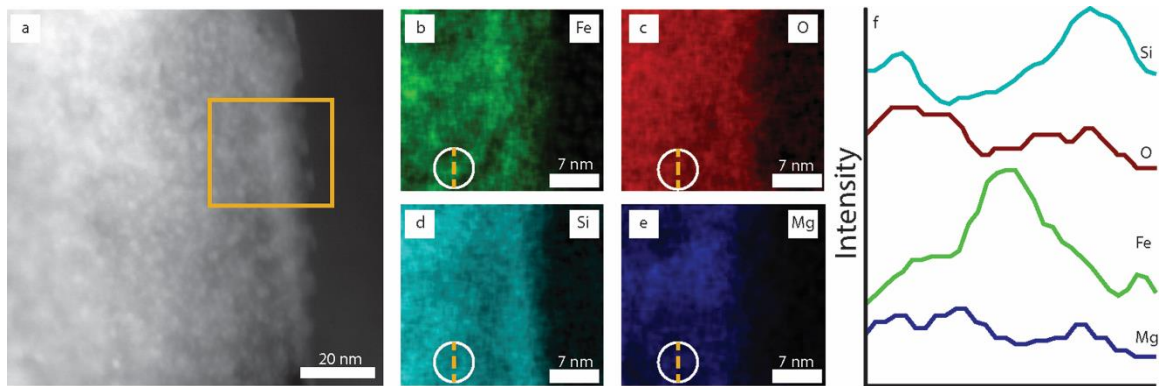


Figure 3.5: TEM and EDS data of nanophase Fe in the rim of orthopyroxene. (A) HAADF image of the orthopyroxene grain rim showing a high concentration of Fe nanoparticles, (B-E) EDS maps of the region indicated by the yellow box in panel (A). An individual particle is indicated by a white circle in panels (B-E), (F) Intensity profiles for Si, O, Fe and Mg taken across the identified particle, indicated by a dashed yellow line. Note the obvious Fe peak, the relatively consistent Mg and O concentrations, and the Si enrichment bordering the particle

occur, the nanophase Fe grains are uniformly distributed in their confined regions, occurring up to 60 nm from the exterior grain rim and are emplaced in a partially

amorphous matrix. The individual particles are uniform in size, each measuring between 2 to 3 nm. EDS mapping on an area containing a particularly high concentration of nanophase Fe particles indicates that the grains are composed primarily of Fe, with no associated Mg or S signatures (Fig. 3.5b-f). These nanoparticles may be Fe oxide or metallic Fe, though the relative depletion in O (Fig. 3.5f) in the profile of the grain may suggest metallic Fe.

3.4 Discussion

The variety of individual space weathering features we observed in these samples indicates that these grains have experienced a complex processing history on the surface of Itokawa. The nature of the observed features suggests that they developed with contributions from both ion radiation processing, almost certainly associated with solar-wind ions, and micrometeorite-impact events. Below we discuss the specific implications of each of the observed features for surface processing on Itokawa.

3.4.1 Amorphization Features

The amorphous zones (both partial and complete, which have identical compositions to the underlying grain) are attributed to solar wind ion irradiation effects. Solar ions, mostly 1 to 4 keV H^+ and He^+ have been estimated by Noguchi (2014) using the Stopping and Range of Ions in Matter (SRIM) Monte-Carlo atomic collisions code (Ziegler et al. 2008) to penetrate between 27 nm to 51 nm (H and He, respectively) into the grain interior from the rim. These simulations were performed for forsteritic ($Fe_{0.70}$) olivine (Noguchi 2014). The simulations, and the observed thickness of the orthopyroxene rims on our samples (thickness <60 nm) are also consistent with the width of ion-amorphized layers

in experimental samples, the width of rims on lunar regolith grains, and previously described Itokawa samples (Carrez et al. 2002; Keller and McKay 1997; Loeffler et al. 2009; Noguchi et al. 2014; Noguchi et al. 2011). In comparison, the plagioclase grain rim exhibits a more consistent degree of damage (i.e, complete amorphization) and is uniformly more narrow (<25 nm) than the average width of the orthopyroxene rim.

Plagioclase is, however, more susceptible to electron beam damage that may have artificially widened the rim, or altered its chemistry and microstructure. In order to account for this sensitivity, we imaged the rim for structure before completing any prolonged analytical work that would have otherwise damaged the sample before we had a chance to assess long-range order. This experimental approach ensured that the thickness and amorphous nature of the grain rim was indigenous to the samples and not an artifact of TEM analysis. After completing spectral imaging, we did observe the effects of beam damage on the plagioclase as the interface between the rim and underlying crystalline material retreated further into the grain interior, revealing that the amorphous layer had increased in thickness.

The discrepancy between the nature and thickness of the orthopyroxene and plagioclase rims suggests three possibilities: 1) the grains had relatively similar solar wind exposure times, and the different characteristics of the rims primarily reflect variations in the solid-state response of the two phases to solar wind ion irradiation. Most notably this could include differences in the critical ion fluence needed to amorphize the two phases; 2) the solid-state response of both phases to irradiation is relatively similar, and the grains were simply exposed directly to solar wind ions for different lengths of time, and finally; 3) both factors contributed to the development of these features.

We are currently not aware of any direct, quantitative experimental comparison of the ion processing behavior or relative amorphization fluences of orthopyroxene compared to plagioclase under conditions applicable to the solar wind. The ion processing behavior of pyroxene relative to a wide range of other silicates has, however, been investigated under irradiation similar to the regime expected for the solar wind (Christoffersen and Keller 2011; Wang and Ewing 1992; Wang et al. 1998a, b). These studies suggest that structures in which the Si-O tetrahedral sites are more polymerized, as in plagioclase, with a greater variety of interstitial sites, are generally much more susceptible to radiation-induced amorphization (Wang and Ewing 1992). This prediction is consistent with the well-known greater susceptibility of feldspars to electron-beam damage relative to pyroxene. As such, the differences in the degree of partial or complete amorphization between the plagioclase and orthopyroxene may reflect this difference.

With regard to the differences in width between the feldspar and pyroxene grain rims, irrespective of their degree of structural amorphization, several factors may play a role. The intrinsic penetration range of ions into the two minerals are determined by differences in the nuclear-elastic, and electronic, stopping power of their collective constituent atoms, and by the structure's atomic density (Zeigler et al 2008). Based on SRIM calculations the maximum in deposited collision energy by H^+ and He^+ at solar wind energies occurs at respective depths of approximately 11 nm and 23 nm for plagioclase and 8 nm and 20 nm for orthopyroxene. This maximum is likely to correspond to the rim width, because the deposited energy falls off rapidly beyond the maximum. Based on these relations, rims in feldspar can be expected to be wider than those in pyroxene, all other factors being equal. These simulations assume ion bombardment at fixed energies with one

ion type, unlike the energy range and multi-ion composition of the solar wind and only account for normal incidence of irradiation. Nonetheless, these are important first-order estimates for understanding the development of irradiated rims on airless body materials.

As noted above, there is the possibility that differences in exposure time may also play a role that is superposed on differences in the ion processing behavior of the two minerals. The narrow width of the rim on the plagioclase grain analyzed here (<25 nm) is significantly less than those observed on plagioclase grains in mature lunar soils, which range from 10-100 nm in thickness, with an average thickness of ~ 50 nm (Zhang and Keller 2012). The smaller rim thickness on the plagioclase grain from Itokawa would seem to suggest that its exposure time is therefore less than that for a mature lunar soil. However, although the orthopyroxene and plagioclase grains are part of one coherent assemblage now, it is possible that they did not exist cohesively during their entire surface exposure lifetime. The observed spatial relationship could be a product of sample-collection methods or the amalgamation of grains during a recent surface event, e.g., an impact. Such an event could group together grains with vastly different exposure times resulting in variable radiation-damage features.

The lack of distinct solar flare tracks may speak to the exposure history of this individual particle which our microtome slices are sourced from. It is possible that the lack of tracks identified here is a result of the inherent difficulty in identifying solar flare tracks in pyroxene minerals that exhibit a high concentration of strain features, including this grain. Another possibility, however, is that these grains were exposed for a very short period of time on the surface of Itokawa, preventing the accumulation of tracks in high enough density to measure. However, we note the difficulty in constraining relevant

surface residence times of material on Itokawa from the analysis of one single particle.

3.4.2 Multilayer Rim Features

The chemically heterogeneous layers we report here are distinct from the composite redeposition rims previously reported (Noguchi et al. 2014; Noguchi et al. 2011). The rims previously described are comprised of an outermost totally amorphous region, whereas the rims we report on here contain a multilayer, mixed nanocrystalline and amorphous morphology. We hypothesize two possible formation mechanisms for these features, or a combination of these processes, described below. The significantly different composition of the multilayer rims relative to the underlying grain (Fig. 3) suggests that the rims could be the product of vapor deposition from a micrometeorite impact of an adjacent grain with a different chemical composition. However, similar features in lunar soils attributed to micrometeorite impact events are typically amorphous because the vapor-deposited material is quenched at low temperatures, preventing the development of crystalline domains. As a result, the nanocrystalline nature of the outer layer in the multilayer rims may argue against this formation mechanism as it suggests that there was sufficient time for at least small grains to crystallize. A nearby heating event, e.g., a subsequent micrometeorite impact in the local surface region, could have provided enough thermal energy to slow quenching and allow for the outer layer to recrystallize.

Alternative processes for forming the chemically heterogeneous multilayer rims could also involve preferential solar ion sputtering of the grain surface itself, sputter deposition of material derived from surrounding grains, or a combination of the two processes (Hapke, 2001). For silicate minerals, the compositional relations that can develop

in the outer rims of grains involved in either of these processes, especially involving relative changes in the constituent cation concentrations like those observed here in the orthopyroxene rims, are still not well understood. Therefore it remains possible that either of these sputtering processes, or a sequence of the two processes, may have contributed to forming the compositional relationships in the inner and outer layers in the orthopyroxene rims.

3.4.3 Amorphous Islands

The amorphous islands are similar to lunar glass features that have been attributed to micrometeorite impact events (Keller and McKay 1997). Their relief from the underlying grain, completely amorphous crystal structure, and different chemistry when compared to the bulk grain beneath are similar to impact glasses in lunar soils that are ‘splashed’ onto the surface from adjacent material. We therefore infer that micrometeorite impacts produced the amorphous islands that we observe in these Itokawa samples.

3.4.4 Fe Nanoparticles

NpFe^0 particles have been produced experimentally through both irradiation experiments and simulated micrometeorite impacts using laser irradiation (Sasaki et al. 2001). Previous studies have attributed individual formation mechanisms to nanoparticles with specific chemistries. NpFe^0 particles associated with Mg and S are attributed to micrometeorite impact events and subsequent vapor deposition (Noguchi et al. 2011). These particles often occur close to the surface of the grain, in a matrix of completely amorphous material. In contrast, particles emplaced deeper into the grain that are not

associated with Mg or S but are instead, purely Fe, are suggested to have formed through radiation processing events (Noguchi et al. 2011). The data on the Fe nanoparticles observed in our Hayabusa particles suggest that they were produced through ion irradiation events because they occur in a matrix that is isochemical with the underlying grain and are also located deeper in the grain in a matrix of partially amorphous material. The relatively low concentration of these particles when compared to lunar samples may suggest a short exposure time on the surface of Itokawa, preventing the accumulation of high volumes of Fe nanoparticles. If this low concentration were characteristic of the population of space weathered grains on Itokawa as a whole, it may indicate that the spectral reddening characteristic of S-type asteroids can be produced with only a small amount of npFe⁰.

3.4.5 Vesiculated Textures

The vesiculated textures observed in our assemblages have been reproduced in experimental samples subjected to irradiation (Hishmeh et al. 1994). Such high concentrations of vesicles are rare in grain rims from mature lunar soils (Keller and McKay 1997), although vesiculated grain rims are commonplace in friable lunar breccias (Noble et al. 2005). Noble et al. (2005) proposed that the vesiculated rims result from thermal processing of the solar wind implanted grains. A similar thermal event may have produced the vesiculated rims we observe on the Itokawa grains.

The space weathering features observed in samples from Itokawa suggest that while radiation from solar energetic ions does play a significant role in surface alteration of this body, observed impact glasses suggest micrometeorite impacts also contribute to its significant and complex processing history. The surface environments of the Moon and

Itokawa are different, e.g., potentially higher resurfacing rates on Itokawa resulting in shorter grain exposure times and lower surface gravity resulting in lower retention of impact products. However, the data presented here suggest that the *processes* altering their surface characteristics are similar, although the *features* these processes generate are variable.

4.0 Conclusions

We examined the detailed microstructure and chemistry of particle RA-QD02-0042 returned by the Hayabusa mission. The particle contains an assemblage with a diverse mineralogy including orthopyroxene, plagioclase, olivine, Fe and Fe-Ni sulfides, and Fe-Ni metal. The data suggest that the grains on the surface of Itokawa have a complex processing history with contributions from both micrometeorite impacts and radiation processing events. Several characteristics, including the differences we observe in concentration and distribution of npFe⁰ particles in these samples, vary from previous observations of lunar soils. The discrepancies in these features are likely a product of different surface modification environments between the Moon and Itokawa and indicate that we should revisit our lunar soil collection for analysis in a new context.

5.0 Acknowledgements

We thank JAXA for the allocation of Hayabusa samples for this study. We gratefully acknowledge the use of facilities within the Leroy Eyring Center for Solid State Science at Arizona State University. We acknowledge the use of facilities and assistance from Huikai Cheng at FEI. The TEM work at the Johnson Space Center was supported in

part by a grant to LPK from the NASA Laboratory Analysis of Returned Samples (LARS) program. Funding for M. S Thompson is provided by the Natural Sciences and Engineering Research Council of Canada (NSERC). Research supported in part by NASA.

CHAPTER 4

THE OXIDATION STATE OF NANOPHASE Fe PARTICLES IN LUNAR SOIL: IMPLICATIONS FOR SPACE WEATHERING

Abstract

Here we report measurements of the oxidation state of Fe nanoparticles within lunar soils that experienced varied degrees of space weathering. We measured >100 particles from immature, submature, and mature lunar samples using electron energy-loss spectroscopy (EELS) coupled to an aberration-corrected transmission electron microscope. The EELS measurements show that the nanoparticles are composed of a mixture of Fe⁰, Fe²⁺, and Fe³⁺ oxidation states, and exhibit a trend of increasing oxidation state with higher maturity. We hypothesize that the oxidation is driven by the diffusion of O atoms to the surface of the Fe nanoparticles from the oxygen-rich matrix that surrounds them. The oxidation state of Fe in the nanoparticles has an effect on modeled reflectance properties of lunar soil. These results are relevant to remote sensing data for the Moon and to the remote determination of relative soil maturities for various regions of the lunar surface.

4.1 Introduction

Grains on the surfaces of airless bodies such as the Moon and asteroids are continually modified by micrometeorite impacts and interactions with solar-wind ions, processes that are collectively known as space weathering. This phenomenon alters the optical properties of surface soils by darkening and reddening their reflectance spectra and by attenuating their characteristic absorption bands (Hapke 2001). Understanding the changes to optical properties of surface samples on airless bodies is important because these processes have historically made it difficult to match meteorites to their parent asteroids, e.g., ordinary chondrites and S-type asteroids.

Changes in the optical properties of soils have been attributed to the production of iron nanoparticles in surface grains, often referred to as nanophase Fe (npFe), by space weathering processes. These iron nanoparticles occur as inclusions in agglutinitic lunar glasses formed by micrometeorite impact events, and as inclusions in amorphous rims on grains produced by vapor deposition and irradiation processes. The iron nanoparticles range in size from a few to several tens of nm; those in vapor-deposited and irradiation-produced surface rims typically average 3 nm in size in a mature lunar soil whereas those in grain interiors associated primarily with agglutinates are larger, averaging 7 nm in the same mature lunar soil. The size and distribution of these grains has important implications for the optical properties of lunar surface soils (Keller and Clemett 2001). Analysis of lunar

soils and experimentally created analogs show that nanoparticles <5 nm increase reflectance with increasing wavelength (reddden), whereas particles >10 nm lower the overall reflectance (darken) spectra of surface materials (Keller et al. 1998; Noble et al. 2007).

The nanoparticles in lunar soil samples are typically reported as containing Fe in the reduced metallic state, i.e., Fe^0 , and are widely identified as npFe⁰ in the literature, e.g., (Pieters et al. 2000). This hypothesis is based on the reducing nature of the environment in which npFe particles form, and the measured ferromagnetic resonance properties of lunar soils (Morris 1978). However, Keller and Clemett (2001) analyzed lunar agglutinitic glasses containing nanoparticles and showed that the Fe in these samples occurs as both Fe^0 and Fe^{2+} oxidation states. Their results suggest that a component of these samples, either the agglutinitic glasses, the nanoparticle inclusions, or both, are composed of mixed-valence Fe. However, direct measurement of the oxidation state of Fe in those nanoparticles was difficult at the time due to spatial and spectral limitations on nearly all available transmission electron microscopes (TEMs).

The presence of mixed-valence Fe has important implications for understanding the effect of npFe on the optical properties of surface samples and on airless body landscape evolution. The refractive properties of Fe vary with oxidation state, affecting the overall reflective properties of the soil in which they occur (Henning et al. 1995; Johnson and

Christy 1974). Experimental simulation of micrometeorite impacts and solar-wind exposure using laser and ion irradiation have both formed npFe (Loeffler et al. 2009; Sasaki et al. 2001). Thus, measurement of the oxidation state of individual Fe nanoparticles could help in constraining the nature of these formation mechanisms and the subsequent alteration of these features. Further, such measurements could provide insight into the nature of space-weathering processes on other airless bodies including near-Earth asteroids such as (25143) Itokawa, the target of the Hayabusa mission.

Over the past ten years, there have been dramatic improvements in electron optics. Development and implementation of spherical-aberration (C_s) correctors and monochromators in TEMs has pushed spatial resolution into the sub-Ångstrom scale and spectral resolution into the millivolt regime. Direct atomic-resolution imaging and spectroscopy has been realized and these techniques have been applied to electronic and other technologically relevant materials, (e.g., Krivanek et al. 2010; Muller et al. 2008; Varela et al. 2009). The application of such methods to earth and planetary materials has the potential to provide new insights into our origins at a fundamental atomic level. Here we apply electron energy-loss spectroscopy (EELS) coupled to a C_s -corrected and monochromated TEM to evaluate the oxidation state of individual Fe nanoparticles in lunar soil. We show that Fe occurs in mixed oxidation states and, combining these results with

spectral modeling, that these states affect the optical properties of the grains on airless body surfaces.

4.2 Samples and Methods

We embedded <1mm grains of three Apollo lunar soils in low-viscosity epoxy and prepared samples for TEM analysis through ultramicrotomy. This preparation technique has previously been used without any adverse effect on the oxidation state of Fe nanoparticles, e.g., Keller and Clemett (2001). The studied samples include: 79221, a mature mare soil; 15071 a submature mare soil; and 12033, an immature mare soil. These samples were chosen because they have similar bulk compositions, but have experienced a range of space weathering, classified from immature to mature. We collected images of our lunar soil samples using the 200 keV JEOL 2500SE analytical scanning TEM (S/TEM) at NASA Johnson Space Center equipped with bright-field (BF) and dark-field (DF) STEM detectors.

To measure the oxidation state of Fe in these nanoparticles we employed core-loss EELS coupled to a TEM. Over 100 individual nanoparticles were measured across all three samples, with over 30 from each sample occurring in several separate lunar soil grains. We analyzed nanoparticles that occur both in vapor-deposited rims around grains and in the interiors of glassy agglutinate grains.

All EELS analyses were performed using the 100 keV monochromated and C_s-corrected Nion UltraSTEM at Arizona State University (ASU), equipped with a Gatan Enfium spectrometer. Operating conditions included a convergence semi-angle of 30 mrad, a 0.2 nm probe size, 3 mm spectrometer entrance aperture and a collection angle of 45 mrad. We collected EELS spectra with the monochromator on, which provided an energy resolution between 200 to 300 meV as measured from the full-width half-maximum height of the zero-loss peak (ZLP). Individual nanoparticles were measured via line profiles using a 0.1 eV/channel dispersion and a variable dwell time, ranging from 0.01s/px to 0.5 s/px, and a probe current of 0.5 nA. The energy dispersions for the spectrometer were calibrated during each analysis session by measuring the shift of the ZLP with automated routines in the DigitalMicrograph software package used to acquire EELS data.

To assess the effect of sample thickness on spatial resolution of the STEM probe, we calculated the amount of beam broadening that a 0.2 nm probe would experience in the sample. Using equation 36.1 from Williams and Carter (1996):

$$(4.1) \quad b = 8 \times 10^{-12} \frac{Z}{E_o} (N_v)^{1/2} t^{3/2}$$

where b is the beam broadening (m), Z is the average atomic number of the sample, E_o is the beam energy (keV), N_v is the number density of atoms (atoms/m³), and t is the thickness of the sample (m). We calculated a beam broadening parameter, b , to be 3.82 nm, based on a 100 keV accelerating voltage, an average atomic number of 11.4, assuming

clinopyroxene, which composes a significant proportion of the mineral fragments in mare soils, a sample thickness of 60 nm (the ultramicrotome slice thickness), and N_v of 8.2×10^{28} atoms/m³ (based on clinopyroxene cell parameters). To find the realized beam size after broadening effects, we used equation 36.2 from Williams and Carter (1996):

$$(4.2) \quad R = (b^2 + d^2)^{1/2}$$

where R is the realized beam diameter (m), b is the beam broadening parameter described above (m), and d is the incident beam diameter (m). Using the calculated broadening parameter and our incident beam diameter of 0.2 nm, the realized beam diameter is 3.84 nm. This beam diameter is small enough to measure accurately the microstructural features we describe throughout the manuscript.

Spectral processing involved multiple steps. We removed the background from each spectrum, in the form of AE^{-1} , and deconvolved the ZLP using the Fourier-Ratio method (Egerton 1996). We note that the diameter of most particles is <10 nm. As such, the three-dimensional size, assuming the particles are spheres, is less than the overall thickness of the ultramicrotomed thin section (≥ 60 nm). Thus, EELS spectra obtained from the nanoparticles include a contribution from the surrounding glassy material lying above and/or below the nanoparticle in cross section. This surrounding matrix material can contain a mixture of Fe oxidation states in proportions unequal to that of the nanoparticle itself (Keller and Clemett 2001). In order to account for this effect and isolate the

contributions to the collected spectra solely from the nanoparticle, we collected line profiles that transect both the nanoparticle and the matrix material surrounding it. After performing background and ZLP corrections for both the matrix and nanoparticle spectra, we subtracted the average matrix component from the average nanoparticle spectrum, leaving a residual spectrum that is representative of the nanoparticle without matrix effects. From this residual spectrum, we subtracted the continuum intensity beneath the Fe $L_{2,3}$ edge on all spectra using a linear fit between 702 to 725 eV. We note that the continuum intensity has been successfully modeled based on linear and step-function (arctan) fits between edge onset and post-edge energies (Garvie and Buseck 1998; van Aken et al. 1998).

We determined the Fe oxidation state of nanoparticles by performing a flux-weighted, linear, least-squares fit between the observed EELS spectra and the spectra of three Fe oxidation end-members: Fe⁰ (Fe metal; 99.98% purity), Fe²⁺ (FeO, wüstite; 99.9% purity), and Fe³⁺ (Fe₂O₃, hematite; 99.9% purity). The wüstite and hematite standards were embedded in epoxy and prepared for the TEM using ultramicrotomy, whereas the Fe metal sample was prepared via focused ion beam (FIB) using the FEI Nova 200 NanoLab FIB at ASU. The standards were measured using the same operating conditions as described above, in order to model quantitatively the measured spectrum from the nanoparticle. The Fe-oxidation-state ratios were quantified using the L_3 edge because it exhibits edge-onset and multiplet peak structure that is indicative of oxidation state. The observed edge onset

of each of these standard spectra are consistent with literature data, e.g., Garvie et al. (1994), van Aken et al. (1998), Zega et al. (2003). The best-fit spectrum, \mathbf{d}^{fit} , can then be written as the linear combination of the spectra of these three end-members:

$$(4.3) \quad \mathbf{d}^{\text{fit}} = f_{\text{Fe}^0} \mathbf{d}_{\text{Fe}^0} + f_{\text{Fe}^{2+}} \mathbf{d}_{\text{Fe}^{2+}} + f_{\text{Fe}^{3+}} \mathbf{d}_{\text{Fe}^{3+}}$$

where f_{Fe^0} , $f_{\text{Fe}^{2+}}$, $f_{\text{Fe}^{3+}}$, are the relative weights of each end-member spectra, and \mathbf{d}_{Fe^0} , $\mathbf{d}_{\text{Fe}^{2+}}$, $\mathbf{d}_{\text{Fe}^{3+}}$ are the end-member spectra (each $n \times 1$ vectors, where n is the number of data points in each spectrum). These best-fit weights can be determined from weighted damped least squares, (e.g. Menke 2012). Fe-oxidation-state ratios are determined from normalizing the best-fit weights:

$$(4.4) \quad \% \text{Fe}^0 = \frac{f_{\text{Fe}^0}}{(f_{\text{Fe}^0} + f_{\text{Fe}^{2+}} + f_{\text{Fe}^{3+}})} * 100\%$$

and similarly for Fe^{2+} and Fe^{3+} . Goodness of fit is evaluated using the coefficient of determination, R^2 , where values of R closer to 1 imply better fits to the observed spectrum. Spectra with an R^2 value of >0.9 were accepted as having a reasonable fit (over 80% of the measured spectra) and are reported on here. The fitting program can be found in Appendix B.

Electron-beam induced damage can alter the oxidation state of Fe-bearing materials. For example, Garvie et al. (2004) showed that Fe in cronstedtite can oxidize during EELS analysis and so care must be taken to acquire spectra free of damage effects.

Thus, the potential for beam damage to affect the oxidation state of the npFe was considered during this investigation. Beam-damage effects can be observed physically and/or chemically. Physical damage can manifest in the form of amorphization or, in extreme cases, the sputtering of material in the measured area. In comparison, chemical damage can take the form of oxidation or reduction. The nature of the damage depends on the material and the experimental conditions. As a general approach to our measurements, we minimized probe dwell times so as to limit electron-beam/sample interaction. Further, we looked for qualitative real-time changes in the EELS spectra, i.e., shifting of the edge onset and/or changes in the fine structure that would suggest oxidation or reduction of the Fe. Initially, we observed both physical and chemical damage effects when using the full probe current and a long dwell time. Such effects prompted a systematic lowering of the probe current and dwell times until neither physical nor chemical damage was observed. The same collection parameters were used in the analysis of each lunar soil sample. If changes in oxidation state ratios resulted from electron beam damage, we would expect to see the resulting oxidation/reduction trend in *all* of the measurements, which we do not observe.

To evaluate the effect of oxidized Fe on the spectral properties of lunar soil, we simulated reflectance spectra with inclusions of npFe in different oxidation states. We developed a reflectance model based on the theory described in Hapke (2001) and Hapke

(2012). We simulated the bidirectional reflectance spectrum of a lunar regolith by modeling a mixture of pulverized rock and glass from lunar rock sample 10022 after Hapke (2001), to which increasing amounts of npFe in different oxidation states (Fe^0 , Fe^{2+} , or Fe^{3+}) were added. We modeled the soil as a particulate surface in which the particles are assumed to be isotropic scatterers, and the opposition effect is ignored (Hapke 2001). Our model spectra cover visible (VIS) and near infrared (IR) wavelengths relevant for observing space weathering effects (i.e., $0.25 - 1.8 \mu\text{m}$) and for interpretation of remote observations, including those from the Lunar Reconnaissance Orbiter (LRO) Wide Angle Camera (LROC/WAC; $0.41 - 0.69 \mu\text{m}$), and the Moon Mineralogy Mapper (M^3) on Chandrayaan-1 ($0.42 - 3.0 \mu\text{m}$) (Robinson et al. 2010; Green et al. 2011).

In order to simulate the spectral reflectance of the weathered regolith we follow the procedure explained in section 8 of Hapke (2001). We begin by calculating the absorption coefficient of an unweathered host soil (α_h) from the linear addition of the individual absorption coefficients of the pulverized rock and glass from sample 10022. These were calculated from the measured reflectances of each component, using the inverted reflectance equations (13) – (23) of Hapke (2001), and assuming equal proportions of rock and glass. We then add the absorption coefficient of the npFe inclusions to find the weathered absorption coefficient: $\alpha_w = \alpha_h + \alpha_{\text{Fe}}$, where α_{Fe} is a volume-weighted linear addition of the absorption coefficients of each Fe oxidation state. To model the inclusion

of oxidized states of Fe, we used the complex refractive indices of FeO and Fe₂O₃ as proxies for Fe²⁺, and Fe³⁺ respectively. The individual absorption coefficients of the iron phases were calculated from equations (11) and (12) of Hapke (2001), in which the values of the real and imaginary parts of the refractive indices were taken from Johnson and Christy (1974) for Fe, Henning et al. (1995) for FeO, and Tanaka (1979) and Triaud (unpublished) for Fe₂O₃. As in Hapke (2001), the reflectance spectra of our model weathered soil was compared to that of the weathered mare soil of sample 10084. We also modeled mixtures of oxidation states that represent the average compositions of nanoparticles measured from the immature (99% Fe⁰, 0.4% Fe²⁺, 0.6% Fe³⁺), submature (83% Fe⁰, 16% Fe²⁺, 1% Fe³⁺), and mature (14% Fe⁰, 71% Fe²⁺, 15% Fe³⁺) soils and simulated their addition to the unweathered spectrum.

4.3 Results

4.3.1 EELS Measurements

EELS spectra were collected as line profiles for over 30 nanoparticles from each sample, e.g., Fig. 4.1. The nanoparticles found in immature sample 12033 often appear more euhedral in shape than those in mature sample 79221. EELS spectra of nanoparticles containing Fe⁰, Fe²⁺, or Fe³⁺ have distinct $L_{2,3}$ edge onsets and structures. Fe⁰ spectra have the lowest energy onset (702.0 eV), with a ~1.5 eV chemical shift between each of the

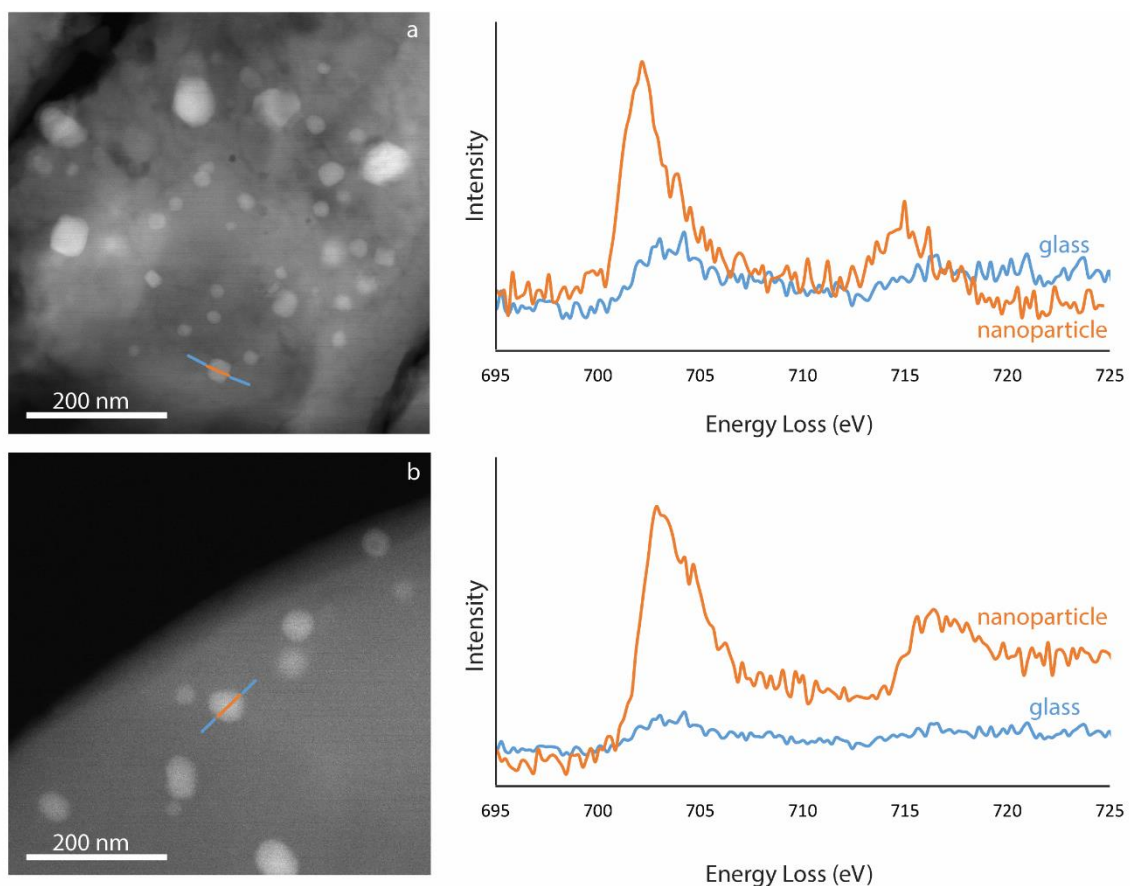


Figure 4.1: STEM imaging and EELS spectra for nanoparticles in both mature and immature samples (A) STEM-HAADF image of a nanoparticle in immature soil 12033 (left panel). EELS line profile across agglutinate glass (blue) and a nanoparticle (orange), right panel. The magnitude of the Fe peak in the EELS spectrum extracted from both the glassy matrix and the nanoparticle itself is shown. (B) STEM-HAADF image of a nanoparticle in mature soil 79221. NpFe in immature soils are euhedral, whereas those in more mature soils appear more spherical.

subsequent onsets of Fe^{2+} (703.5 eV) and Fe^{3+} (705.0 eV). Nanoparticles that contain primarily one oxidation state exhibit EELS spectra with a single peak structure (Fig. 4.2a). Nanoparticles composed of two oxidation states, e.g., Fe^0 and Fe^{2+} or Fe^{2+} and Fe^{3+} , exhibit two-peaked L_3 edges (cf., Fig 4.2b,c) with a shape intermediate between their two oxidation-state components (Garvie et al. 1994; van Aken et al. 1999; Zega et al. 2003). The majority of particles analyzed here have a two-peak structure, with only contributions

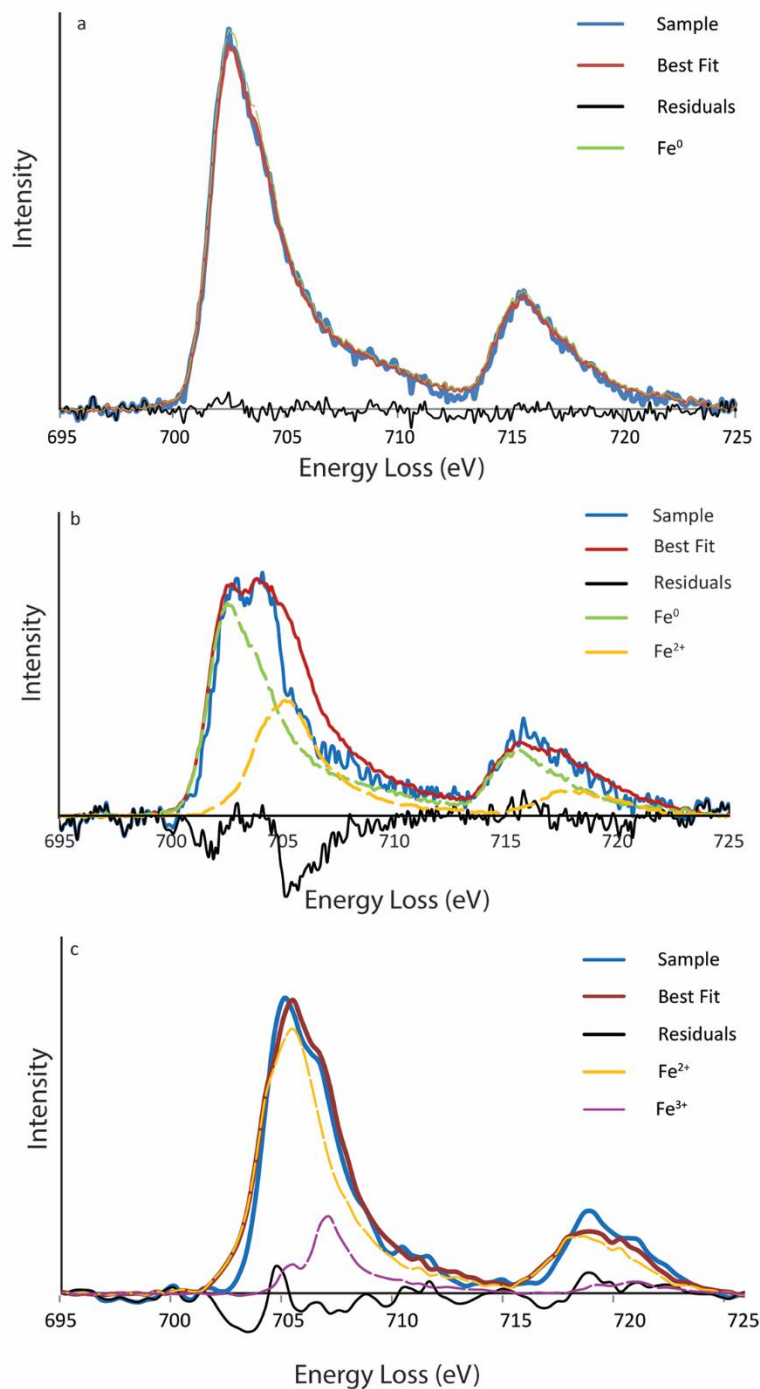


Figure 4.2: Quantified EELS spectra of nanoparticles. (A) Immature lunar soil sample 12033. The measured sample (blue), the best fit (red), the fit residuals (black), and the components fitting the spectrum, in this case Fe^0 (green) are shown. This particle is composed of 100% Fe^0 . (B) Submature lunar soil sample 15071. Colors for spectra are the same as in (A) except we have included the Fe^{2+} (gold) component. This particle is composed of 67% Fe^0 and 33% Fe^{2+} , (C) Mature lunar soil sample 79221. Colors for spectra are the same as in (b) except we have included Fe^{3+} (purple) components. This particle is composed of 45% Fe^{2+} and 55% Fe^{3+} .

from two standard end members. While we did not observe three-peaked spectra, a small proportion of the nanoparticles are best modeled with contributions from each oxidation state (i.e., Fe^0 , Fe^{2+} , and Fe^{3+}). The changes in the relative heights of the two-peaked L_3 edge qualitatively reflect changes in the ratio of particular Fe oxidation states to total Fe, defined herein as Fe^0 to total Fe ($\text{Fe}^0/\Sigma\text{Fe}$), Fe^{2+} to total Fe ($\text{Fe}^{2+}/\Sigma\text{Fe}$), and Fe^{3+} to total Fe ($\text{Fe}^{3+}/\Sigma\text{Fe}$). Fe-valence ratios were calculated for each spectrum using the flux-weighted, linear, least-squares method described above. Typical uncertainties in mixing ratios are 1 to 3%. The uncertainties were evaluated in a Monte-Carlo fashion, where we repeated each least squares fit several hundred times with random noise injected into each standard and sample. The random noise added to each spectrum was normally distributed with a standard deviation equivalent to the standard deviation in each observed spectrum shortward and longward of the L_2 and L_3 peaks. Variances in the spectra beyond these peaks likely represent random instrumental noise. The final mixing ratio uncertainty was taken as the standard deviation of the resulting suite of Monte-Carlo fits. An example best-fit spectrum for a particle from each lunar sample is shown in Fig. 4.2.

The quantified valence ratios for the various soil maturities are shown in ternary space (Fig. 4.3). Spectra collected from immature soil sample 12033 are composed mostly of Fe^0 , with 84% of particles composed of 100% Fe^0 . The remaining 16% of particles contain between 88 and 98% Fe^0 and residual amounts of Fe^{2+} and Fe^{3+} . The nanoparticles

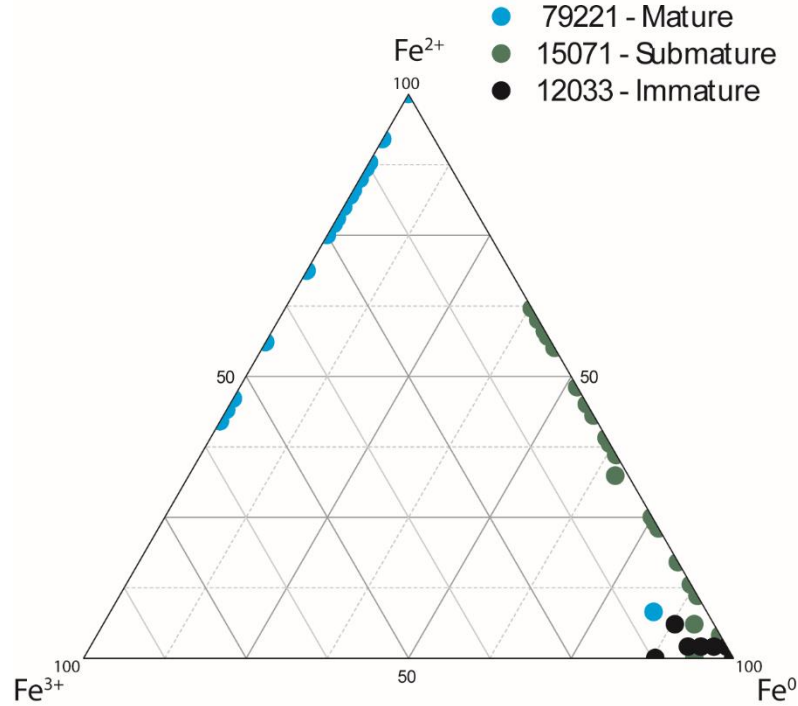


Figure 4.3: Ternary plot showing compositions of nanoparticles in each of the lunar soil samples.

from the submature soil 15071 have Fe^0 compositions ranging between 38 to 100% with the remaining Fe in each particle primarily composed of Fe^{2+} . A selection of the nanoparticles measured in submature soil 15071 contain an oxidized shell surrounding a reduced core (discussed below). In comparison, spectra collected from nanoparticles in mature sample 79221 have the greatest variety of Fe oxidation states, with Fe^0 and Fe^{2+} compositions each ranging from 0 to 100%, and Fe^{3+} ranging from 0 to 56%, although the fraction of nanoparticles with such a high Fe^{3+} content is low ($\leq 15\%$ of the total nanoparticle have $\text{Fe}^{3+} > 25\%$). The EELS results show a trend of increasing nanoparticle oxidation with increasing soil maturity; nanoparticles in immature soil (12033) are

composed primarily of Fe^0 , whereas those in the submature soil (15071) are a mixture of Fe^0 and Fe^{2+} , and nanoparticles in the mature soil (79221) are a mixture of Fe^{2+} and Fe^{3+} .

We note that these results should be considered in the context of measurement statistics. Due to sample thickness requirements for the EELS measurements, grains that were adequately thin and contain a high density of large Fe nanoparticles were often chosen for analysis. These grains may be among the most mature in the soil, and could contain a relatively larger fraction of oxidized Fe. Over-counting of such particles could introduce a sampling bias that is not representative of the average soil. These results do not preclude the presence of Fe^0 nanoparticles in mature soils. Our results indicate that 40% of nanoparticles in mature soil 79221 contain *no* Fe^{3+} , and >15% of those mature nanoparticles measured here contain >80% Fe^0 . These findings simply indicate there is oxidized Fe present in the nanoparticles of mature lunar soils, but it is not the most abundant Fe component.

4.3.2 Particles with Oxidized Rims

A subset of particles in the submature soil (sample 15071) contain oxidized Fe in their outer edges. Quantification of EELS line profiles show that the outer three nm (on average) of these particles is composed primarily of Fe^{2+} , whereas the interior material is composed predominantly of Fe^0 (Fig. 4.4). This reduced-core/oxidized-shell structure was

found in over 10 npFe particles that were measured in agglutinitic glass grains. This structure was only observed in nanoparticles in the submature soil, indicating it is not the result of a measurement or spectral processing artifact.

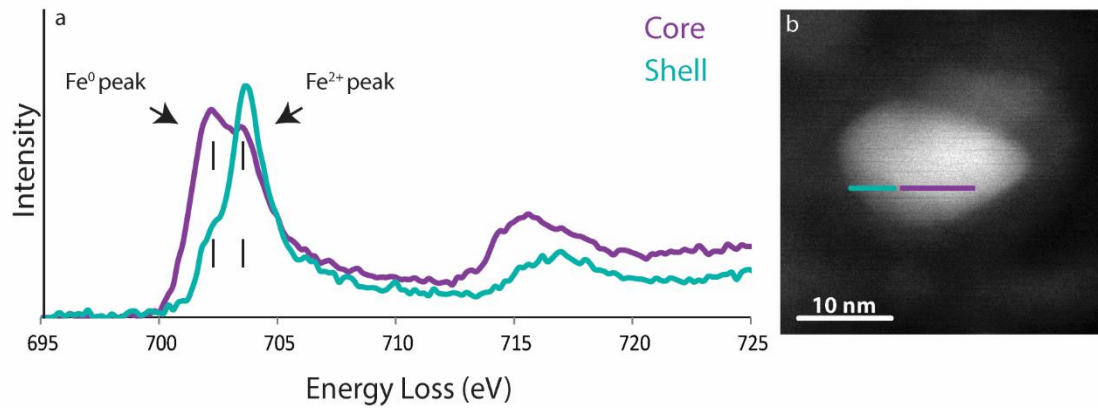


Figure 4.4: TEM data for a core-shell particle. (A) EELS spectra for the shell and core of the nanoparticle shown in the HAADF image (B). The shell of the nanoparticle gives a two-peaked spectrum, containing 16% Fe⁰ and 84% Fe²⁺. The core contains 79% Fe⁰ and 21% Fe²⁺.

4.3.3 Hollow NpFe Particles

We collected STEM BF and DF images of npFe particles in each lunar soil sample. Ten nanoparticles in sample 79221 contain dark cores surrounded by bright-contrast shells (Fig. 4.5), suggesting that they contain a central void. As npFe is typically smaller in diameter than the thickness of the ultramicrotomed thin section, nanoparticles containing central voids may not be recognized unless the section surface happens to transect the nanoparticle core, e.g., Fig. 4.5. These types of nanoparticles may be in higher abundance than recognized here or in previous studies.

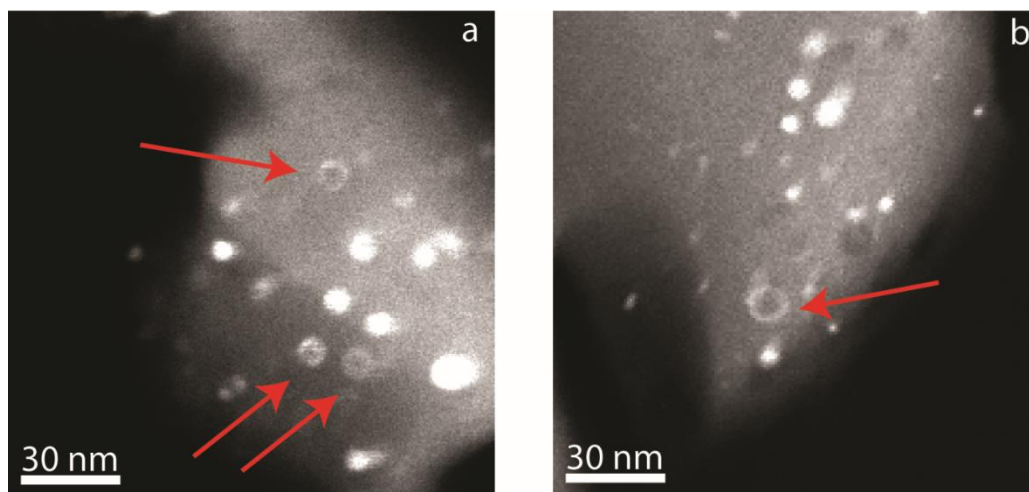


Figure 4.5: DF STEM images of hollow Fe nanoparticles in mature soil sample 79221, indicated by red arrows.

4.3.4 High Resolution STEM Imaging

We performed STEM imaging of npFe particles in each of the three lunar soils to obtain high-resolution images of their structures. We measured interplanar d -spacings in one or two directions, as the data allowed, for each particle from these images (Fig. 4.6a-c). Measurements of npFe particles from immature sample 12033 give d -spacings consistent with Fe metal (Fig. 4.6a, Table 1). Measurements of d -spacings from submature sample 15071 are consistent with FeO, i.e., wüstite containing Fe^{2+} (Fig. 4.6b, Table 1). In comparison, the measured d -spacings for mature sample 79221 overlap with those of several Fe-oxide minerals (Fig. 4.6c, Table 4.1), i.e., wüstite, magnetite, and hematite, indicating possible Fe^{2+} and Fe^{3+} oxidation states. These structural measurements are consistent with the Fe oxidation states measured through EELS for each of the lunar samples.

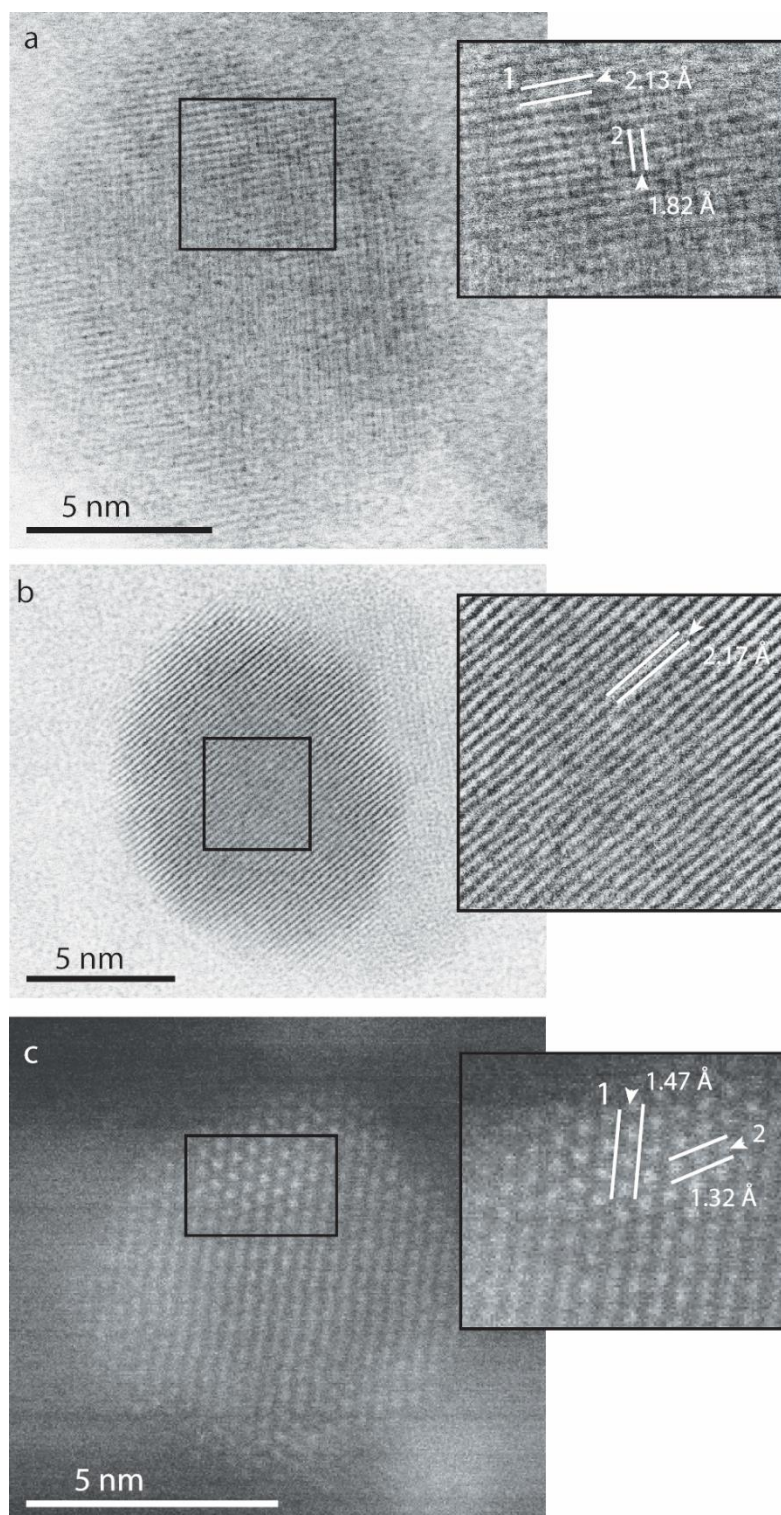


Figure 4.6: High resolution STEM images of nanoparticles in lunar soils. (A) BF STEM image of nanoparticles in immature soil sample 12033. The measured d -spacings are consistent with Fe^0 , (B) BF STEM images of submature soil sample 15071. The measured d -spacings are consistent with FeO (wüstite), (C) HAADF STEM image of a nanoparticle in mature lunar soils sample 79221. The measured d -spacings are consistent with Fe_3O_4 (magnetite).

Table 4.1: Measured d -spacings for npFe in lunar soil.

Sample	Measured d -spacings (Å)	Possible matching phase	d -spacing for matching phase (Å)	Miller index
12033 - Immature	2.13	Fe Metal	2.11	(111)
		Wüstite	2.16	(200)
	1.82	Fe Metal	1.82	(200)
15071 - Submature	2.17	Wüstite	2.16	(200)
79221 - Mature	1.47	Magnetite	1.48	(404)
	1.32	Magnetite	1.32	(026)
			1.28	(353)
		Wüstite	1.29	(113)
		Fe Metal	1.29	(220)

4.3.5 Spectral Modelling

The results of our spectral reflectance models indicate significant differences in the behavior of certain spectral characteristics of space-weathered soils due to the Fe oxidation states in npFe (Fig. 4.7). Including only Fe^0 in the nanoparticles causes attenuation of the 1.0 μm absorption band, and creates a significantly darkened spectrum overall, when compared to the unweathered components (Fig. 4.7a). An oxidation state of Fe^{2+} in the npFe reduces the reddening effect of weathering through the mid wavelengths (0.5-1.5 μm), although the attenuation of absorption bands is similar to the addition of Fe^0 (Fig. 4.7a). An oxidation state of Fe^{3+} in the npFe increases the reddening effect at wavelengths $>0.5 \mu\text{m}$. In addition, the magnitude of the attenuation at the 1.0 μm silicate absorption band is slightly reduced in Fe^{3+} when compared to Fe^{2+} or Fe^0 . Most noticeably however,

the simulated spectrum is significantly redder and brighter with Fe^{3+} inclusions compared to that with Fe^{2+} or Fe^0 (Fig. 4.7a).

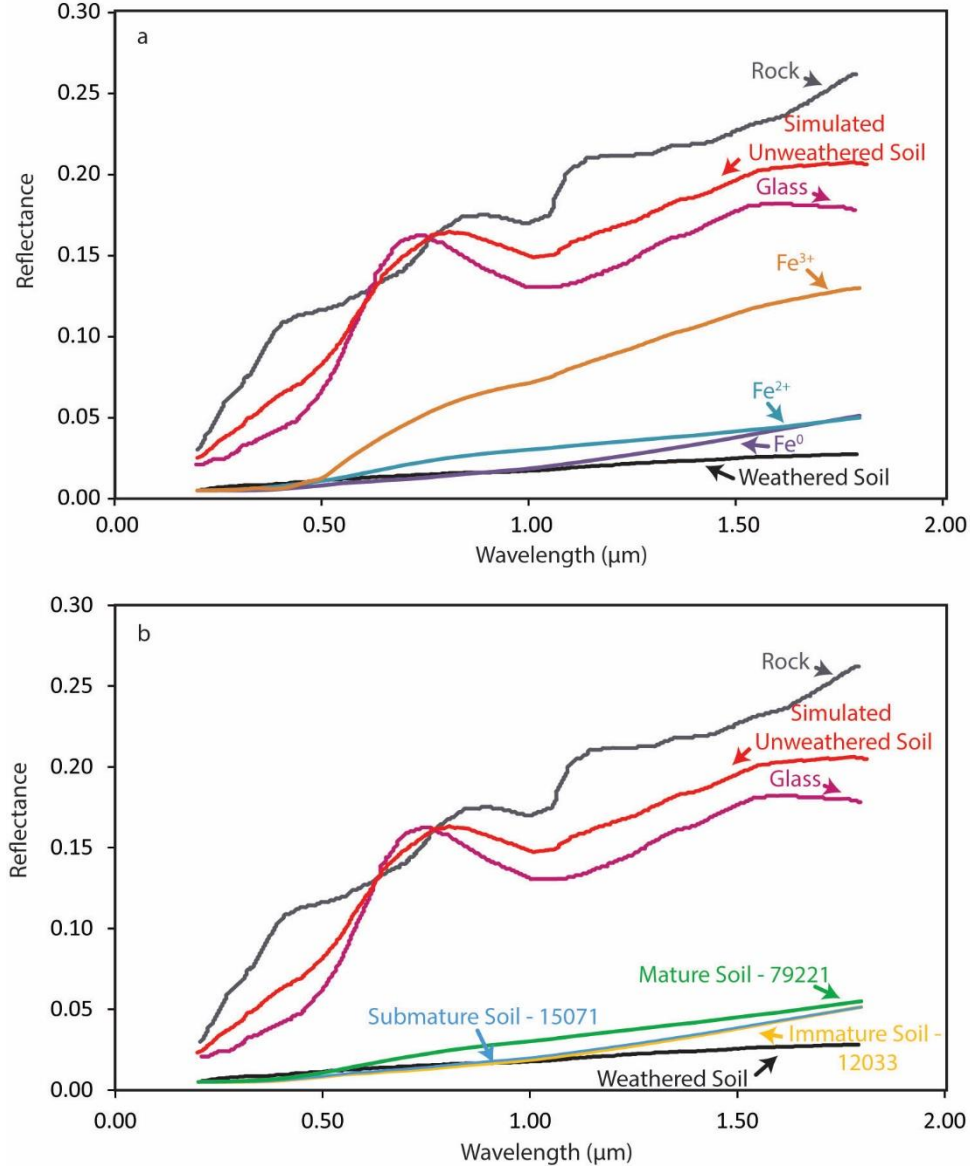


Figure 4.7: Simulated reflectance spectra of lunar soil. (A) Simulated unweathered soil spectrum (red) from rock (grey) and glass (magenta) components and oxidation state end-members spectra for nanophase Fe inclusions, with Fe^0 (purple), Fe^{2+} (blue), and Fe^{3+} (orange). A measured weathered soil spectrum is shown (black) for reference. (B) Unweathered components shown as in (A). Mixtures of Fe oxidation states with proportions measured from lunar soils, the immature with 99% Fe^0 , 0.4% Fe^{2+} , and 0.6% Fe^{3+} (gold), submature with 83% Fe^0 , 16% Fe^{2+} , and 1% Fe^{3+} (blue), and mature with 14% Fe^0 , 71% Fe^{2+} , and 15% Fe^{3+} (green). A measured weathered soil spectrum is shown (black) for reference.

We also simulated mixtures of Fe oxidation states that are representative of the compositions from each of the lunar soils, as measured using EELS (Fig. 4.7b). The results for the immature and submature soils are virtually indistinguishable from one another and are very similar to the measured weathered soil spectrum, although slightly reddened. The mature soil, with the highest proportion of Fe^{3+} , is brighter than the submature and immature samples.

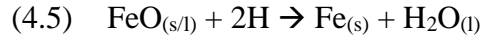
4.4 Discussion

4.4.1 Crystal chemistry and structure

The EELS measurements show that there is a trend of increasing Fe oxidation state in nanoparticles with increasing soil maturity. The most mature soils have significant exposure times on the lunar surface and as such have experienced prolonged weathering processes. These data suggest that increased weathering time leads to increased oxidation of npFe. Several mechanisms have been proposed to describe the development of npFe particles through space weathering.

One process, which was a long-standing paradigm in lunar sample science, proposes that hydrogen (H^+) is implanted into surface soils by solar-wind irradiation and functions as a reducing agent (Hapke 2001). When these H-bearing soil grains experience melting and/or vaporization as a result of a subsequent micrometeorite impact, oxide

molecules, including FeO, are liberated from the crystal structure of the grain. The implanted hydrogen acts to reduce the Fe in the melt or vapor, via the reaction:



This pathway is expected to produce metallic Fe in lunar surface grains, and has been invoked to explain nanoparticles in agglutinate grains, which are interpreted to be melt products e.g., (Housley et al. 1973). However, Fe nanoparticles also occur in amorphous rims of plagioclase grains, which have no native Fe that could otherwise be reduced, and so reaction (3) is unable to explain all observed npFe in lunar soils. Moreover, several laboratory experiments that simulate solar-wind irradiation with only He ions have demonstrated the development of Fe nanoparticles, without any implanted hydrogen e.g., (Loeffler et al. 2009). These results suggest that while nanoparticle production via reaction (3) may be occurring on the lunar surface, it cannot be the sole process by which Fe particles are produced.

Another mechanism, first proposed by Hapke et al. (1975), involves ion-irradiation of surface grains resulting in sputtered and redeposited material onto adjacent grains. This theory gathered support with the discovery of vapor-deposited rims in lunar soils (Keller and McKay 1993, 1997). In this ion-irradiation scenario, if O atoms are preferentially sputtered, a localized reducing environment is created on the surface of the particle, which can cause the Fe in the residual material to become reduced. The sputtered O has a low

sticking coefficient, does not readily adhere to any adjacent surfaces, and is subsequently lost from the system. In contrast, as cations from the target are sputtered and redeposited onto an adjacent surface, a localized reducing environment is created on the target substrate, causing the reduction of redeposited Fe to the metallic state and the formation of nanoparticles.

A related mechanism has also been proposed for micrometeorite impacts. Oxide molecules are vaporized in the target material during an impact event, e.g., SiO, MgO, FeO. In this vapor cloud, FeO molecules have the lowest binding energy (Hapke 2001) and consequently dissociate, resulting in independent Fe and O atoms. O, being the more volatile species, will prefer to stay in the vapor, whereas Fe will condense as nanoparticles in the surrounding glassy matrix. This formation scenario is problematic for nanoparticles in lunar agglutinates as these grains are associated with a melting process and not vapor deposition e.g., Papike et al. (1982).

The data presented herein do not preclude any of these processes. The npFe could have been formed through a combination of these processes occurring on the surface of the moon and other airless bodies. These processes, however, are not static. The EELS data show that the npFe in the mature soils have an oxidized Fe component, whereas those particles in the immature soils contain abundant reduced Fe. Therefore, the products of space weathering, such as npFe particles, are continually evolving after their initial

formation. Mature soils have significant exposure times on the lunar surface and as such are subjected to the most prolonged weathering processes. The nanoparticles in these soils have experienced both microchemical and microstructural changes over their long lifetimes on the Moon's surface. The more spherical nature of nanoparticles in mature soils, compared to the euhedral appearance of those in the immature soil, suggest a history of microchemical processing.

There have been prior identifications of Fe^{3+} in lunar soils using techniques including RAMAN and Mössbauer spectroscopy, magnetic susceptibility, electron spin resonance studies and electron microprobe (e.g., Griscom and Marquardt 1972; Forester 1973; Dikov et al. 2009; Yakovlev et al. 2009; Ramdohr and El Goresey 1970; Weeks et al. 1970, 1972; Kolopus et al. 1971; Runcorn et al. 1971; Bell et al. 1974; Dąbrowski et al. 2008; Pasieczna-Patkowska et al. 2008; Shearer et al. 2014). These results are often met with skepticism as the analyses of Fe^{3+} -bearing phases were not confirmed through multiple analytical techniques. In addition, some of these results were shown to have been caused by oxidation in the terrestrial atmosphere (Griscom 1974; Housley et al. 1974). However, a recent study by Joy et al. (2015) shows, using multiple analytical techniques, that the Fe^{3+} -bearing phase magnetite occurs in lunar samples. Joy et al. (2015) suggest that magnetite formed through the desulfurization of troilite in the presence of an oxidizing

agent such as H_2O or CO_2 . These oxidizers may be sourced from low-temperature volcanic gases, impact vapor plumes, or impact-driven degassing of volatile-bearing regoliths.

Insight into the pathway of oxidation for npFe is provided by observations of nanoparticles in submature soil 15071. This sample is intermediary between metallic npFe in immature samples and oxidized npFe in mature samples, and their compositional differences correlate with changes in the nanoparticles' structure over time. NpFe in immature samples exhibit structures consistent with metallic Fe (bcc and fcc). Submature nanoparticles have structures matching to Fe and Fe oxide minerals, e.g., FeO (wüstite). Mature samples have nanoparticles structures matching a variety of Fe-oxide minerals, e.g., FeO, Fe_3O_4 (Fig. 4.6). We explore the source of this O below.

In the formation mechanisms described above, O previously bonded to Fe, is being lost from the system, with the residual O remaining in the matrix. The most abundant source of O is therefore the glassy matrix that surrounds the npFe, and we hypothesize that it is the oxidizing source of the npFe. Oxidation is nearly complete in the case of the mature sample, whereas the immature sample is composed of primarily Fe^0 nanoparticles, suggesting oxidation has not yet had time to significantly affect these samples. Fe nanoparticles may initially form in the metallic Fe state in reducing environments through one or several of the mechanisms described above. Subsequent oxidation of npFe in lunar soils could have occurred through one of several diffusion mechanisms described below.

Understanding the oxidation of Fe nanoparticles is an active field of research in the materials-science community. Fe nanoparticles, similar to those found in lunar soils, are used in a variety of biomedical and environmental applications. Due to their large surface area-to-volume ratio, Fe metal nanoparticles are highly reactive and especially prone to rapid oxidation (Bødker et al. 1994; Roy et al. 1996). Experimental work has shown that thin, oxidized films can form on Fe and other metal surfaces in only minutes when in the presence of O, even at extremely low temperatures e.g., <100 K (Cabrera and Mott 1949). Oxidized films have also formed on surfaces of Fe metal nanoparticles that are coated in other substrates, e.g., Au, where O is hypothesized to diffuse through grain boundaries in the Au coating to oxidize the metallic core, despite no direct exposure of the metal to atmosphere (Cho et al. 2005). Such nanoparticle oxidation can proceed rapidly, forming a thin oxidized film on metallic surfaces up to ~2.0 nm in thickness in minutes (Cabot et al. 2007; Cabrera and Mott 1949). The initial growth rate of oxide layers may slow substantially but will proceed up to ~10 nm in total thickness (Cabot et al. 2007).

In synthetic nanoparticles, O initially adsorbs to and oxidizes the surface layer of the nanoparticle. The electrostatic potential difference of this adsorbed O drives electron transport from the metallic Fe core to the O on the recently formed surface oxide layer (Cabot et al. 2007; Cabrera and Mott 1949). This electron transport occurs through quantum tunneling (up to an oxide layer ~3 nm in thickness) at lower temperatures (<423

K), or through thermoemission of electrons from the Fe core into the oxide conduction band at higher temperatures (>423 K). Oxygen on the surface of the nanoparticle creates an electric field capable of driving ion diffusion (Cabot et al. 2007; Cabrera and Mott 1949), and so oxidation continues through the outward diffusion of Fe from the metallic core, through the oxide layer, to the surface of the nanoparticle where it interacts with the adsorbed O. This diffusion process leaves vacancies in the core of the nanoparticle that coalesce into a central void (Cabot et al. 2007).

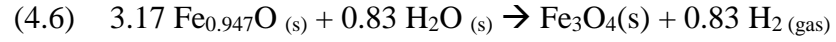
In the context of space weathering, airless bodies such as the moon lack an O-containing atmosphere, and so the npFe acquires O from the surrounding soil over time. We hypothesize that a solid-state diffusion gradient exists between the npFe and the agglutinate matrix, resulting from lack of charge neutrality, and/or unsatisfied bonds in the nanoparticle as a result of fast quenching times on the lunar surface. The diffusion rate of O to the nanoparticle surface may accelerate intermittently during episodes of nearby heating events, e.g., micrometeorite impacts. The timescales for oxidation of npFe grains are likely significantly longer than those proposed for synthetic nanoparticles, given the extreme differences in oxygen fugacity experienced by lunar soil grains and those produced in laboratories on Earth. It is possible that the npFe particles in the immature lunar soil, composed primarily of Fe^0 , may have already experienced a rapid, small degree of

oxidation on the surface of the Moon, evidenced by the minor oxidized Fe component of these nanoparticles.

Oxidized shells on nanoparticles, formed through diffusion mechanisms described above, were shown to be capable of developing long-range order (Bødker et al. 1994; Cabot et al. 2007). After prolonged oxidizing conditions, a hollow core may develop in nanoparticles (Cabot et al. 2007). As shown here, hollow nanoparticles occur in mature lunar soil sample 79221 (Fig. 4.5). This observation lends credence to the hypothesis that Fe is diffusing outward to the surface in contact with the O-containing glass. Such diffusion produces vacancies in the core of the particle leading to breakdown of long-range order and the creation of voids. We note that voids have also been reported in the cores of Fe and Fe-sulfide particles in GEMS grains (Matsuno et al. 2015), which may have formed through similar processes.

The glass matrix in which the Fe nanoparticles occur contains Fe in the Fe^0 and Fe^{2+} valence states (Keller and Clemett 2001). Diffusion of O from the surrounding silicate glass to the nanoparticle can oxidize metallic Fe to Fe^{2+} , in the form of FeO, as discussed above. However, this oxidation process may not be adequate in producing the Fe^{3+} observed in some nanoparticles because, if it were, abundant Fe^{3+} should also be observed in the surrounding glass matrix from which the O is derived, which has not been reported. We explore below additional mechanisms for oxidizing ferrous to ferric iron.

In one such mechanism, we can consider the oxidation of Fe^{2+} to Fe^{3+} in the presence of hydrogen implanted into lunar soils by the solar wind. This hydrogen can bond with oxygen to produce water molecules that are shown to be concentrated in lunar agglutinitic glasses (Liu et al. 2012). High-resolution images of Fe nanoparticles collected from each of the soil samples indicate that the oxidized Fe in the submature and mature soils is present in the form of Fe-oxide minerals, not simply as Fe ions. Thus, a possible alternative pathway toward forming Fe^{3+} is through an Fe-oxide nanoparticle reaction with water that is concentrated in the glass matrix. The oxidation of Fe^{2+} in wüstite can produce Fe^{3+} in magnetite via:



This is a plausible reaction that may occur in lunar soils as this work identified FeO and Fe_3O_4 phases within the nanoparticles, and H_2O and H are known to be components of lunar soils and agglutinitic glasses (Liu et al. 2012).

If this reaction were occurring at equilibrium it would be possible to constrain an equilibrium constant for the reaction that would be dependent upon the activity of H_2O and the fugacity of H_2 :

$$(4.7) \quad k_{eq} = \frac{a_{\text{Fe}_3\text{O}_4} f_{\text{H}_2}^{0.83}}{a_{\text{FeO}}^{3.17} a_{\text{H}_2\text{O}}^{0.83}}$$

where a is the activity of the solid and f is the fugacity of the gas. Assuming the Fe_3O_4 and FeO components are pure substances with activities of 1, the equilibrium constant becomes dependent upon the H_2 fugacity and the H_2O activity.

However, constraining the conditions of reaction 4.6, and by extension equation 4.7, is challenging. This reaction could be driven by episodic heating events, e.g., from an adjacent micrometeorite impact. In this case, the oxidation reaction is likely kinetic in nature, and equilibrium predictions are inapplicable. Further, the thermodynamic properties of agglutinitic glasses, in which such oxidation is occurring, are unknown. Specifically, the H_2 and H_2O components are present in the matrix (Liu et al 2012), suggesting that the thermodynamic activity of these molecules associated with their chemical siting is important, though unknown. As a result it is not possible at this time to provide an accurately quantified temperature constraint for the proposed reaction. Future efforts at quantitatively treating this problem may require detailed experimental work, theoretical modeling, or some combination of these.

4.4.2 Reflectance Modeling

Varying the Fe oxidation state of lunar soils significantly alters their optical properties and reflectance spectra. In particular, the addition of Fe^{3+} into npFe compositions in proportions that we measured through EELS causes noticeable reddening

and brightening of the reflectance spectra. The slope of the modeled soil containing Fe^{3+} is over 50% higher (redder) than the measured soil. Thus, the degree of absorption-band attenuation and the effects that npFe particles have on the reflectance spectra of weathered materials should be reevaluated. Based on our measurements and model results, it is not appropriate to simulate space weathering effects on the Moon using pure Fe^0 nanoparticles. A variety of oxidation states, with proportions relevant to the maturity of the sample, should be considered in order to preclude under and/or over estimating the npFe concentration generating weathering characteristics. This is in contrast with recent analyses of samples from near-Earth asteroid (25143) Itokawa. Solar-flare track identification and analysis suggest that this asteroid's surface may be very immature compared to the lunar surface (Keller and Berger 2014). Thus, for some asteroids it may be more appropriate to create reflectance models of asteroidal surfaces with a singular Fe oxidation state, Fe^0 .

Understanding the effects that different Fe oxidation states have on the characteristics of reflectance spectra could contribute to a deeper understanding of the distribution of soil maturities from remote sensing data on airless bodies such as the Moon. Analyzing the reflectance spectra for different regions of the Moon and comparing them to simulated spectra with reduced and oxidized Fe nanoparticle contributions may allow us to determine remotely the relative maturities of sample regions. This insight could

contribute to our understanding of regolith processing and landscape evolution on the surface of the Moon and other airless bodies.

4.5 Conclusions

EELS measurements of nanophase Fe in space-weathered lunar soils of varying maturities show that the Fe in the nanoparticles occurs in Fe^0 , Fe^{2+} , and Fe^{3+} oxidation states. The EELS measurements are corroborated through phase identification via high-resolution imaging. Immature soils primarily contain reduced, metallic Fe^0 nanoparticles, submature soils contain Fe^0 and Fe^{2+} , and mature soils contain Fe^{2+} and Fe^{3+} . In the submature sample we found npFe with oxidized shells. We hypothesize that the oxidation of npFe is a result of the diffusion of O atoms through the surrounding glassy matrix to the nanoparticle surface over time. We show that there is a significant difference in the reflective properties of lunar soil when including npFe particles with a range of oxidation states. Future efforts to simulate space weathering may need to consider oxidized Fe when modeling the spectral reflectance of the surface of an airless body. A spectral model that more accurately accounts for the micro-scale chemical complexity of the surface could be used to understand the macro-scale chemical and physical evolution of airless body landscapes from remote sensing data.

4.6 Acknowledgements

We thank CAPTEM for allocation of lunar samples for this study. We gratefully acknowledge the use of facilities within the Leroy Eyring Center for Solid State Science at Arizona State University, with assistance from Dr. Toshihiro Aoki. We thank Dante Laurretta for providing helpful advice on the manuscript. We also acknowledge the use of Electron Beam Analysis Labs at the NASA Johnson Space Center. Funding for M.S. Thompson is provided by the Natural Sciences and Engineering Research Council of Canada (NSERC) and the NASA Earth and Space Science Fellowship (NESSF). Research supported in part by NASA.

CHAPTER 5
IN SITU EXPERIMENTAL FORMATION AND GROWTH OF NpFe
PARTICLES AND VESICLES IN LUNAR SOIL

Abstract

Here we report results of the first dynamic, in situ heating of lunar soils to simulate micrometeorite impacts on the lunar surface. We performed slow- and rapid-heating experiments inside the transmission electron microscope to understand the chemical and microstructural changes in surface soils resulting from space weathering processes. Our slow-heating experiments show the formation of Fe nanoparticle begins at ~575 °C. These nanoparticles also form as a result of rapid heating experiments, and electron energy-loss spectroscopy measurements indicate the npFe particles are composed entirely of Fe⁰, suggesting this simulation accurately mimics space weathering processes occurring on airless body surfaces. In addition to npFe grains, rapid-heating experiments also formed vesiculated textures in the samples. Several grains were subjected to repeated thermal shocks, and the measured size distribution of number of npFe particles evolved with each subsequent heating event. These results provide insight into the formation and growth mechanisms for npFe grains in space weathered soils and could provide a new methodology for relative age dating of individual soil grains from within a sample population.

5.1 Introduction

Surface soils on airless bodies such as the Moon and asteroids experience irradiation from solar energetic particles and micrometeorite impact events (Hapke 2001). Such space weathering alters the chemical and microstructural characteristics of surface grains and thus, their optical properties, attenuating characteristic absorption bands, and reddening and darkening soil reflectance spectra (Hapke 2001). Investigating the nature of space weathering products is important for understanding the evolution of airless body surfaces, and how weathering processes affect reflectance spectra obtained from remote sensing spacecraft.

Space-weathering features were identified in returned samples from the Moon and near-Earth asteroid Itokawa and include: glassy agglutinate grains, partial and completely amorphous rims on grains, vesiculated grain textures, and nanophase Fe particles, e.g., (Keller and McKay 1993, 1997; Noble et al. 2005; Noble et al. 2011; Noguchi et al. 2014; Noguchi et al. 2011; Thompson et al. 2014). Fe nanoparticles (npFe) contribute to the changes we observe in the optical properties of space-weathered material (Hapke 2001), and several mechanisms have been proposed for their formation. One such process suggests that hydrogen implanted by solar-wind irradiation functions as a reducing agent in surface soils during a melting or vaporization event e.g., a micrometeorite impact event (Hapke 2001). Another proposed mechanism includes sputtering and re-deposition of material during ion-irradiation events, i.e., if O atoms are preferentially sputtered from the surface of a grain, a localized reducing environment is created and Fe in the residual material becomes reduced (Hapke 2001). A third mechanism proposes that oxide molecules are vaporized in the target material during an impact event, the FeO molecules dissociate, the

volatile oxygen dissipates, and the Fe atoms condense as nanoparticles (Keller et al. 1998). These formation pathways indicate that npFe develops as a result of both micrometeorite impacts and ion-irradiation processes.

Investigating the microstructural, chemical, and optical properties of npFe particles is a critical part of understanding the nature of space weathering processes. Surface soils with a higher maturity, i.e., amount of exposure time to interplanetary space, have a larger concentration of npFe particles. Recent work has shown these nanoparticles can oxidize from metallic (Fe^0) to ferrous (Fe^{2+}) and even ferric (Fe^{3+}) Fe on the lunar surface after their formation, and that oxidized Fe impacts the optical properties of the soil in which the npFe is hosted (Thompson and Zega 2015; Thompson et al. 2016). An investigation of the effect that npFe size has on resulting reflectance spectra showed that small (<10 nm) nanoparticles are responsible for reddening the reflectance spectra of soils, whereas larger (>50 nm) particles cause darkening of the overall spectrum (Keller et al. 1998).

In addition to npFe particles, recent analyses of soil returned from asteroid Itokawa by the Hayabusa mission revealed the presence of vesiculated textures in space-weathered grains. The vesicles are visible on the surfaces of soil grains as seen in secondary electron (SE) imaging, and in the outer 50 nm of the grains when viewed in cross section in the transmission electron microscope (TEM) (Matsumoto et al. 2015a; Noguchi et al. 2014; Noguchi et al. 2011; Thompson et al. 2014). These vesicles are hypothesized to have formed by solar wind irradiation of grains on airless body surfaces. However, vesicles are relatively rare in mature lunar soils, which have experienced high doses of ion irradiation, suggesting this may not be the sole mechanism responsible for vesicle formation. It is

possible that a heating event, such as a micrometeorite impact in the adjacent soil, could be contributing to the development of vesiculated textures.

In order to understand the nature of the airless body surface conditions that are generating these features, several experimental techniques have been developed to simulate space-weathering processes. Solar wind bombardment has been simulated through ion irradiation of planetary surface analog materials with H, He, Ar, and Ga ions. These irradiation experiments have been performed under a wide range of energies and vacuum levels, with some experiments closely mimicking solar-wind energies, e.g., 1 keV H⁺ and/or 4 keV He⁺, and ultra-high vacuum conditions (Christoffersen et al. 2012; Dukes et al. 1999; Keller et al. 2015; Loeffler et al. 2009). The total fluence that the experimental analog samples experience simulates millions to hundreds-of-millions of years on the surface of an airless body, within a laboratory timescale. These experiments are typically performed with the goal of understanding the changes in spectral properties that occur as a result of irradiation, and so the reflectance spectra are measured from the samples before and after experimentation, either in situ or with an ex situ spectrometer. Beyond changes in the optical characteristics, several studies have used TEM to investigate changes in the chemistry and microstructure of these samples resulting from simulated space-weathering conditions. These studies have shown the presence of amorphous microstructures, Fe nanoparticles, and vesiculated textures near the irradiated surface in the post-irradiation samples, e.g., Christoffersen et al. (2012), Keller et al. (2015).

In addition to ion irradiation studies, micrometeorite impact events have been simulated in surface analog materials. Using pulse-laser irradiation, the sample is repeatedly exposed to nano-second laser pulses, e.g., timescales similar to impact events,

under high vacuum, e.g., (Christoffersen et al. 2016; Gillis-Davis et al. 2015; Matsuoka et al. 2015; Sasaki et al. 2001). The energy imparted by the laser can then be compared to that of a micrometeorite impact event, assuming an impactor size and velocity. This technique has been successful in reproducing the optical changes observed in naturally weathered materials, and some experiments have shown the presence of Fe nanoparticles with similar size and concentration to those observed in the returned samples, e.g., Sasaki et al. (2001). These experiments produced similar effects on the optical properties of surface soils to those resulting from natural space weathering processes, but they do not consistently produce microstructural and chemical characteristics similar to those observed in returned samples e.g., Christoffersen et al. (2016). Ion irradiation experiments are using a methodology to simulate solar wind bombardment that is nearly identical from a microphysical perspective to what is occurring on airless body surfaces. Pulse-laser irradiation simulates an impact event by mimicking the estimated total energy introduced into the system during an impact event, which may not replicate the physical mechanisms creating space weathering features in these samples, or account for the chemistry of the impactor. These experiments are able to reproduce spectral properties of space-weathered samples without necessarily creating the same chemical and microstructural features that result from actual space weathering conditions. While these experiments have provided important insight into our understanding of space-weathering processes, we are unable to observe changes in chemistry and microstructure *during* the simulated weathering event. None of the described procedures allows for the observer to witness the formation or continued growth of npFe particles or vesicles in real-time.

Here we use a new technique to simulate space-weathering conditions in situ inside the TEM using a specialized heating stage. We perform slow- and rapid-heating experiments on mature lunar soils to simulate temperature changes and energy input similar to micrometeorite impact events occurring on the surfaces of airless bodies. These experiments allow for the observation of npFe formation and ripening, and the development of vesiculated textures in lunar soil grains. This work presents the first direct in situ observation of surface soils being subjected to simulated space weathering conditions, providing insight into the nature of these processes and the resultant microstructural and chemical features. The results presented here provide a new perspective on space weathering of returned samples, and provide a relevant methodology for simulating surface processes relevant to the upcoming OSIRIS-REx and Hayabusa II missions.

5.2 Methods

For these experiments, a mature lunar soil was chosen in order to obtain grains for analysis that have a high concentration of implanted H and He, which may contribute to the production of vesicles and/or npFe particles during in situ heating. Grains of mature mare lunar soil 79221 were suspended in methanol and agitated. We allowed the grains to settle for ~30 seconds, based on a Stoke's law settling calculation, to enable the largest size fraction of grains to drop out of suspension to the bottom of the vial. We extracted the finest-size fraction from the suspension in order to analyze grains that contain localized electron-transparent regions. Using a micropipette, we drop-cast the suspension onto either C-coated Ni grids or SiN thermal e-chips for analysis in the TEM, depending on the heating

methodology we employed. We deposited several droplets on each TEM grid to ensure a high enough density of grains for analysis in the experiments.

We used two distinct methodologies for simulating micrometeorite impacts. In the first method, we heated samples incrementally on the carbon-coated Ni grids using a Gatan slow-heating stage inside the 300 keV monochromated and aberration-corrected FEI Titan environmental TEM (ETEM) at Arizona State University (ASU). The Titan ETEM is equipped with bright-field (BF) and dark-field (DF) STEM detectors. We heated the grains from room temperature to ~1000 °C over the course of 15 minutes. We chose this temperature to ensure that implanted H and He would become mobilized within the sample, increasing the likelihood of observing the formation of space-weathering features like npFe particles or vesicles (Cintala 1992; Gibson Jr and Johnson 1971). We collected BF images of the material at roughly 150 °C increments over the course of the experiment. We also performed energy-dispersive x-ray spectroscopy (EDS) mapping of the samples before and after heating. EDS mapping was performed on the JEOL 2010F TEM at ASU, equipped with a dark-field (DF) STEM detector and an EDAX thin-window Si(Li) EDS system.

In the second method, we thermally shocked samples on specialized Hitachi SiN chips to ~1000 °C and back to room temperature in <1 second inside the 300 keV Hitachi HF3300 TEM at the University of Toronto. The HF3300 is equipped with BF, DF and secondary electron (SE) detectors, a Bruker silicon-drift EDS detector, and a Gatan GIF Quantum electron energy-loss spectrometer (EELS). We recorded video of the heating experiments, and collected BF, high-angle annular dark-field (HAADF), and SE images, as well as EDS maps of the grains before and after heating. We also collected EELS spectra of several Fe nanoparticles that formed during heating. Spectra were acquired from

individual nanoparticles with a collection semi-angle of 35 mrad, a dispersion of 0.25 eV/channel, a 0.21 nm probe size, and dwell times between 1.0 to 2.0 s/px. We measured npFe particles that were sitting in relief from the surface of the lunar soil grain in which they were embedded. A line profile was collected across each nanoparticle extending into the glassy matrix. A spectrum was extracted from the region of each particle that was not embedded in the glassy matrix, which limited thickness effects and contributions of matrix Fe to the spectrum. We removed the background from each spectrum, in the form of AE^{-1} , and deconvolved the ZLP using the Fourier-Ratio method (Egerton 1996). The continuum intensity has been successfully modeled with linear and step-function (arctan) fits between edge onset and post-edge energies (Garvie and Buseck 1998; van Aken et al. 1998). As such, we used a linear fit between 705 to 735 eV to subtract the continuum beneath the Fe $L_{2,3}$ edge for each spectrum e.g., Thompson et al. (2016), Zega et al. (2003) .

We performed a flux-weighted, linear, least-squares fit between the observed EELS spectra and three standards, in order to determine the Fe oxidation state of nanoparticles, as described in Thompson et al. (2016). The standard spectra were measured using the same operating conditions as described above and include: Fe^0 (Fe metal; 99.98% purity), Fe^{2+} (FeO, wüstite; 99.9% purity), and Fe^{3+} (Fe_2O_3 , hematite; 99.9% purity). The Fe-oxidation-state ratios were quantified using the $L_{2,3}$ edge which exhibits edge-onset and multiplet peak structure that is indicative of oxidation state, e.g., Garvie et al. (1994). We evaluated goodness of fit using the coefficient of determination, R^2 , where values of R closer to 1 imply better fits to the observed spectrum. Spectra with an R^2 value of >0.9 were accepted as having a reasonable fit.

In addition to single-shock experiments, we subjected some samples to multiple heating events. We repeatedly thermally shocked selected samples to ~ 1000 °C in <1 second; one sample was shocked eight times and another sample was shocked 12 times in total. We recorded video throughout each heating interval, and imaged and collected EDS maps of the grains after the final thermal event. Between the first and final thermal shocks, we measured the minimum and maximum sizes of npFe particles that formed on the grain surfaces along their longest axis. We also measured the total number of nanoparticles visible on the surfaces of the grains in SE images, and an overall size distribution for the nanoparticles between the initial and last heating events. We used SE images for this analysis because the thickness of the sample made it difficult to determine whether contrast changes in the HAADF images were due solely to the presence of a high-Z (Fe) nanoparticle. Also, the HAADF and BF STEM images represent the entire cross section of the grain, making it difficult to count individual nanoparticles accurately as the npFe grains may appear to be superimposed on one another when present in high concentrations in the grain interior. As such, while we provide the total number of nanoparticles visible on the grain surfaces, differences in nanoparticle populations may be better reflected in the measured size distributions.

5.3 Results

We monitored individual grains throughout each experiment, during both slow- and rapid-heating events. For each run, we continuously observed and recorded the thermal episode for one grain within the field of view. The results of multiple experimental runs

are discussed here. For many of the slow heating experiments, we also imaged several individual grains both before and after the heating event.

5.3.1 Slow-heating Experiments

We monitored grains for visible changes in microstructure, and we highlight one grain ‘79221-S1’ here. 79221-S1 has a pyroxene-like composition and measures 1.5 x 1.5 μm in size. Prior to heating, the grain had localized npFe grains, measuring between 5 and 48 nm in diameter (Fig. 5.1). Between room temperature and 544 °C, we did not observe any changes within the grain. Between the temperature steps of 544 and 575 °C, we observed formation of new npFe in the host grain, in the region that previously did not exhibit any nanoparticles (Fig. 5.1b). The nanoparticles that occurred prior to heating also began to increase in size during this temperature interval. As the grain was heated to a maximum temperature of 900 °C, the npFe particles continued to form and grow larger in size, up to 65 nm in diameter (Fig. 5.1d). Some of the npFe are euhedral while others are spherical in shape (Fig. 5.2a).

Nanoparticles were observed to develop in another grain that was heated in a similar manner, 79221-S2, with their initial formation occurring during the same temperature range. Post-heating EDS mapping of this grain revealed that the nanoparticles are composed of Fe (Fig. 5.2c). No other elements are associated with Fe in the nanoparticles (cf., Fig. 5.1d-h).

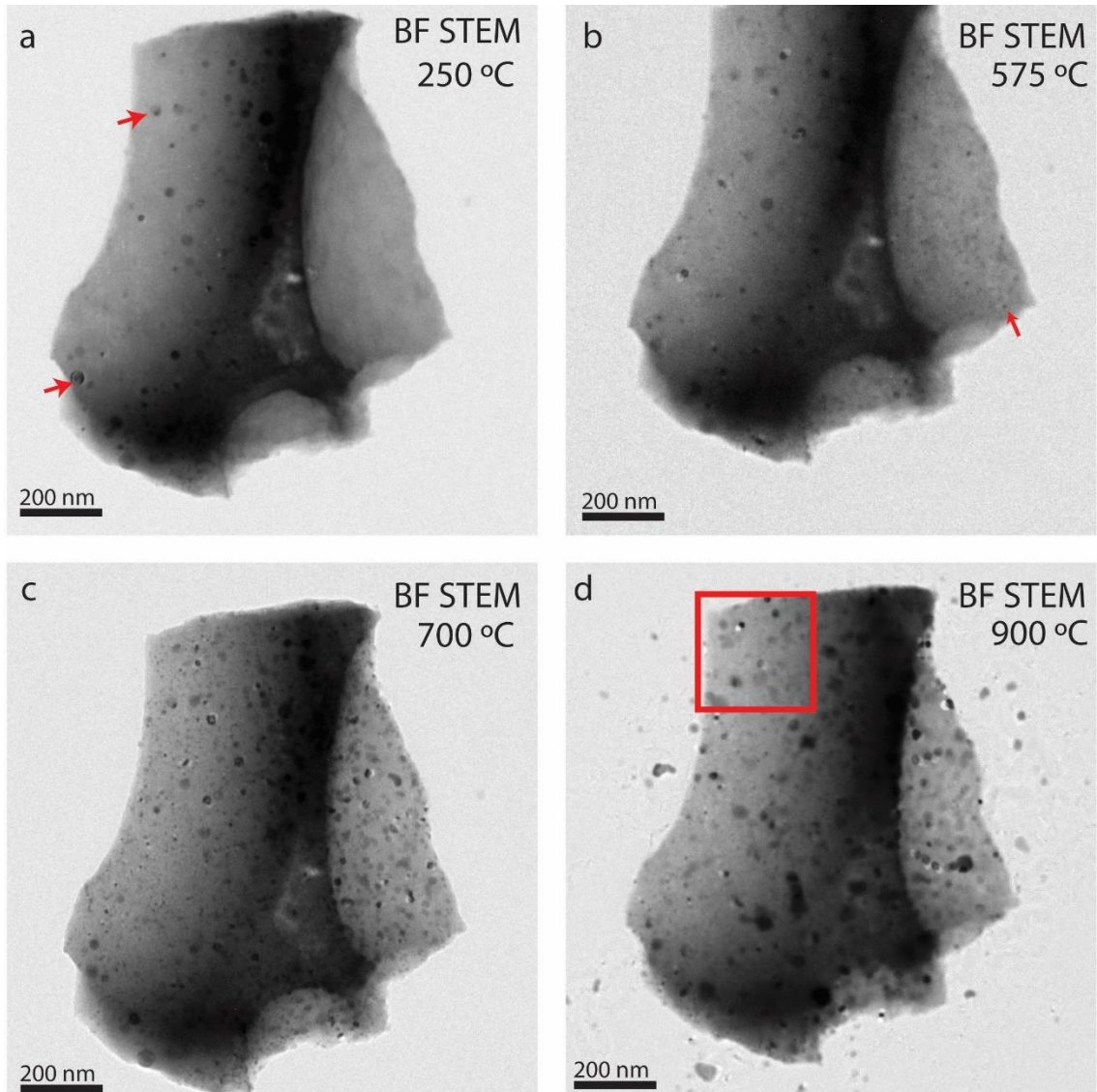


Figure 5.1: Slow heating experiments of a grain with areas containing localized npFe particles prior to heating (left hand side of the grain, indicated by red arrows). BF STEM images of the monitored grain at (A) 250 °C, (B) 575 °C where the red arrow indicates a newly formed nanoparticle, (C) 700 °C, and (D) 900 °C, the final temperature step.

5.3.2 Single Thermal-shock Experiments

During rapid heating, several distinct changes were observed in the grains. The morphology of the grains changed as a result of heating, angular grains became highly rounded and spherical, and features sitting in sharp relief on the surface of the grains,

79221-R1 and -R2 became less defined and more continuous with the underlying material, as seen in SE imaging of grains 79221-R1 and 79221-R2 (Fig. 5.2c,f). The grains

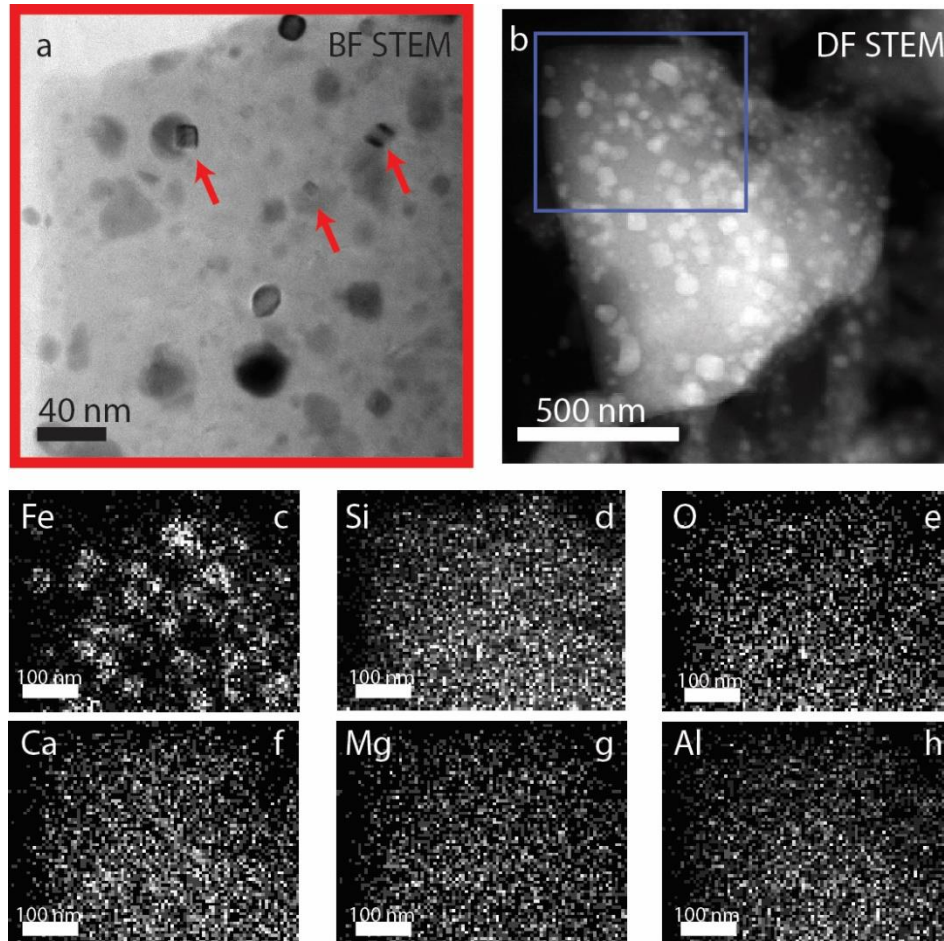


Figure 5.2: TEM data of grains that underwent slow-heating (A) TEM images of the npFe particles where red arrows indicate euhedral grains, (B) DF STEM image of a slowly heated grain. EDS maps of the region outlined by the blue box in (B) showing (C) Fe, composing the nanoparticles, and uniform distributions of Si, O, Ca, Mg, and Al (D-H, respectively).

monitored during these experiments exhibited little to no npFe particles prior to heating, but we observed the rapid formation of high densities of nanoparticles during the thermal shock (Fig. 5.3). SE imaging of the grain revealed that nanoparticles formed on the surface of the grain (Fig. 5.3f). HAADF imaging shows that additional nanoparticles are formed

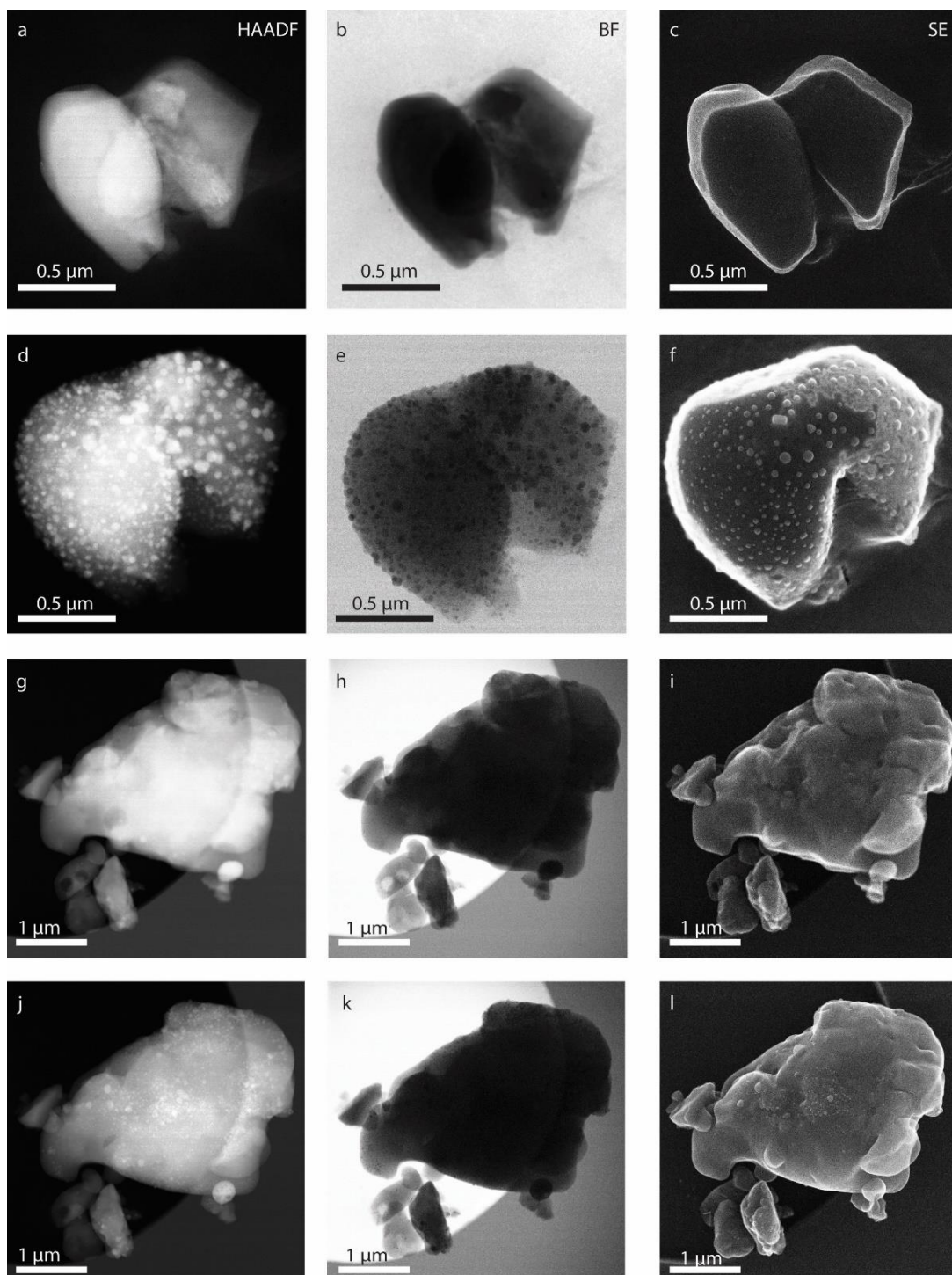


Figure 5.3: TEM images from two grains that underwent single-thermal shocks. Grain 1, 79221-R1, is shown pre- and post-heating, respectively, in (A,D) HAADF, (B,E) BF, and (C,F) SE. Note the development of nanoparticles visible in each of the post-heating images, with a substantial proportion visible on the grain surface in SE. Grain 2, 79221-R2 is shown pre- and post-heating, respectively, in (G,J) HAADF, (H,K) BF, and (I,L) SE. Note that fewer nanoparticles are visible on the grain surface in SE, but many are in the grain interior as visible in HAADF and BF.

interior of the grains, in varying proportions. The nanoparticles exhibit both spherical and euhedral shapes. EDS maps collected after heating indicate the nanoparticles are composed of Fe, and the distribution of all other elements appear uniform across the grain (Fig. 5.4).

We also observed the formation of vesicles in the exterior rim of one of the grains. SE imaging shows a hummocky texture on the grain surface of 79221-R2, which corresponds to elliptical features that exhibit low contrast in HAADF images and high contrast in BF images (Fig. 5.5). The vesicles are between 10 to 25 nm in their longest diameter, and are consistent in size and shape to those reported in other lunar soils and samples from Itokawa.

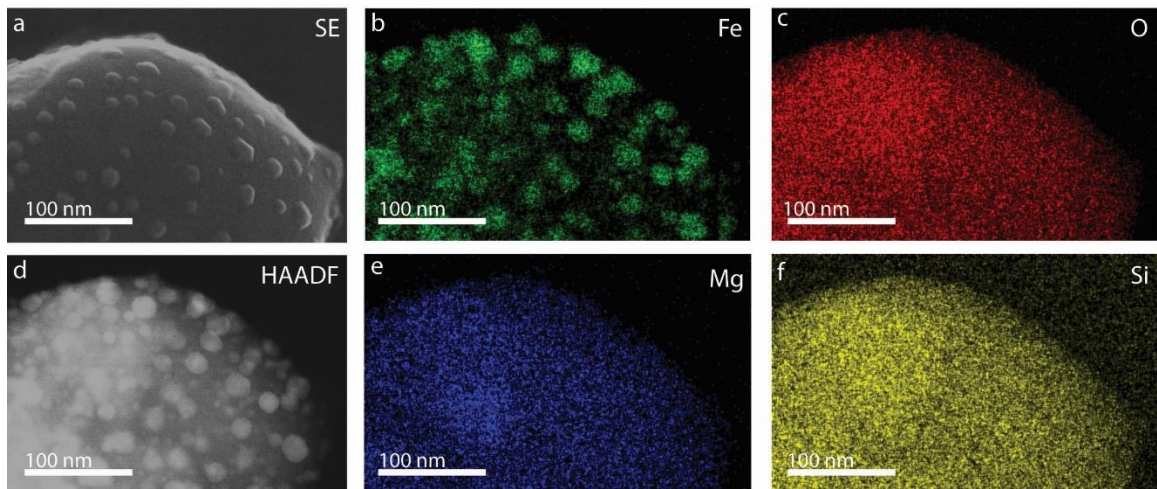


Figure 5.4: TEM images of nanoparticles, visible post-heating in (A,D) SE and HAADF imaging. EDS maps show the composition of the nanoparticles is Fe in (B), and that the distribution of other constituent elements is uniform in (C) O, (E) Mg, and (F) Si.

5.3.3 Multiple Thermal-shock Experiments

79221-R1 and -R2 were each subjected to multiple thermal shocks of the same duration (<1 s) as their initial heating cycle. 79221-R1 was thermally shocked eight times, whereas 79221-R2 was shocked a total of 12 times. For both grains, the average size of the

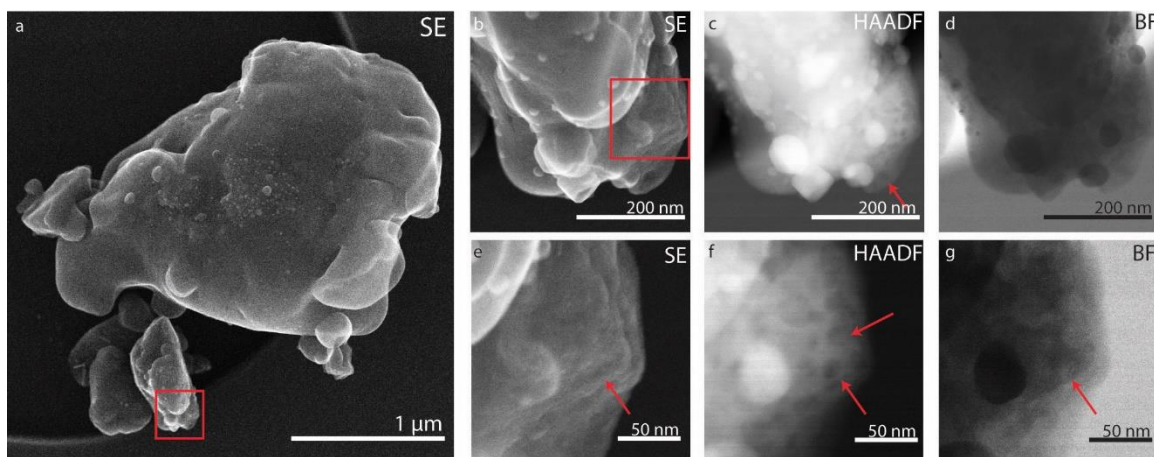


Figure 5.5: TEM images of 79221-R2, subjected to rapid-heating, shown in (A) SE. High magnification images of the area indicated by the red box in (A) are shown in (B) SE, (C) HAADF, and (D) BF. The area outlined by the red box in (B) shows (E) SE image of a hummocky texture on the surface of the grain, indicated by the arrow, (F) Low contrast elliptical shapes in HAADF, vesicles, indicated by red arrows, also shown as high contrast ellipses in (G) BF.

npFe particles increased with each subsequent heating (Fig. 5.6). Nanoparticles in the grain that was shocked 8 times increased in average diameter from 17.8 nm (single thermal shock) to 28.2 nm over the course of the experiment. In the case of the grain shocked 12 times, the npFe particles increased from 18.5 nm to 45.1 nm after all the thermal episodes. The size distribution of the nanoparticles also changed significantly over the course of multiple heating events. After one heating event, a histogram of the npFe particle sizes is right-skewed for both grains (Fig. 5.7a,c). After multiple heating events, the npFe populations exhibit a Gaussian-like distribution of npFe sizes, although the 8-shocked sample peaks at a smaller size relative to the 12-shocked sample (Fig. 5.7b,d). While one of the grains exhibited an increase in the average size of its' nanoparticles, the total number of npFe grains counted on the surface of the grain decreased overall. The maximum size of npFe particles increased between the first thermal event and the final thermal event for both grains.

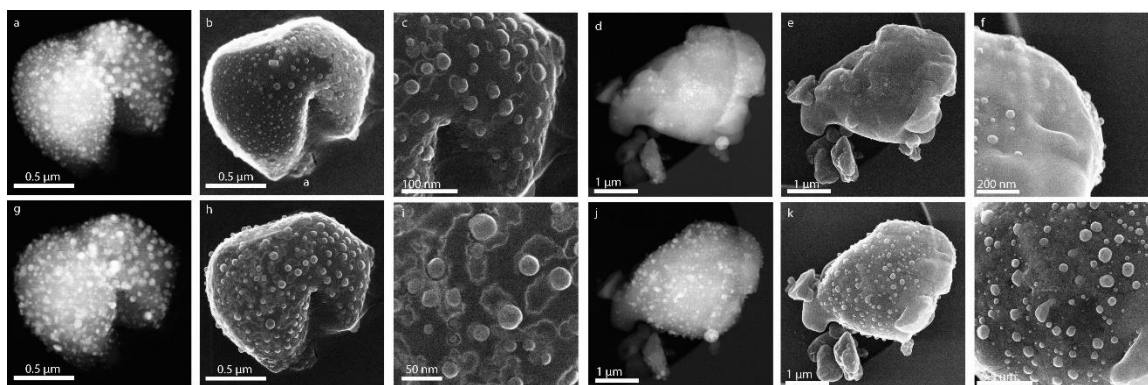


Figure 5.6: TEM images showing 79221-R1 subjected to multiple thermal episodes is shown after one event, as seen previously in Figure 5.2, and multiple (eight total) events, respectively in (A,G) HAADF, (B,H) SE. High magnification images of nanoparticles after multiple heating events shown in (C,I). Note the pitting visible on the surfaces surrounding the npFe particles. Another grain, 79221-R2 subjected to multiple heating events (12 total) is shown after one event, and multiple events, respectively in (D,J) HAADF, and (E,K) SE. Note the increase in nanoparticles visible on the surface in SE between the first and final thermal events. High magnification SE images shows (F) npFe particles just below the smooth surface of the grain, and (L) large nanoparticle sizes on the grain surface.

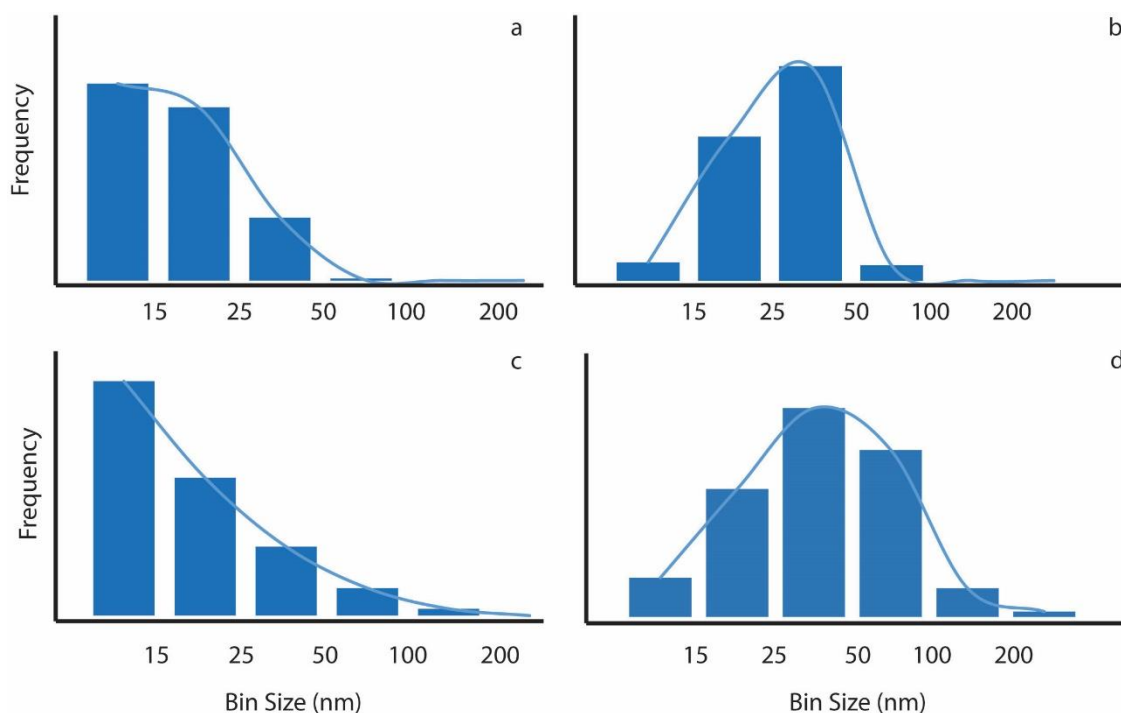


Figure 5.7: Particle size distributions for npFe in grains 79221-R1 and -R2 after (A,C) One thermal event, notice the right-skewed shape of the distribution, and (B) after 8 thermal events, (D) after 12 thermal events, each showing a more normal distribution.

5.3.4 EELS Measurements of NpFe Particles

We measured the EELS spectra of 6 individual npFe particles via line scans over an energy range that contained the N *K*, the Fe *L*_{2,3} and the O *K* edges. An example npFe grain is shown in Fig. 5.8. The spectrum extracted from the portion of the linescan that was acquired over the substrate only exhibits a N *K* peak, corresponding to the SiN heating chip material (Fig. 5.8c). The spectrum from the region of the linescan transecting only the particle contains both N *K* and Fe *L*_{2,3} edges, which are respectively attributed to the underlying SiN substrate and the nanoparticle (Fig. 5.8d). In comparison, the spectrum extracted from the nanoparticle embedded in the matrix contains N *K*, O *K*, and Fe *L*_{2,3} edges. These edges respectively correspond to contributions from the substrate, the glassy matrix, and the nanoparticle (Fig. 5.8e). The distribution of these elements as indicated by the EELS line profile are confirmed with EDS mapping of the npFe (Fig. 5.8f-i). Fe correlates with high-Z nanoparticles in the HAADF image, O appears in the matrix, and an overlay map of Fe and O together shows no appreciable oxygen in regions of the nanoparticles that protrude from the surface of the grain matrix, indicating the nanoparticles are composed of only Fe, and not an Fe-oxide mineral.

The oxidation state of Fe in the nanoparticles was determined by analyzing the structure of the Fe *L*_{2,3} edge. Our results indicate that all six nanoparticles analyzed are composed of 100% Fe⁰, with no contributions from other Fe oxidation states. An example nanoparticle spectrum and its associated best fit are shown in Fig. 5.9. Typical error on these quantification are <3 %, and the R² value for each fit was >0.9.

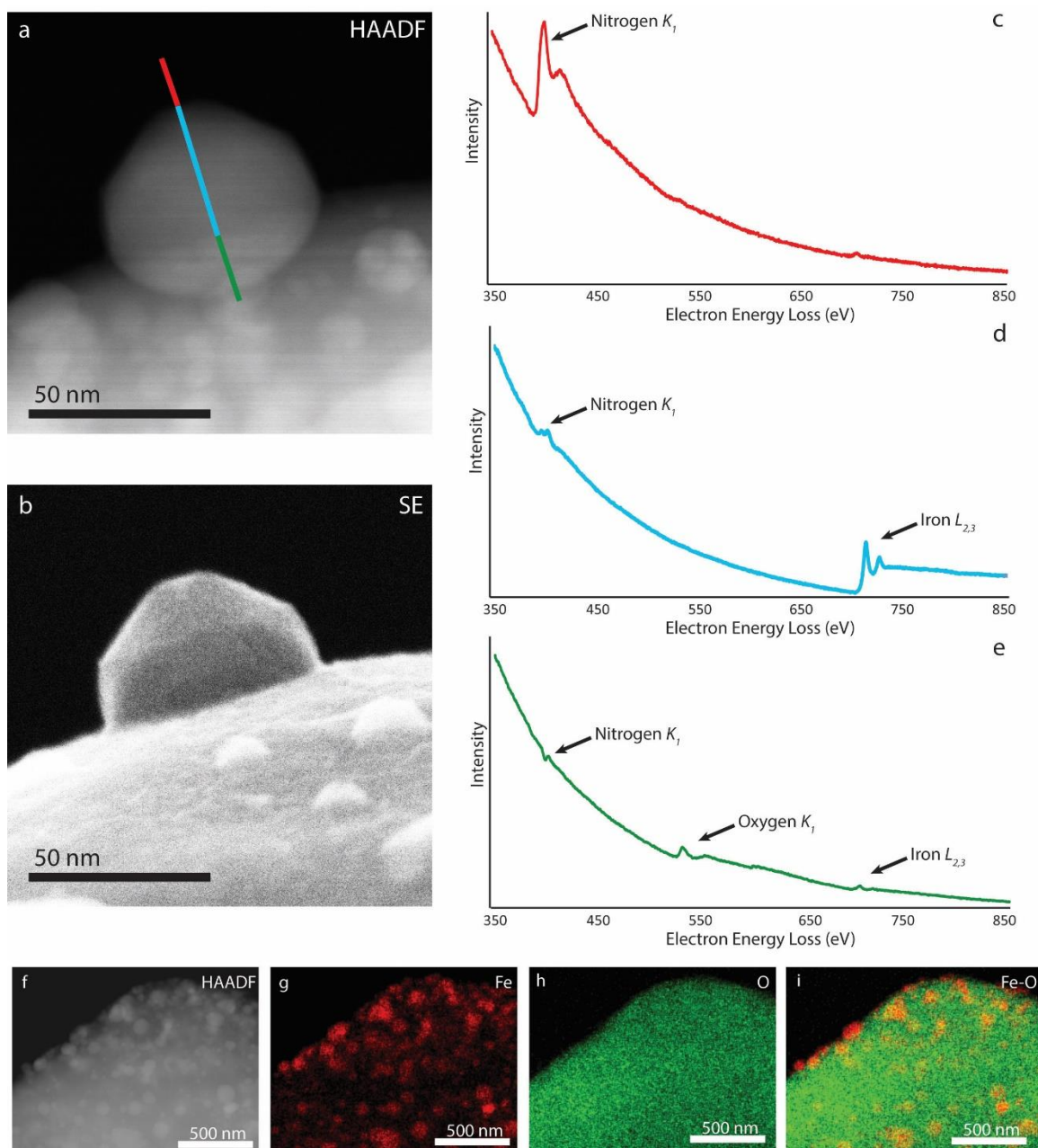


Figure 5.8: TEM images of individual nanoparticles shown in (A) HAADF, and (B) SE, were analyzed using EELS via line profiles, shown in (A). EELS spectra extracted from (C) The red portion of the line in (A), shows the Nitrogen K_1 peak, (D) The blue portion of the line in (A), shows the Nitrogen K_1 peak and the Fe $L_{2,3}$ peak, and (E) The green portion of the line in (A), shows the Nitrogen K_1 , and Oxygen K_1 and the Fe $L_{2,3}$ peaks. EDS maps of the nanoparticles from the area of the grain where EELS spectra were collected, shown in (F) HAADF, show (G) Fe, and (H) O, which when overlaid in (I) indicate the nanoparticles are composed of Fe and the O remains in the surrounding matrix material.

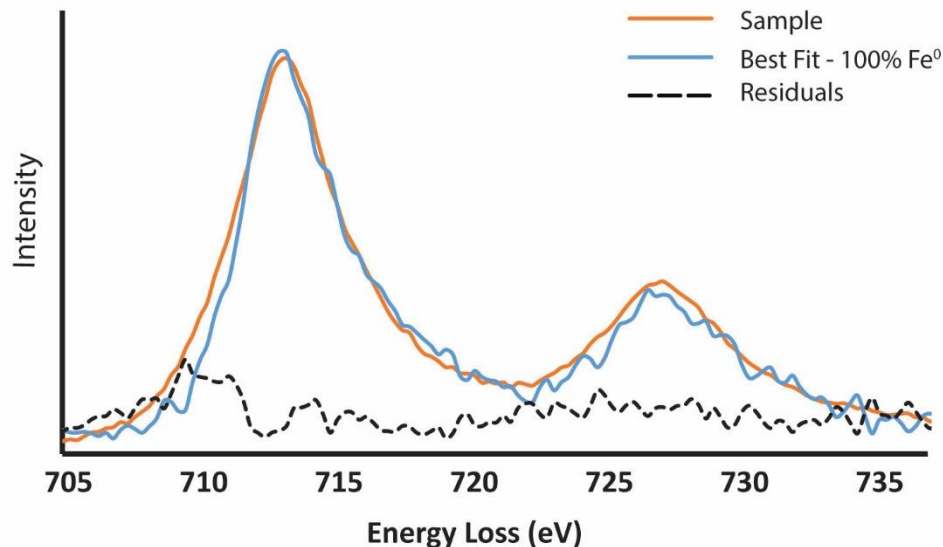


Figure 5.9: An EELS spectrum from an individual nanoparticle is shown in the orange line. The simulated best fit is shown in blue, and the residuals are shown by the black dashed line. This nanoparticle is composed of 100% Fe⁰ and the simulated fit has an R² value of 0.97.

5.4 Discussion

Both the slow- and rapid-heating simulations conducted herein produced several features that are consistent with microstructural and chemical characteristics we have observed in returned samples from the surfaces of airless bodies. Slow-heating and thermal-shock experiments produced npFe particles throughout the host grain that are similar in size, shape, and distribution as the nanoparticles found in agglutinates in lunar soils, indicating this novel experimental technique accurately mimics the natural space weathering processes (Hapke 2001). To our knowledge, this is the first direct observation of the formation of npFe particles in situ through experimental techniques.

The morphology on npFe particles provides insight into their formation and evolution. The euhedral nature of some nanoparticles has been recognized in immature lunar soil grains (Thompson et al. 2016). In the multiple thermal-shock experiments for

this work, the euhedral nanoparticles that developed after the initial heating event become more rounded/spherical with each subsequent thermal episode. A similar trend has been identified in lunar soils, as npFe in mature soils, which have had longer exposure times on the lunar surface and as such have experienced more space weathering events/processing, are almost entirely spherical (Thompson et al. 2016).

Nanoparticles formed in natural space-weathering processes have specific oxidation states. The measured oxidation state of npFe grains developed during these experiments, Fe^0 , is identical to returned lunar samples that have experienced recent space weathering activity (Thompson et al. 2016). Recent analyses of npFe grains in immature, submature, and mature soils show that npFe in immature soils is composed almost entirely of reduced Fe^0 . EELS measurements of the npFe in sub-mature and mature lunar soils suggest that it can oxidize over long timescales on the lunar surface, eventually including Fe^{2+} and Fe^{3+} components (Thompson et al. 2016). However, the initial formation of this npFe is in the reduced, metallic state, suggesting that the npFe particles developed here are similar to naturally produced nanoparticles.

The heating experiments also developed vesicles in the rims of the lunar soil grains. These vesicles have a similar size, shape, and distribution within the sample, as those identified recently in the samples from Itokawa, which were produced by space weathering processes (Matsumoto et al. 2015a; Noguchi et al. 2014; Noguchi et al. 2011; Thompson et al. 2014). Each of these chemical and microstructural features closely mimic what we observe in naturally space-weathered samples, indicating that using thermal shocks to simulate micrometeorite impacts is a novel and worthwhile approach to exploring the effects of these processes in the laboratory.

The formation mechanisms for space weathering characteristics have been discussed in the literature for decades. Features such as chemically heterogeneous grain rims have been attributed to both micrometeorite impacts and irradiation processes. In comparison, partial and complete amorphization are hypothesized to form as a result of solar wind irradiation alone. The experiments performed here provide the unique opportunity to further understand the formation of two primary space weathering features, npFe grains and vesicles.

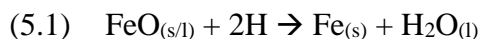
Vesiculated textures were recently reported in samples returned from the Hayabusa mission to asteroid Itokawa (Matsumoto et al. 2015a; Noguchi et al. 2014; Thompson et al. 2014; Noguchi et al. 2011). They are theorized to form through ion irradiation on the surfaces of airless bodies. However, mature lunar soils, which have experienced long exposure times to interplanetary space and thus a high degree of solar wind irradiation, do not often exhibit vesiculated textures, at least in the same frequency as has been observed in Itokawa particles. Experimental work simulating solar wind irradiation with 4 to 10 keV He^+ , which is a reasonable proxy for simulating the solar wind, has shown that vesicles form in analog materials at doses mimicking as little as 5,000 years on an asteroidal surface. These results suggest that ion irradiation may be a viable mechanism for vesicle formation (Matsumoto et al. 2015b). While the total dose the materials experienced is relevant to exposure timescales for grains on airless body surfaces it is important to also consider the flux of the ions used in these experiments. The flux of the solar wind is measured to be 1×10^7 ions/cm² at 1 AU for He^+ (Goldstein et al. 1996). Experiments are often performed with irradiation fluxes many order of magnitude higher than this, at 10^{12} - 10^{16} ion/cm² (Matsumoto et al. 2015b). Such a higher flux allows for the simulation of thousands or

millions of years of cumulative solar wind irradiation on laboratory timescales. However, experiments performed at low doses, which are more similar to the actual solar wind, have difficulty in generating well-formed vesicles of the size and shape described in returned samples (Matsumoto et al. 2015b). As such, these experiments suggest an unnaturally high irradiation flux would be needed to generate vesicles in surface samples on airless bodies. Surface soils with young exposure ages, like those from asteroid Itokawa, have experienced low doses of solar wind irradiation, and thus it is unclear how vesiculated textures would develop in these grains without another contributing formation mechanism (Keller et al. 2016).

While ion irradiation experiments had difficulty reproducing vesiculated textures, we observed the formation of vesicles in the experiments performed here. We hypothesize that heating events in the soil adjacent to the target grain, such as a micrometeorite impact, may contribute to the formation of these vesicles. We postulate that H^+ and He^+ that has been implanted in the target grain from the solar wind may rapidly de-gas from the matrix during one of these thermal shocks, and will coalesce to form vesicles that become part of the microstructure of the grain rim. Subsequent thermal shocks to this grain may change or erase the vesiculated structures developed after the initial heating event. As a result, vesicles may be preserved in surface grains that have only experienced a single, or very few heating events. This may be evidenced in grains on the surface of Itokawa which have had short exposure times and, consequently, may have experienced fewer heating events, allowing the vesiculated textures we observe in these soils to remain intact. In contrast, most lunar soil grains will have experienced longer space weathering timescales, meaning

the grains have likely been processed by heating events multiple times, which may disturb or erase the vesicles present in grain rims.

In addition to the vesicles, understanding the formation mechanism for npFe particles is important for developing a comprehensive model of space weathering processes. One potential pathway for npFe formation is that solar-wind implanted hydrogen (H^+) acts as a reducing agent for oxidized Fe (Fe^{2+}) in the surface soils (Hapke 2001). When these H-bearing grains experience melting and/or vaporization as a result of a subsequent micrometeorite impact, FeO and other oxide molecules, are liberated from the grain's crystal structure. The implanted hydrogen acts to reduce the Fe in the melt or vapor via the reaction:



We hypothesize that npFe particles are forming during the thermal shocks in this experiment via (5.1). We targeted the finest size fraction of grains within sample 79221, as small grains are likely among the most mature grains in an already mature soil, meaning they have a high probability of containing implanted H and He from the solar wind. The experiments were performed at vacuum, with pressure measurements inside the TEM column of 3.8×10^{-5} Pa throughout the heating cycles, and so there is very little atmospheric gas to interact with the sample during heating. The npFe particles that formed during these episodes were both in the grain interior and on the surface. If there was residual gas, such as H, inside the TEM column driving the reaction, as opposed to implanted solar wind H native to the grain, it would be unlikely that npFe particles were forming in the particle interior. Instead we would expect nanoparticles to form only on the surface, where the H would be in contact with the sample. In addition, the EELS measurements indicate the Fe

is metallic, without any contributions from other Fe oxidation states, suggesting the experimental environment had an oxygen fugacity low enough to drive the reduction of Fe from the ferrous state.

The slow-heating experiments performed here provide a temperature constraint for the initial formation of npFe particles. Previous work has shown that npFe grains appear to be stable and unchanged when heated up to 200 °C (Noble and Pieters 2003), but these experiments applied heat over the course of many hours with the intention of studying thermal cycling on airless body surfaces, not micrometeorite impact formation of npFe. The work presented here indicates that any Fe-bearing grain that experiences a rapid temperature change to 575 °C has the potential for developing npFe. This may prove relevant for predicting npFe formation on the surfaces of other airless bodies that experience more extreme thermal variations, such as Mercury.

Beyond a temperature constraint for formation, this work provides insight into the growth of npFe particles as a result of repeated heating episodes. The process known as Ostwald ripening has been proposed to explain the continued growth and development of npFe in surface soils experiencing thermal cycling on airless bodies (Noble and Pieters 2003). Ostwald ripening is thermodynamically driven, as larger particles are more energetically favourable than smaller ones, because molecules or atoms on the surface of a particle are more unstable than those in the interior of a grain (Ratke and Voorhees 2013). The boundaries between npFe particles and the surrounding matrix have an associated interfacial energy, and more interfaces (i.e., more small particles which have a high surface area/volume ratio) means higher overall energy. The system acts to minimize its energy, and as a result decreases the total amount of interfacial area, resulting in coarsening of

existing particles over time (Ratke and Voorhees 2013). Ostwald ripening also drives angular nanoparticles to become more spherical over time, because spheres are an energy-minimized structure. This process can be driven by diffusion of atoms from the matrix to the nanoparticle surface. As a result, the particle-size distribution changes over time, from a right-skewed population of small particles, to a normal distribution, and perhaps eventually a left-skewed population (Li et al. 2015). In a system that has reached equilibrium, meaning the number of nanoparticles of a specific composition are saturated with respect to the composition of the matrix, the total volume of the nanoparticles will remain constant. In this case, while the size of the nanoparticles are increasing with time, the total number of nanoparticles decreases.

While Ostwald ripening often occurs over long timescales, we have artificially accelerated its progression in these experiments by exposing the grains here to a rapid succession of heating events to simulate micrometeorite impacts. In this experiment, the npFe particles initially form during the first thermal episode. With each subsequent simulated impact event, the nanoparticles grow in size. Such particle growth is likely driven by the diffusion of Fe from the surrounding matrix to the surface of the nanoparticle, the rate of which may increase significantly during the thermal shocks. Because spherical-shaped nanoparticles are also energetically favoured, some npFe may initially form as euhedral crystals, but subsequent heating events may cause those crystal edges to become rounded, as is observed in our experiments and in materials science applications such as quantum dots and theoretical calculations (Ratke and Voorhees 2013). The particle-size distributions we observe are also consistent with those predicted as a result of Ostwald ripening (Ratke and Voorhees 2013). Beginning with right-skewed populations, with each

thermal episode, the average size of the nanoparticles grows, and the population moves towards a Gaussian or normal distribution. Additionally, one of our grains showed a decrease in the total number of nanoparticles visible after experiencing more heating events. The decrease in total nanoparticle number suggests the grain may have reached a steady-state in terms of the volume of material contained in the nanoparticles resulting in no new npFe but instead only growth of existing grains. If Ostwald ripening is controlling the growth and size distribution of npFe in lunar soils, it may challenge the idea that individual grains are more mature simply if they have a higher concentration of npFe particles. Instead, investigating the shape and size distribution function of nanoparticles may provide more information as to the relative ages of individual soil grains.

Changes in the size-distribution function of npFe within agglutinate grains as a result of multiple heating events could provide valuable insight into the relative ages of grains within a population. The impact flux at 1 AU, e.g., the location of the Moon, has been measured by several spacecraft, including the Galileo dust experiment (Grün et al. 1991). Taking the impact flux of 1 μm dust particles to be around $10^{-4}\text{m}^{-2}\text{s}^{-1}$, a grain covering an area on the surface of the Moon measuring e.g., 5 μm x 5 μm , similar to those in this experiment, would experience 2.5×10^{-15} impacts/s. This number translates to 7.9×10^{-8} impacts/year, or roughly 1 impact/ 10^8 years. Knowing that a grain will probably experience on average one impact during 10^8 years of surface exposure, we can simply equate the grains we subjected to a single thermal event to having roughly 10^8 years of exposure on the lunar surface. Thus, grains that experienced eight total impact events, chosen arbitrarily, may have experienced around 8×10^8 years' worth of surface exposure, and 12 impact events around 10^9 years on the lunar surface. We can then compare the

evolution of the size-distribution functions of npFe within those grains to perhaps place a relative age constraint on exposure times for individual grains within a bulk soil. This would serve as a new technique for relative age dating of grains within a population, and could provide the ability to target agglutinate grains of particular exposures for further study. Such a dating methodology relies on several assumptions, however. The heating experiments performed here only provide size constraints on npFe that formed during micrometeorite impact events, while we know ion irradiation is surely forming nanoparticles simultaneously. For the inferred ages to be truly robust, the size distribution of npFe particles should be analyzed for samples that have only been subjected to varying doses of irradiation, and not simulated impact events. Measurements of irradiated grains npFe distributions could then be combined with the measurements presented here for impacted-grains, to yield a comprehensive npFe size distribution that is representative of surface particles experiencing both space weathering processes simultaneously. It is also important to consider that the duration of these simulations may be significantly longer than the theorized timescale of a real impact event. While the duration of each of these thermal episodes is <1 s, and nominally <0.5 s, impact events on the lunar surface may only last nano- to micro-seconds (Sasaki et al. 2001). The heating stage technology that enables these experiments is still under development, and will eventually be programmable for such short duration episodes. Until such time, this is an important first order approximation of micrometeorite impact events performed in situ, enabling for the first time direct observation of the development and growth of npFe and vesicles in lunar soils.

In Chapter 4, nanoparticles with oxidized shells surrounding reduced cores were described. In that work, however, we did not observe nanoparticles with oxidized *cores*

and reduced *shells*. Were such a nanostructure to occur, it could suggest that a previously oxidized nanoparticle experienced an impact-driven ripening event, which mobilized reduced Fe that diffused towards the surface, surrounding the oxidized interior. This nanostructure could occur in the samples, but may not have been identified due to sampling statistics, as <10% of nanoparticles measured in Chapter 4 exhibited any noticeable core/shell structure at all. Another possibility, however, is that impact events may reduce the Fe that has been oxidized over time back to Fe⁰. The oxidation process may be occurring on shorter-timescales than impact-induced heating (with a frequency of occurrence around once every 10⁸ years). In this case, nanoparticles may become completely oxidized, and then their surfaces may be infrequently reduced when the soil experiences a thermal shock.

While intermittent impact-induced heating may be the dominating factor in controlling the growth of npFe particles in surface samples, intervening temperature changes with a smaller overall magnitude, e.g., diurnal temperature variations, may also contribute to nanoparticle growth. Diurnal temperature variations on the Moon and Mercury can span 300 K and 600 K, respectively (Vasavada et al. 2012; Noble and Pieters 2003). These predictable temperature changes with lower-magnitude may contribute to slow, steady growth rates over long time scales, which are sporadically punctuated by impact events driving more significant changes in nanoparticle size and size distribution. The influence of slower, repeated thermal cycles on the growth and development of npFe particles could be investigated with experiments over longer timescale using the hot-stage technology described here.

5.5 Conclusions

Lunar soils were subjected to slow- and rapid-heating events to simulate micrometeorite impacts on airless body surfaces. This technique provides a novel method for simulating space weathering processes in the laboratory. Heating experiments of lunar soil grains inside the TEM shows that npFe particles form at ~575 °C during slow-heating and as a result of rapid heating events. We observed the formation of vesicles during the thermal shock episodes. This work successfully develops features in the experimental samples that are consistent with naturally space weathered returned samples, including reduced Fe nanoparticles, vesiculated rims, and glassy grain morphologies. The experiments provide insight into the evolution of npFe populations through time, indicating their size distribution follows that which is predicted by growth through Ostwald ripening. In the future, these results may provide the basis for a new methodology for relative age dating of soil grains within a population.

5.6 Acknowledgements

We thank CAPTEM for allocation of lunar samples for this study. We gratefully acknowledge the use of facilities within the Leroy Eyring Center for Solid State Science at Arizona State University, with assistance from Dr. Zhaofeng Gan. We gratefully acknowledge the use of facilities in the Ontario Centre for the Characterization of Advanced Materials, and Dr. Doug Perovic at the University of Toronto for making this project possible. Funding for M.S. Thompson is provided by the NASA Earth and Space Science Fellowship (NESSF). Research supported in part by NASA.

CHAPTER 6

SUMMARY, IMPLICATIONS, AND FUTURE WORK

6.1 Summary

This work employed a multi-faceted approach to understanding space weathering processes. The first component of this study focused on the analysis of returned samples from near-Earth asteroid Itokawa, contributing to the first-ever comparison of microstructural and chemical features of space weathering in returned samples from two different airless bodies. This research used STEM and high-resolution imaging and quantitative EDS measurements to analyze space weathering characteristics in an Itokawa soil grain. These analyses confirmed that space weathering is operating on the surface of near-Earth asteroids, and that many of the resulting features have similarities to those observed in lunar soils. This work showed that while there is evidence that both major constituent space weathering processes are operating on the surface of Itokawa, solar wind irradiation appears to be the dominant contributor to changes in the microstructure and chemistry of surface material for the grain studied. This finding is in contrast to the important role that micrometeorites play on the lunar surface. Analyses of irradiation-produced rims also indicate that grains on the surface of Itokawa have a complex exposure history.

The second component of this work presented a detailed study of nanophase Fe particles in lunar soil samples. For the first-time, the oxidation state of individual npFe particles was directly measured using cutting-edge EELS techniques in the TEM. The results show that npFe particles are oxidizing over their time on the lunar surface, and

that the amount of oxidized Fe in the nanoparticles is correlated with soil maturity. The EELS data were also coupled to atomic- and high-resolution imaging that was used to determine the microstructure of the nanoparticles, confirming their mineral phase. This work challenged the long-standing paradigm in the space weathering community that all npFe particles are composed of metallic Fe and that the chemical composition of these features remains static after their formation. The TEM work was coupled to a theoretical modeling investigation of the influence that npFe particles of different oxidation states have on the spectral properties of the material. This work showed that varying the oxidation state of nanoparticles can produce subtle changes in the optical properties of the soils, and should be accounted for in modeling reflectance spectra.

The third and final component of this research presented a novel technique for simulating space weathering processes inside the TEM. Using a specialized sample holder, lunar soils were subjected to both slow- and rapid-heating events to simulate micrometeorite impacts. The slow-heating experiments provided a temperature constraint on initial npFe formation at around ~ 575 °C. Grains subjected to single thermal pulses, up to 1000 °C and back to room temperature in $\ll 1$ second, showed the development of npFe grains and vesiculated textures near the grain rim. These features were analyzed using SE and STEM imaging, and qualitative EDS mapping, and the oxidation state of the npFe grains was confirmed to be Fe^0 using EELS. The similarity of these features to naturally space weathered samples indicates that this methodology was accurately mimicking space weathering processes occurring on airless body surfaces. Several grains were subjected to multiple thermal shocks to simulate longer exposure times on the lunar surface. With each heating cycle, the number and size distribution of the npFe particles

changed. These results provide insight into the particle growth dynamics for space weathered soils and could provide a new way to place relative age constraints on grains in lunar soil.

6.2 Implications and Future Work

This work was motivated by many outstanding questions in the field of space weathering, as outlined in section 1.5. The results of these experiments speak to those questions, providing insight into how space weathering processes operate on airless bodies and provide a broader understanding of the evolution of their surfaces. The results from Chapter 3, analyzing space-weathering features in Itokawa samples, have shown that the microstructural and chemical characteristics of space weathering are similar in surface soils from different airless bodies, but that the relative contributions of those processes may vary significantly. This is a new insight for the field, and contributes to the development of an overall space-weathering model for the solar system. The results from Chapter 4, show for the first time that npFe particles contain Fe in a variety of oxidation states, challenging decades of fundamental assumptions about the chemical reactions driving space weathering processes. This work used cutting-edge techniques to provide new, formerly unobtainable information on processes previously thought to be well-established, motivating the community to reevaluate their understanding of space weathering as a whole. Chapter 5 provides an entirely new methodology for simulating space weathering processes in the laboratory, through in situ heating in the TEM. This work enables the first direct observation of the formation of npFe, and tracks their evolution and growth with continued simulated exposure. These results give new insight

into how npFe populations change over time, calling into question the simple assumption that more mature grains simply have more nanoparticles. Rather, size distribution should be considered as a new parameter for which we measure soil maturity.

While each of these experiments performs detailed measurements of returned or experimental samples inside the TEM, the influence their results have on our understanding of space weathering is far reaching. More than simply answering long-standing questions in the field, this work poses new ones. We know that space weathering on Itokawa is dominated by solar wind processes, but why? Does this speak to the dynamic history of the surface of Itokawa itself, or can it be extended to other asteroids, even in the main-belt? We understand now that nanoparticles in lunar soils are not simply composed of Fe⁰, but how will this impact our interpretation of reflectance measurements for planetary surfaces? Can we extend these oxidation processes to any surface with mature soils? Will oxidation occur in nanoparticles on Itokawa? New techniques for simulating space weathering in the TEM have provided the first direct observation of the development of npFe grains, confirming a long-proposed formation mechanism fundamental to our understanding of space weathering. These experiments also enabled the observation of the evolution of npFe populations over time, showing that, contrary to assumptions, more mature soils do not necessarily have more nanoparticles. Should we reevaluate how we classify soil maturity? How do these experimental results compare to returned samples? Each of these new questions can be addressed with future work on lunar soils and Itokawa samples. However, the space weathering community should expand beyond bodies from which we have samples and look toward the next frontier.

There are two current sample-return missions to near-Earth asteroids in the planetary science community: NASA's OSIRIS-REx mission and JAXA's Hayabusa II mission. The target planetary bodies for these missions are carbonaceous asteroids. The eventual sample return from these missions will open a new world of possibility for understanding space weathering processes on airless body surfaces. The community should begin to prepare for the science return of these missions by exploring new questions. How do the optical properties of carbonaceous materials change in response to space weathering? How do hydrated minerals or organic material respond chemically and microstructurally to solar-wind irradiation and impact events? Do these processes radically change the composition and/or functionality of organics in the material, possibly thought to seed our own planet? With these missions on the horizon, the community has an opportunity to broaden the entire scope of understanding for space weathering processes. Beyond just carbonaceous materials, the community should expand to study the weathering of ices and rock-ice mixtures relevant to comets and outer-solar system bodies that will undoubtedly be the target of future missions. By applying the techniques discussed here to a new and diverse set of samples, we can further contribute to an overall space-weathering model, which could be applied across the solar system.

The heart of this work lies in the TEM techniques used to achieve these results. The future of TEM analyses in planetary science is bright. The ability of the FIB to prepare site-specific samples for analysis in the TEM enables targeted investigations of fine-scale features without the loss of broader context. Combining chemical and microstructural information down to the atomic scale is a capability unique to TEM, offering the ability to provide insight relevant to the largest-scale questions across the

field. Recent advances in electron optics have enabled the measurement of compositional information of atomic-columns, opening the smallest scales to investigations about the formation and modification of planetary materials. The application of in situ experimental TEM also provides a fundamentally new laboratory capability for planetary scientists. The ability to observe chemical and structural changes occurring as a result of e.g., thermal shocks, could have applications to many types of planetary materials. These hot stage experiments are versatile and could be applied to e.g., annealing studies of radiation damage in presolar grains, chondrules, and calcium-aluminum-rich inclusion formation mechanisms and subsequent phase changes, airless body thermal cycling etc. The TEM will continue to be important to our study of planetary materials, and as such, our understanding of the formation and evolution of the solar system.

APPENDIX A

CAMERA CONSTANTS DETERMINED FOR THE JEOL 2010 AT ASU

Table A1: 2013 Camera Constants for Image Size 2688 x 2672 px

Camera Length (mm)	Camera Constant (pxÅ)
150	607.0
200	800.0
250	1001.4
300	1197.6
400	1595.5
500	1983.6
600	2364.5

Table A2: 2015 Camera Constants for Image Size 1344 x 1336 px

Camera Length (mm)	Camera Constant (pxÅ)
80	166.2
100	208.6
120	251.4
150	313.4
200	411.9
250	515.3
300	620.6
400	816.9
500	1016.8
600	1218.0

Table A3: 2015 Camera Constants for Image Size 2688 x 2672 px

Camera Length (mm)	Camera Constant (pxÅ)
80	332.3
100	417.1
120	502.8
150	626.8
200	823.9
250	1030.6
300	1241.2
400	1633.7
500	2033.6
600	2436.1

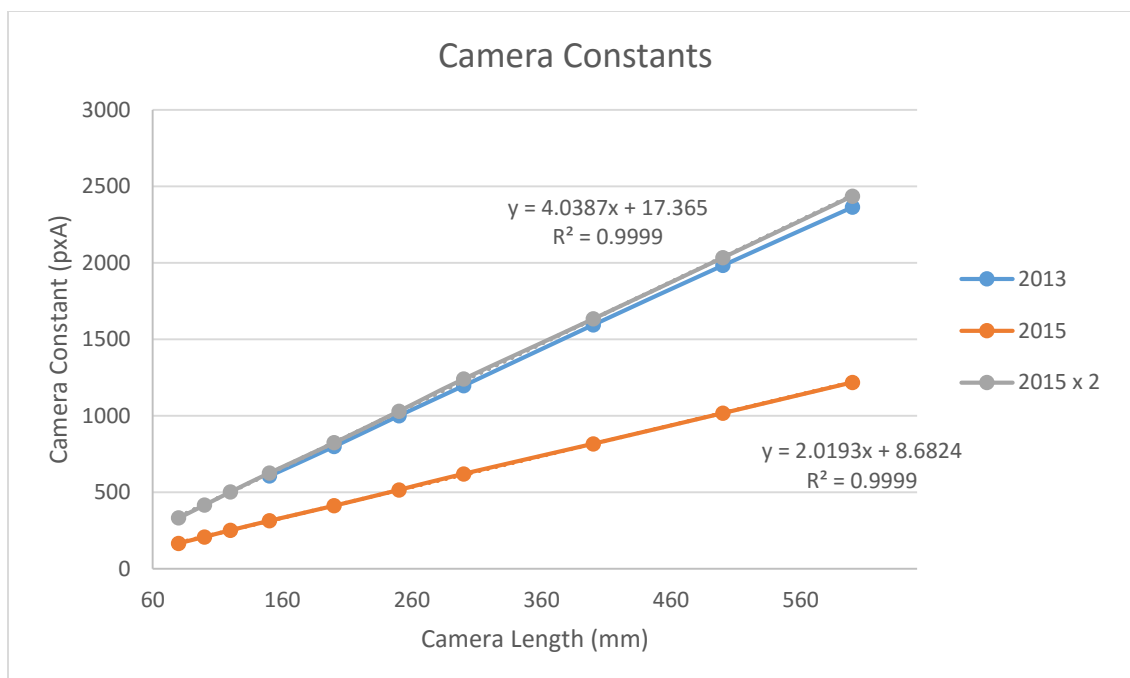


Figure A1: Comparison between 2013 and 2015 camera constants. Equations for lines of best fit are shown.

APPENDIX B

LINEAR, LEAST-SQUARES FITTING PROGRAM

Author: J. T. Keane

Coded in MATLAB

%% Simple GUI

function JTK_SpectraFitter_GUI_141027(inputfilename)

close all

global X Y Y1 Y2 Y3 Emin1 Emax1 p1 p2 p3 pf pr fontn fonts y1 y2 y3 k1 k2 k3 p0
shiftval YS x y filename0

%-----

%- standards

FE2PLUS_FILENAME='Fe 2 Plus.txt';

FE3PLUS_FILENAME='Fe 3 Plus.txt';

FEMETAL_FILENAME='Fe Metal_2.txt';

FE2PLUS_i=0;

FE3PLUS_i=0;

FEMETAL_i=0;

%- creating blank array to store all the results

nfiles=4;

```

DATA=zeros(5000,4,nfiles);

COVD=zeros(nfiles,1);

%- range of energy to consider:

Emin = 690;

Emax = 750;

for i=1:1:4

%- loading data

    if i==1

        FE2PLUS_i=1;

        filename=FE2PLUS_FILENAME;

    elseif i==2

        FE3PLUS_i=2;

        filename=FE3PLUS_FILENAME;

    elseif i==3

        FEMETAL_i=3;

        filename=FEMETAL_FILENAME;

    elseif i==4

        filename=inputfilename;

        filename0=inputfilename;

    end

    dat=importdata(filename);

    x=dat(:,1);          % energy

```

```

y=dat(:,2);          % flux

%- normalizing amplitude of spectra
y=y/max(y);

%- trimming data to be within acceptable energy range
r1=x>=Emin;r2=x<=Emax;r3=r1+r2;r=r3==2;
x=x(r);y=y(r);

%- background subtraction;
y2=y.*0;

% low energy background
r1_lim=700;
r=x<=r1_lim;
polyorder=1;

[p,~,mu]=polyfit(x(r),y(r),polyorder);
yp=polyval(p,x,[],mu);
yp1=polyval(p,r1_lim,[],mu);
y2(r)=yp(r);

% high energy background

```

```

r2_lim=735;

r=x>=r2_lim;

    polyorder=1;

[p,~,mu]=polyfit(x(r),y(r),polyorder);

yp=polyval(p,x,[],mu);

yp2=polyval(p,r2_lim,[],mu);

y2(r)=yp(r);

```

% connecting these two

```

r1=x<r2_lim;

r2=x>r1_lim;

r3=r1+r2;

r=r3==2;

polyorder=1;

```

```

[p,~,mu]=polyfit([r1_lim r2_lim],[yp1 yp2],1);

yp=polyval(p,x,[],mu);

y2(r)=yp(r);

```

%- corrected flux

```

y3=y-y2;

y3=y3/max(y3);

```



```

COVD(i)=var(y3(r==0));

%- storing data

DATA(1:numel(x),1,i)=x;

DATA(1:numel(x),2,i)=y;

DATA(1:numel(x),3,i)=y2;

DATA(1:numel(x),4,i)=y3;

end

k=4;

%-- FE 2+

x1= squeeze(DATA(:,1,FE2PLUS_i));

y1o=squeeze(DATA(:,2,FE2PLUS_i));

y1= squeeze(DATA(:,4,FE2PLUS_i));

x1=x1(y1o~=0);

y1=y1(y1o~=0);

%-- FE 3+

x2= squeeze(DATA(:,1,FE3PLUS_i));

y2o=squeeze(DATA(:,2,FE3PLUS_i));

y2= squeeze(DATA(:,4,FE3PLUS_i));

x2=x2(y2o~=0);

```

```
y2=y2(y2o~=0);
```

```
%-- FE M
```

```
x3= squeeze(DATA(:,1,FEMETAL_i));
```

```
y3o=squeeze(DATA(:,2,FEMETAL_i));
```

```
y3= squeeze(DATA(:,4,FEMETAL_i));
```

```
x3=x3(y3o~=0);
```

```
y3=y3(y3o~=0);
```

```
%- sample to fit
```

```
x= squeeze(DATA(:,1,k));
```

```
yo=squeeze(DATA(:,2,k));
```

```
y= squeeze(DATA(:,4,k));
```

```
x=x(yo~=0);
```

```
y=y(yo~=0);
```

```
%- resampling
```

```
spc=max([x1(2)-x1(1); x2(2)-x2(1); x3(2)-x3(1); x(2)-x(1)]);
```

```
Emin1=max([min(x1) min(x2) min(x3) min(x)]);
```

```
Emax1=min([max(x1) max(x2) max(x3) max(x)]);
```

```
X=Emin1:spc:Emax1;
```

```
Y1=interp1(x1,y1,X);
```

```
Y2=interp1(x2,y2,X);
```

```

Y3=interp1(x3,y3,X);

Y=interp1(x,y,X);

%- renormalizing

Y1=Y1/max(Y1);

Y2=Y2/max(Y2);

Y3=Y3/max(Y3);

Y=Y/max(Y);

%-----

%-- creating GUI window

figure('position',[73      251      1375      1102],...

       'name', 'JTK_SpectraFitter_GUI_140925',...

       'NumberTitle', 'off');clf;

subplot('position',[0.1 0.3 0.8 0.6]);

hold on;

fontn='arial';

fontsize=16;

set(gca,'fontname',fontn,'fontsize',fontsize,...

      'tickdir','out','box','on','layer','bottom')

% dummy plots, to be deleted when cycled

p1=plot(0,0,'ok','markerfacecolor','r','color','r');

```

```

p2=plot(0,0,'ok','markerfacecolor','g','color','g');
p3=plot(0,0,'ok','markerfacecolor','b','color','b');
pf=plot(0,0,'ok','markerfacecolor',[247 73 148]/255,'color',[247 73 148]/255);
pr=plot(0,0,'ok','markerfacecolor',[200 200 200]/255,'color',[200 200 200]/255);

y1=Y.*0;
y2=Y.*0;
y3=Y.*0;
YS=Y;

k1=0;
k2=0;
k3=0;

%-- sliding the sample left and right
%- label

uicontrol('Style','text','String','Shifting Sample:',...
          'Position',[150 160 200 20],...
          'fontname',fontn,'fontsize',fonts,'ForegroundColor','k');

%- slider

uicontrol('Style','slider','Min',-10,'Max',10,...
          'Position',[350 160 300 20],'Callback',@PlotGUI_4);

%    %- label

```

```

%   uicontrol('Style','text','String','Fe 2+',...
%       'Position',[150 100 90 20],...
%       'fontname',fontn,'fontsize',fonts,'ForegroundColor','r');

%   %- slider

%   uicontrol('Style','slider','Min',0,'Max',2,...
%       'Position',[250 100 200 20],'Callback', @PlotGUI_1);


%-- slider output label

    uicontrol('Style','text','String','Weights:',...
        'Position',[700 140 90 60],...
        'fontname',fontn,'fontsize',fonts);

%-- slider output label

    uicontrol('Style','text','String','Normalized Mixing Ratios:',...
        'Position',[850 140 90 60],...
        'fontname',fontn,'fontsize',fonts);

%-- slider output label

    uicontrol('Style','text','String','R^2',...
        'Position',[1000 140 90 60],...
        'fontname',fontn,'fontsize',fonts);

%-- amplitude slider #1

%- label

    uicontrol('Style','text','String','Fe 2+',...
        'Position',[150 100 90 20],...

```

```

        'fontname',fontn,'fontsize',fonts,'ForegroundColor','r');

%- slider

uicontrol('Style','slider','Min',0,'Max',2,...

        'Position',[250 100 400 20],'Callback',@PlotGUI_1);

%-- amplitude slider #1

%- label

uicontrol('Style','text','String','Fe 2+',...

        'Position',[150 100 90 20],...

        'fontname',fontn,'fontsize',fonts,'ForegroundColor','r');

%- slider

uicontrol('Style','slider','Min',0,'Max',2,...

        'Position',[250 100 400 20],'Callback',@PlotGUI_1);

%-- amplitude slider #2

%- label

uicontrol('Style','text','String','Fe 3+',...

        'Position',[150 70 90 20],...

        'fontname',fontn,'fontsize',fonts,'ForegroundColor','g');

%- slider

uicontrol('Style','slider','Min',0,'Max',2,...

        'Position',[250 70 400 20],'Callback',@PlotGUI_2);

%-- amplitude slider #3

%- label

```

```

uicontrol('Style','text','String','Fe M',...

    'Position',[150 40 90 20],...

    'fontname',fontn,'fontsize',fontz,'ForegroundColor','b');

%- slider

uicontrol('Style','slider','Min',0,'Max', 2,...

    'Position',[250 40 400 20],'Callback', @PlotGUI_3);

%-- save button

uicontrol('Style','pushbutton','String','SAVE DATA',...

    'Position',[1150 80 100 20],...

    'fontname',fontn,'fontsize',fontz,'ForegroundColor','b',...

    'Callback', @PlotGUI_5);

%-- plotting stuffs

%-- plotting observed spectrum

clr=[0 0 0];

p0=plot(X,Y,'-k','linewidth',5,'color',clr);

%-- plot options

ylim([-0.4 1.2])

xlim([Emin1-1 Emax1+1]);

xlim0=get(gca,'xlim');

ylim0=get(gca,'ylim');

plot([xlim0(1) xlim0(2)],[ylim0(1) ylim0(1)],'-k','linewidth',2)

plot([xlim0(1) xlim0(2)],[ylim0(2) ylim0(2)],'-k','linewidth',2)

plot([xlim0(1) xlim0(1)],[ylim0(1) ylim0(2)],'-k','linewidth',2)

```

```
plot([xlim0(2) xlim0(2)],[ylim0(1) ylim0(2)],'-k','linewidth',2)
```

```
ylabel('Normalized Flux');
```

```
xlabel('Energy (eV)');
```

```
title(inputfilename,'interpreter','none',...
```

```
    'fontname',fontn,'fontsize',fonts);
```

```
l1=legend([p0 p1 p2 p3 pf pr],...
```

```
    ' Particle',...
```

```
    ' Fe 2+ Standard',...
```

```
    ' Fe 3+ Standard',...
```

```
    ' Fe Metal Standard',...
```

```
    ' Linear Combination',...
```

```
    ' Residuals');
```

```
set(l1,'box','off')
```


APPENDIX C

HAPKE REFLECTANCE MODEL OF THE OPTICAL EFFECTS OF SPACE WEATHERING ON LUNAR SOILS

Author: P. Becerra

Coded in IDL

:: Hapke Reflectance Model for the Optical effects of Space Weathering v1.0 (4/14/2015)

:: Angle Conversions ::

d2r = **!dpi/180.d** ; degrees to radians

r2d = **180.d/!dpi** ; radians to degrees

:: Fixed Parameters and start values ::

lambda = (**dindgen(1600)+200.d**)/**1d9** ; wavelength range 0.2-2.5 um)

i = **30.d***d2r

e = **30.d***d2r

mu0 = **cos**(i)

mu = **cos**(e)

:: Host material calculations ::

n_h = **1.7d** ; host real absorption coefficient

d_h = **16d-6** ; grain size

$se = ((n_h - 1.d)^{2.d} / ((n_h + 1.d)^{2.d})) + 0.05d$; Hapke (2001) eq. 19

$si = 1.d - (4.d / (n_h * (n_h + 1.d)^{2.d}))$; Hapke (2001) eq. 20

;; Standard Reflectance (particulate medium with $w = 1$ at same angles) ;;

$w_{std} = 1.d$

$\gamma_{std} = \sqrt{1.d - w_{std}}$

$H_{mu0_std} = (1.d + 2.d * \mu_0) / (1.d + 2.d * \gamma_{std} * \mu_0)$

$H_{mu_std} = (1.d + 2.d * \mu) / (1.d + 2.d * \gamma_{std} * \mu)$

$r_{std} = (w_{std} / (4.d * !dpi)) * (\mu_0 / (\mu + \mu_0)) * (H_{mu_std} * H_{mu0_std})$

print, 'This is R_standard:', r_{std}

;; Rock Reflectance ;;

dummy = **double**((**read_ascii**('hapkefig27_rock10022.txt', data_start = 1)).field1)

;reading in measured lunar rock bidirectional reflectance

$w_l = \text{reform}(\text{dummy}(0,*))$

$r_{rock} = \text{reform}(\text{dummy}(1,*))$

$r_{rock} = \text{interpol}(r_{rock}, w_l/1d6, \lambda)$; sample reflectance (fe)

$\gamma_{mu0_rock} = r_{rock} / r_{std}$; Relative Reflectance

$\gamma_{mu_rock} = ((\sqrt{((\mu_0 + \mu)^{2.d}) * (\gamma_{mu0_rock}^{2.d}) + (1.d +$

$$\frac{4.d * \mu_0 * \mu * \text{gamm0_rock} * (1.d - \text{gamm0_rock}) - (\mu_0 + \mu) * \text{gamm0_rock}}{(1.d + 4.d * \mu_0 * \mu * \text{gamm0_rock}) + (\sqrt{((\mu_0 + \mu)^2.d * (r_sam^2.d) + (1.d + 4.d * \mu_0 * \mu * r_sam) * (1.d - r_sam)) - (\mu_0 + \mu) * r_sam})} / (1.d + 4.d * \mu_0 * \mu)$$

w_rock = 1.d - gamm_rock^2.d ; use this to average with glass and find host w

alph_rock = (1.d / d_h) * **alog**(si + ((1.d - se)*(1.d - si) / (w_rock-se))) ; Hapke (2001)

eq. 23b use only for proof below

; Proof of model r_rock should be equal to rm_rock ;

$$H_{\mu_0} = (1.d + 2.d * \mu_0) / (1.d + 2.d * \text{gamm_rock} * \mu_0)$$

$$H_{\mu} = (1.d + 2.d * \mu) / (1.d + 2.d * \text{gamm_rock} * \mu)$$

$$r_{m_rock} = (w_rock / (4.d * \pi)) * (\mu_0 / (\mu + \mu_0)) * (H_{\mu} * H_{\mu_0})$$

:: Glass Reflectance ::

dummy = **double**((**read_ascii**('hapkefig27_glass10022.txt', data_start = 1)).field1)

;reading in measured lunar rock bidirectional reflectance

wl = **reform**(dummy(0,*))

rglass = **reform**(dummy(1,*))

r_glass = **interpol**(rglass, wl/1d6 , **lambda**) ; sample reflectance (fe)

gamm0_glass = r_glass/r_std ; Relative Reflectance

$$\text{gamm_glass} = \left(\left(\sqrt{((\mu_0 + \mu)^{2d}) * (\text{gamm0_glass}^{2d}) + (1d + 4d * \mu_0 * \mu * \text{gamm0_glass}) * (1d - \text{gamm0_glass})} \right) - (\mu_0 + \mu) * \text{gamm0_glass} \right) / (1d + 4d * \mu_0 * \mu * \text{gamm0_glass}) ; \left(\left(\sqrt{((\mu_0 + \mu)^{2d}) * (r_sam^{2d}) + (1d + 4d * \mu_0 * \mu * r_sam) * (1d - r_sam)} \right) - (\mu_0 + \mu) * r_sam \right) / (1d + 4d * \mu_0 * \mu)$$

$w_glass = 1d - \text{gamm_glass}^{2d}$; use this to average with rock and find host w

$$\text{alph_glass} = (1d / d_h) * \log(\text{si} + ((1d - se) * (1d - \text{si}) / (w_glass - se))) ; \text{Hapke (2001)}$$

eq. 23b use only for proof below

; Proof of model r_glass should be equal to r_m_glass ;

$$H_{\mu_0} = (1d + 2d * \mu_0) / (1d + 2d * \text{gamm_glass} * \mu_0)$$

$$H_{\mu} = (1d + 2d * \mu) / (1d + 2d * \text{gamm_glass} * \mu)$$

$$r_m_glass = (w_glass / (4d * \pi)) * (\mu_0 / (\mu + \mu_0)) * (H_{\mu} * H_{\mu_0})$$

:: Host Absorption Coefficient ::

$$w_h = (w_rock + w_glass) / 2d$$

$$\text{alph_h} = (1d / d_h) * \log(\text{si} + ((1d - se) * (1d - \text{si}) / (w_h - se)))$$

$$;\text{alph_h} = \text{alph_rock}$$

$$;\text{alph_h} = \text{alph_glass}$$

```
:: Real Soil Data Input ::
```

```
dummy = double((read_ascii('hapkefig27_soil10084.txt', data_start = 1)).field1) ;reading  
in measured lunar rock bidirectional reflectance
```

```
wl = reform(dummy(0,*))
```

```
rsoil = reform(dummy(1,*))
```

```
r_soil = interpol(rsoil, wl/1d6 , lambda) ; sample reflectance (fe) *note: this is the  
equivalent to the relative reflectance of the sample soil. must be multiplied by r_std in order  
to be compared with r_w from below.
```

```
:: Weathered Material Calculations ::
```

```
:: Fe inclusions ::
```

```
:: Fe ::
```

```
:: Johnson and Christy (1974) ::
```

```
dummy = double((read_ascii('Fe_Johnson.txt', data_start = 1)).field1) ;reading in optical  
constants for Iron from ascii file (Johnson and Christie)
```

```
wl = reform(dummy(0,*))
```

```
n = reform(dummy(1,*))
```

```
k = reform(dummy(2,*))
```

```
n_fe = interpol(n, wl/1d6 , lambda) ;real part of complex index of refraction (fe)
```

k_fe = **interp**(k, wl/**1d6** , **lambda**) ;imaginary part of complex index of refraction (fe)

;; FeO (Fe2+ proxy) ;;

;; Henning (1995) ;;

dummy = **double**((**read_ascii**('FeO_0.2-2.5.txt', data_start = **1**)).*field1*) ;reading in optical constants for FeO from ascii file (Henning)

wl = **reform**(dummy(**0**,*))

n = **reform**(dummy(**1**,*))

k = **reform**(dummy(**2**,*))

n_fe2 = **interp**(n, wl/**1d6** , **lambda**) ;real part of complex index of refraction (fe)

k_fe2 = **interp**(k, wl/**1d6** , **lambda**) ;imaginary part of complex index of refraction (fe)

;; Fe2O3 (Fe3+ proxy) ;;

;; Amaury (unpublished) ;;

dummy = **double**((**read_ascii**('Fe2O3_0.18-2.5.txt', data_start = **1**)).*field1*) ;reading in optical constants for Fe2O3 from ascii file (Amaury)

wl = **reform**(dummy(**0**,*))

n = **reform**(dummy(**1**,*))

k = **reform**(dummy(**2**,*))

$n_{fe3} = \text{interpol}(n, wl/1d6, \lambda)$;real part of complex index of refraction (fe)

$k_{fe3} = \text{interpol}(k, wl/1d6, \lambda)$;imaginary part of complex index of refraction (fe)

;; Iron inclusions absorption coefficient ;;

$\rho_h = 2900.d$; density of host material (basalt kg/m3)

$mf = 0.005d$

;; Fe ;;

$mf = 0.005d$

$\rho_{fe} = 7900.d$; kg/m3

$$zed = ((n_h^{3.d} * n_{fe} * k_{fe}) / ((n_{fe}^{2.d} - k_{fe}^{2.d} + 2.d * n_h^{2.d})^{2.d} + (2.d * n_{fe} * k_{fe})^{2.d})$$

$\alpha_{fe} = (36.d * \pi / \lambda) * zed * \rho_h / \rho_{fe}$

$\alpha_{fe} = (36.d * \pi / \lambda) * zed * mf * \rho_h / \rho_{fe}$;use only for single-component weathering

;; FeO (Fe2+) ;;

$mf2 = 0.005d$

$\rho_{fe2} = 5700.d$; kg/m3

$$\text{zed} = ((n_h^{3.d} * n_{fe2} * k_{fe2}) / ((n_{fe2}^{2.d} - k_{fe2}^{2.d} + 2.d * n_h^{2.d})^{2.d} + (2.d * n_{fe2} * k_{fe2})^{2.d})$$

$$\text{alph}_{fe2} = (36.d * !dpi / \lambda) * \text{zed} * \rho_h / \rho_{fe2}$$

$$; \text{alph}_{fe2} = (36.d * !dpi / \lambda) * \text{zed} * mf2 * \rho_h / \rho_{fe2} \quad ; \text{use}$$

only for single-component weathering

:: Fe₂O₃ (Fe³⁺) ::

$$; mf3 = 0.005d$$

$$\rho_{fe3} = 5260.d ; \text{ kg/m}^3$$

$$\text{zed} = ((n_h^{3.d} * n_{fe3} * k_{fe3}) / ((n_{fe3}^{2.d} - k_{fe3}^{2.d} + 2.d * n_h^{2.d})^{2.d} + (2.d * n_{fe3} * k_{fe3})^{2.d})$$

$$\text{alph}_{fe3} = (36.d * !dpi / \lambda) * \text{zed} * \rho_h / \rho_{fe3}$$

$$; \text{alph}_{fe3} = (36.d * !dpi / \lambda) * \text{zed} * mf3 * \rho_h / \rho_{fe3} \quad ; \text{use}$$

only for single-component weathering

:: Reflectance of unweathered host soil ::

$$\text{gamm}_{uw} = \sqrt{1.d - w_h}$$

$$H_{mu0} = (1.d + 2.d * \mu_0) / (1.d + 2.d * \text{gamm}_{uw} * \mu_0)$$

$$H_{mu} = (1.d + 2.d * \mu) / (1.d + 2.d * \text{gamm}_{uw} * \mu)$$

$$r_{uw} = (w_h / (4.d * !dpi)) * (\mu_0 / (\mu + \mu_0)) * (H_{\mu} * H_{\mu_0})$$

$$gamm_{host} = (1.d - gamm_{uw}^{2.d}) / ((1.d + 2.d * gamm_{uw} * \mu_0) * (1.d + 2.d * gamm_{uw} * \mu))$$

;; Weathered reflectance calculation ;;

$$d_p = 26.d - 6$$

$$p1 = 0.14.d$$

$$p2 = 0.71.d$$

$$p3 = 0.15.d$$

$$\alpha_w = \alpha_h + mf * (p1 * \alpha_{fe} + p2 * \alpha_{fe2} + p3 * \alpha_{fe3})$$

; If s = 0 ;

$$\theta_w = \exp(-\alpha_w * d_p)$$

$$; \text{ if inclusions are in rims: } \theta_w = \theta_w * \exp((36.d * !dpi / \lambda) * zed * mf3 * \rho_h / \rho_{fe3} * d_p)$$

$$w_w = se + (1.d - se) * ((1.d - si) / (1.d - si * \theta_w)) * \theta_w$$

$$gamm_w = \sqrt{1.d - w_w}$$

$$H_{\mu_0} = (1.d + 2.d * \mu_0) / (1.d + 2.d * gamm_w * \mu_0)$$

$$H_{\mu} = (1.d + 2.d * \mu) / (1.d + 2.d * gamm_w * \mu)$$

$$r_w = (w_w / (4.d * !dpi)) * (\mu_0 / (\mu + \mu_0)) * (H_{\mu} * H_{\mu_0})$$

$$\text{gamm_soil} = (1.d - \text{gamm_w}^{2.d}) / ((1.d + 2.d * \text{gamm_w} * \mu_0) * (1.d + 2.d * \text{gamm_w} * \mu))$$

$$\text{rel_r_w} = r_w / r_{\text{std}}$$

; If s > 0 ;

;sw = 6.d

$$r_1 = (\sqrt{1.d + \text{alph_w}/\text{sw}} - 1.d) / (\sqrt{1.d + \text{alph_w}/\text{sw}} + 1.d)$$

$$\text{theta_w} = (r_1 + \exp(-\sqrt{\text{alph_w} * (\text{alph_w} + \text{sw})) * d_p}) / (1.d + r_1 * \exp(-\sqrt{\text{alph_w} * (\text{alph_w} + \text{sw})) * d_p}))$$

$$\text{; if inclusions are in rims: theta_w} = \text{theta_w} * \exp((36.d * !dpi / \lambda) * \text{zed} * m_{f3} * \rho_h / \rho_{\text{fe3}} * d_p)$$

$$w_w = s_e + (1.d - s_e) * ((1.d - s_i) / (1.d - s_i * \text{theta_w})) * \text{theta_w}$$

$$\text{gamm_w} = \sqrt{1.d - w_w}$$

$$H_{\mu_0} = (1.d + 2.d * \mu_0) / (1.d + 2.d * \text{gamm_w} * \mu_0)$$

$$H_{\mu} = (1.d + 2.d * \mu) / (1.d + 2.d * \text{gamm_w} * \mu)$$

$$r_w = (w_w / (4.d * !dpi)) * (\mu_0 / (\mu + \mu_0)) * (H_{\mu} * H_{\mu_0})$$

$$\text{gamm_soil} = (1.d - \text{gamm_w}^{2.d}) / (1.d + 2.d * \text{gamm_w} * \mu_0) * (1.d + 2.d * \text{gamm_w} * \mu)$$

```
;rel_r_w = r_w / r_std
```

```
:: Plotting Output ::
```

```
;Run one time with these three uncommented:
```

```
plot1 = plot(lambda*1d6, r_rock, thick = 2, xtitle = 'Wavelength ( $\mu\text{m}$ )', ytitle =  
'Reflectance', dimensions = [1000,800],axis_style=2, margin=[0.1,0.1,0.05,0.1], xstyle =  
1, ystyle =1, font_size = 18, xrange = [0,2.0],yrange = [0,0.4], title = 'Hapke Reflectance  
Model', name = 'Pulverized Rock')
```

```
plotgl = plot(lambda*1d6, r_glass, thick = 2, name = 'Pulverized Glass',/overplot, color =  
'gray')
```

```
plotsoil = plot(lambda*1d6, r_soil*r_std, thick = 2, name = 'Soil',/overplot, color = 'blue')
```

```
plotuw = plot(lambda*1d6, r_uw, thick = 2, name = 'Soil',/overplot, color = 'green')
```

```
;Run again with desired proportions for the model weathered soil (e.g. immature soil), then  
run this command in the console:
```

```
;plotim = plot(lambda*1d6, r_w, thick = 2, name = 'Immature Soil Model',/overplot, color  
= 'red') ;Immature Soil
```

```
;Run again with desired proportions for the model weathered soil (e.g. submature soil),  
then run this command in the console:
```

```
;plotsub = plot(lambda*1d6, r_w, thick = 2, linestyle = 1,name = 'Submature Soil  
Model',/overplot, color = 'red') ;Submature Soil
```

;Run again with desired proportions for the model weathered soil (e.g. mature soil), then run this command in the console:

```
;plotma = plot(lambda*1d6, r_w, thick = 2, linestyle = 2,name = 'Mature Soil  
Model',/overplot, color = 'red') ;Mature Soil
```

:: Writing Text Files ::

```
;write_csv, 'mature.txt', lambda*1d6, r_w, header = ['wavelength', 'reflectance'],  
table_header = 'Mature Soil Model'
```

```
;write_csv, '/ model_rel_fe3_0.5.txt', lambda*1d6, gamm_soil, header = ['wavelength',  
'relative reflectance'], table_header = 'Model Soil with Fe2O3 (0.5%)'
```

end

APPENDIX D

D.1 PEER-REVIEWED PUBLICATIONS

Thompson, M.S., Zega, T.J., and Howe, J.Y. 2016. In situ experimental formation and growth of npFe particles and vesicles in lunar soil. *Meteoritics and Planetary Science* (submitted).

Thompson, M.S., Zega, T.J., Becerra, P., Keane, J.T., and Byrne, S. 2016. The Oxidation State of Nanophase Fe Particles in Lunar Soil: Implications for Space Weathering. *Meteoritics and Planetary Science* (accepted).

Bolser, D., Zega, T.J., Asaduzzaman, A., Bringuier, S., Simon, S., Grossman, L., **Thompson, M.S.**, and Domanik K. J. 2016. Microstructural analysis of Wark-Lovering Rims in the Allende and Axtell CV3 chondrites: Implications for high-temperature nebular processes. *Meteoritics and Planetary Science* (in press).

Miller, K.E., Lauretta, D.S., Berger, E.L., **Thompson, M.S.**, Zega, T.J., and Jackson, K. 2016. Chalcopyrite in the Rumuruti Chondrites: Evidence of unique parent body conditions. *Geochimica et Cosmochimica Acta* (in preparation).

Thompson, M.S., Christoffersen, R., Zega, T.J., and Keller, L.P. 2014. Microchemical and structural evidence for space weathering in soils from asteroid Itokawa. *Earth, Planets and Space* **66**:89.

D.2 CONFERENCE ABSTRACTS

Thompson, M.S., Zega, T.J., and Howe, J.Y. 2016. In Situ Heating of Lunar Soil in the Transmission Electron Microscope: Simulating Micrometeorite Impacts. *Microscopy and Microanalysis Conference*.

Thompson, M.S., Zega, T.J., and Howe, J.Y. 2016. Simulation of Micrometeorite Impacts through In Situ Dynamic Heating of Lunar Soil. *LPSC Abstract 2744*. Oral Presentation.

Thompson, M.S., Zega, T.J., Keane, J.T., Becerra, P. and Byrne, S. 2015. The Oxidation State of Fe Nanoparticles in Lunar Soil: Implications for Space Weathering. *Workshop on the Space Weathering of Airless Bodies. Abstract 2017*. Oral Presentation.

Thompson, M.S., and Zega, T.J. 2015. Simulation of Micrometeorite Impacts through in situ Dynamic Heating of Lunar Soil. *Workshop on the Space Weathering of Airless Bodies. Abstract 2018*. Oral Presentation.

- Thompson, M.S.**, and Zega, T.J. 2015. Simulation of Micrometeorite Impacts through in situ Dynamic Heating of Lunar Soils. *Meteoritical Society Meeting Abstract* 5389. Oral Presentation.
- Thompson, M.S.**, and Zega, T.J. 2015. The Oxidation State of Nanophase Fe Particles Produced by Space Weathering as Revealed through Aberration-Corrected Transmission Electron Microscopy. *Microscopy and Microanalysis Conference Abstract* 0761. Oral Presentation.
- Thompson, M.S.**, Zega, T.J., Keane, J.T., Becerra, P. and Byrne, S. 2015. The Oxidation State of Fe Nanoparticles in Lunar Soil: Implications for Space Weathering Processes. *LPSC Abstract* 2932. Poster Presentation.
- Hyde, B.C., Tait, K.T., Rumble III, D., Izawa, M.R.M., **Thompson, M.S.**, Nicklin, I., and Gregory, D.A. 2015. Achondritic Impactor Clasts in Northwest Africa 869. *LPSC Abstract* 1983. Poster Presentation.
- Thompson, M.S.** and Zega, T.J. 2014. Electron Energy-Loss Spectroscopy of Iron Nanoparticles in Lunar Soil using an Aberration-Corrected Scanning Transmission Electron Microscope. *Microscopy and Microanalysis Abstract* 1672. Oral Presentation.
- Thompson, M.S.**, Christoffersen, R., Zega, T.J., and Keller, L.P. 2014. Nanoscale Analysis of Space Weathering Features in Soils from Itokawa. *LPSC Abstract* 2121. Oral Presentation.
- Miller, K.E., **Thompson, M.S.**, Lauretta, D.S., and Zega, T.J. 2014. Conditions for Formation of Chalcopyrite in the Rumuruti Chondrites. *LPSC Abstract* 1461. Poster Presentation.
- Thompson, M.S.** and Zega, T.J. 2014. Determining the Oxidation State of Iron Nanoparticles in Mature Lunar Soil through Electron Energy-Loss Spectroscopy. *LPSC Abstract* 2834. Poster Presentation.
- Thompson, M.S.** and Zega, T.J. 2013. Microstructural and Chemical Analysis of Soils from Itokawa: Evidence for Space Weathering. *LPSC Abstract* 2593. Poster Presentation.
- Thompson, M.S.**, Christoffersen, R., and Zega, T. J. 2013. Microchemical and Structural Evidence for Space Weathering in Soils from Itokawa. *Hayabusa Sample Symposium*. Oral Presentation.

Thompson, M.S, Miller, K.E, Zega, T.J., and Laurretta, D.S. 2012. Nanostructural Analysis of a Sulfide Assemblage in an R Chondrite Meteorite via Large Solid-Angle EDS. *Microscopy and Microanalysis Meeting Abstract*. Poster Presentation.

REFERENCES

- Alamgir F. M., Jain H., Williams D. B., and Schwarz R. B. 2003. The structure of a metallic glass system using EXELFS and EXAFS as complementary probes. *Micron* **34**: 433-439.
- Bell P., Mao H., and El Goresy A. 1974. A study of iron-rich particles on the surfaces of orange glass spheres from 74220. In *Lunar and Planetary Science Conference Proceedings*, pp. 187-191.
- Bernatowicz T. J., Nichols R. H., Hohenberg C. M., and, Maurette M. 1994. Vapor deposits in the lunar regolith. *Science* **264**:1779-1780.
- Bibring J. P., Duraud J. P., Durrieu L., Jouret C., Maurette M., and Meunier R. 1972. Ultrathin amorphous coatings on lunar dust grains. *Science* **175**:753-755.
- Binzel R. P., Bus S. J., Burbine T. H., and Sunshine J. M. 1996. Spectral properties of near-Earth asteroids: Evidence for sources of ordinary chondrite meteorites. *Science* **273**:946-948.
- Binzel R. P., Rivkin A. S., Bus S. J., Sunshine J. M., and Burbine, T. H. 2001. MUSES-C target asteroid (25143) 1998 SF36: a reddened ordinary chondrite. *Meteoritics & Planetary Science* **36**: 1167-1172.
- Blanford G., Fruland R., and Morrison D. 1975. Long-term differential energy spectrum for solar-flare iron-group particles. In *Lunar and Planetary Science Conference Proceedings*, pp. 3557-3576.
- Bødker F., Mørup S., and Linderøth S. 1994. Surface effects in metallic iron nanoparticles. *Physical Review Letters* **72**: 282.

- Bottke W. F., Nolan M. C., Greenberg R., and Kolvoord R. A. 1994. Velocity distributions among colliding asteroids. *Icarus* **107**: 255-268.
- Bradley J. P. 1988. Analysis of chondritic interplanetary dust thin-sections. *Geochimica et Cosmochimica Acta* **52**: 889-900.
- Bradley J., Dukes C., Baragiola R., McFadden L., Johnson R., and Brownlee D. 1996. Radiation processing and the origins of interplanetary dust. *Lunar and Planetary Science Conference XXVII Abstract*, pp. 149.
- Buseck P. R. and Allen F. (1992) *Minerals and reactions at the atomic scale: transmission electron microscopy*. Mineralogical Society of America.
- Cabot A., Puentes V. F., Shevchenko E., Yin Y., Balcells L., Marcus M. A., Hughes S. M., and Alivisatos A. P. 2007. Vacancy coalescence during oxidation of iron nanoparticles. *Journal of the American Chemical Society* **129**: 10358-10360.
- Cabrera N. and Mott N. 1949. Theory of the oxidation of metals. *Reports on Progress in Physics* **12**: 163-184.
- Carrez P., Demyk K., Cordier P., Gengembre L., Grimblot J., D'Hendecourt L., Jones A. P., and Leroux H. 2002. Low-energy helium ion irradiation-induced amorphization and chemical changes in olivine: Insights for silicate dust evolution in the interstellar medium. *Meteoritics and Planetary Science* **37**:1599-1614.
- Chapman C. R. 2004. Space weathering of asteroid surfaces. *Annual Reviews in Earth and Planetary Science* **32**:539-567.
- Christoffersen R., Keller L., Rahman Z., and Baragiola R. 2010. Experimental investigation of space radiation processing in lunar soil ilmenite: combining

- perspectives from surface science and transmission electron microscopy. *Lunar and Planetary Science Conference Abstracts XXXXI* Abstract 1532.
- Christoffersen R. and Keller L. P. 2011. Space radiation processing of sulfides and silicates in primitive solar systems materials: Comparative insights from in situ TEM ion irradiation experiments. *Meteoritics & Planetary Science* **46**: 950-969.
- Christoffersen R., Rahman Z., and Keller L. 2012. Solar ion sputter deposition in the lunar regolith: Experimental simulation using Focused-Ion Beam techniques. *Lunar and Planetary Science Conference XXXXIII* Abstract 2614.
- Christoffersen R., Cintala M., Keller L., See T., and Horz F. 2013. Nanoscale mineralogy and composition of experimental regolith agglutinates produced under asteroidal impact conditions. *Lunar and Planetary Science Conference Abstracts XXXXVI* Abstract 2068.
- Christoffersen R., Loeffler M., Dukes C., Keller L., and Baragiola R. 2016. Compositional and microstructural evolution of olivine under multiple-cycle pulsed laser irradiation as revealed by FIB/field-emission TEM. *Lunar and Planetary Science Conference XXXXVII* Abstract 2747.
- Christoffersen R., Loeffler M., Dukes C., Keller L., and Baragiola R. 2016. Compositional and Microstructural Evolution of Olivine Under Multiple-Cycle Pulsed Laser Irradiation as Revealed by FIB/Field-Emission TEM.
- Cintala M. 1991. A reassessment of impact melting and vaporization in the regolith of Mercury: Comparison with the Moon. *Lunar and Planetary Science Conference XXII* Abstract 209.

- Cintala M. J. 1992. Impact-induced thermal effects in the lunar and Mercurian regoliths. *Journal of Geophysical Research: Planets* **97**: 947-973.
- Cintala M., Keller L., Christoffersen R., and Hörz F. 2015. Space weathering in Houston: A role for the experimental impact laboratory at JSC. *LPI Contribution* 2061.
- Cho S.-J., Idrobo J.-C., Olamit J., Liu K., Browning N. D., and Kauzlarich S. M. 2005. Growth mechanisms and oxidation resistance of gold-coated iron nanoparticles. *Chemistry of Materials* **17**: 3181-3186.
- Clark B. E., Lucey P., Helfenstein P., Bell J. F., Peterson C., Veverka J., McConnochie T., Robinson M. S., Bussey B., Murchie S. L. and Izenberg N. I. 2001. Space weathering on Eros: Constraints from albedo and spectral measurements of Psyche crater. *Meteoritics & Planetary Science* **36**: 1617-1637.
- Clark B. E., Hapke B., Pieters C., and Britt D. (2002) *Asteroid space weathering and regolith evolution*. In Bottke W, Cellino A, Paolicchi P, and Binzel RP (ed) *Asteroids III*, Tucson, Arizona: University of Arizona Press.
- Cliff G. and Lorimer G. W. 1975. The quantitative analysis of thin specimens. *Journal of Microscopy* **103**: 203-207.
- Conel J. and Nash D. 1970. Spectral reflectance and albedo of Apollo 11 lunar samples: Effects of irradiation and vitrification and comparison with telescopic observations. *Geochimica et Cosmochimica Acta Supplement* **1**: 2013.
- Connolly Jr. H. C., Lauretta D. S., Walsh K. J., Tachibana S., and Bottke W. F. 2015. Towards understanding the dynamical evolution of asteroid 25143 Itokawa: constraints from sample analysis. *Earth, Planets and Space* **67**: 1-6.
- Cowley J. M. (1995) *Diffraction physics*. Elsevier.

- Dąbrowski A., Mendyk E., Robens E., Skrzypiec K., Goworek J., Iwan M., and Rzączyńska Z. 2008. Investigation of surface properties of lunar regolith part III. *Journal of Thermal Analysis and Calorimetry* **94**: 633-639.
- Dikov Y. P., Gerasimov M., Yakovlev O., and Ivanov A. 2009. Valence state of iron in a condensate from the Luna 16 regolith. *Petrology* **17**: 429-438.
- Dukes C., Baragiola R., and McFadden L. 1999. Surface modification of olivine by H⁺ and He⁺ bombardment. *Journal of Geophysical Research: Planets* **104**: 1865-1872.
- Egerton R. 1996. Electron energy loss in the electron microscope. *Plenum, New York* 160: 165-169.
- Forester D. 1973. Mössbauer search for ferric oxide phases in lunar materials and simulated lunar materials. In *Lunar and Planetary Science Conference Proceedings*, pp. 2697.
- Garvie L. A., Craven A. J., and Brydson R. 1994. Use of electron-energy loss near-edge fine structure in the study of minerals. *American Mineralogist* **79**: 411-425.
- Garvie L. A. and Buseck P. R. 1998. Ratios of ferrous to ferric iron from nanometre-sized areas in minerals. *Nature* **396**: 667-670.
- Garvie L. A., Zega T. J., Rez P., and Buseck P. R. 2004. Nanometer-scale measurements of Fe³⁺/ΣFe by electron energy-loss spectroscopy: A cautionary note. *American Mineralogist* **89**: 1610-1616.
- Gianuzzi L. and Stevie F. 2005. Introduction to focused ion beams. *Instrumentation, Theory, Techniques and Practice*. Springer U.S.
- Gibson Jr E. and Johnson S. M. 1971. Thermal analysis-inorganic gas release studies of lunar samples. In *Lunar and Planetary Science Conference Proceedings*, pp. 1351.

- Gillis-Davis J., Lucey P., Bradley J., Ishii H., and Connolly H. 2013. Laser Space Weathering of Allende Meteorite. *Lunar and Planetary Science Conference XXXIV* Abstract 2494.
- Gillis-Davis J., Gasda P., Bradley J., Ishii H., and Bussey D. 2015. Laser Space Weathering of Allende (CV2) and Murchison (CM2) Carbonaceous Chondrites. *Lunar and Planetary Science Conference XXXVI* Abstract 1607.
- Gold T. 1955. The lunar surface. *Monthly Notices of the Royal Astronomical Society* **115**: 585-604.
- Gold T., Campbell M., and O'leary B. 1970. Optical and high-frequency electrical properties of the lunar sample. *Geochimica et Cosmochimica Acta Supplement* **1**: 2149.
- Goldstein B., Neugebauer M., Phillips J., Bame S., Gosling J., McComas D., Wang Y.-M., Sheeley N., and Suess S. 1996. ULYSSES plasma parameters: latitudinal, radial, and temporal variations. *Astronomy and Astrophysics* **316**: 296-303.
- Green R. O., Pieters C., Mouroulis P., Eastwood M., Boardman J., Glavich T., Isaacson P., Annadurai M., Besse S., Barr D., Buratti B., Cate D., Chatterjee A., Clark R., Cheek L., Combe J., Dhingra D., Essandoh V., Geier S., Goswami J. N., Green R., Haemmerle V., Head J., Hovland L., Hyman S., Klima R., Koch T., Kramer G., Kumar A. S. K., Lee K., Lundeen S., Malaret E., McCord T., McLaughlin S., Mustard J., Nettles J., Petro N., Plourde K., Racho C., Rodriguez J., Runyon C., Sellar G., Smith C., Sobel H., Staid M., Sunshine J., Taylor L., Thaisen K., Tompkins S., Tseng H., Vane G., Varanasi P., White M., and Wilson D. 2011. The Moon Mineralogy Mapper (M³) imaging spectrometer for lunar science: Instrument

- description, calibration, on-orbit measurements, science data calibration and on-orbit validation. *Journal of Geophysical Research: Planets* **116**: E00G19.
- Griscom D. 1974. Ferromagnetic resonance spectra of lunar fines: some implications of line shape analysis. *Geochimica et Cosmochimica Acta* **38**: 1509-1519.
- Griscom D. and Marquardt C. 1972. Evidence of lunar surface oxidation processes: Electron spin resonance spectra of lunar materials and simulated lunar materials. In *Lunar and Planetary Science Conference Proceedings*, pp. 2397.
- Grün E., Fechtig H., Hanner M., Kissel J., Lindblad B.-A., Linkert D., Morfill G., and Zook H. (1991) In-situ exploration of dust in the solar system and initial results from the Galileo Dust Detector. In *Origin and Evolution of Interplanetary Dust*, 21-28. Springer.
- Hapke B., Cohen A., Cassidy W., and Wells E. 1970. Solar radiation effects on the optical properties of Apollo 11 samples. *Geochimica et Cosmochimica Acta Supplement* **1**: 2199.
- Hapke B., Cassidy W., and Wells E. 1975. Effects of vapor-phase deposition processes on the optical, chemical, and magnetic properties of the lunar regolith. *The Moon* **13**: 339-353.
- Hapke B. 2001. Space weathering from Mercury to the asteroid belt. *Journal of Geophysical Research: Planets* **106**: 10039-10073.
- Hapke B. (2012) *Theory of reflectance and emittance spectroscopy*. Cambridge University Press.
- Heiken G., Vaniman D., and French B. M. (1991) *Lunar sourcebook: A user's guide to the Moon*. Cambridge University Press.

- Henning T., Begemann B., Mutschke H., and Dorschner J. 1995. Optical properties of oxide dust grains. *Astronomy and Astrophysics Supplement Series* **112**: 143.
- Hiroi T., Abe M., Kitazato K., Abe S., Clark B.E., Sasaki S., Ishiguro M., and Barnouin-Jha O.S. 2006. Developing space weathering on the asteroid 25143 Itokawa. *Nature* **443**:56-58.
- Hishmeh G., Cartz L., Desage F., Templier C., Desoyer J., and Birtcher R. 1994. Rare gas bubbles in muscovite mica implanted with xenon and krypton. *Journal of Materials Research* **9**:3095-3107.
- Housley R., Grant R., and Paton N. 1973. Origin and characteristics of excess Fe metal in lunar glass welded aggregates. In *Lunar and Planetary Science Conference Proceedings*, pp. 2737.
- Housley R., Cirlin E., Paton N., and Goldberg I. 1974. Solar wind and micrometeorite alteration of the lunar regolith. In *Lunar and Planetary Science Conference Proceedings*, pp. 2623-2642.
- Johnson P. and Christy R. 1974. Optical constants of transition metals: Ti, V, Cr, Mn, Fe, Co, Ni, and Pd. *Physical Review B* **9**: 5056.
- Joy K. H., Visscher C., Zolensky M. E., Mikouchi T., Hagiya K., Ohsumi K., and Kring D. A. 2015. Identification of magnetite in lunar regolith breccia 60016: Evidence for oxidized conditions at the lunar surface. *Meteoritics & Planetary Science* **50**: 1157-1172.
- Keane J. and Matsuyama I. 2013. Hill Slope Failure as a Mechanism to Resurface Asteroids During Planetary Flybys. In *AAS:Division for Planetary Sciences Meeting Abstracts*.

- Keller L. P. and McKay D. S. 1993. Discovery of vapor deposits in the lunar regolith. *Science* **261**: 1305-1307.
- Keller L. P. and McKay D. 1995. The origin of amorphous rims on lunar soil grains-revisited. *Meteoritics* **30**: 526.
- Keller L. P. and McKay D. S. 1997. The nature and origin of rims on lunar soil grains. *Geochimica et Cosmochimica Acta* **61**: 2331-2341.
- Keller L. P., Wentworth S., and McKay D. S. 1998. Space Weathering: Reflectance spectroscopy and TEM analysis of individual lunar soil grains. *Lunar and Planetary Science Conference XXIX* Abstract 1762.
- Keller L. and Clemett S. J. 2001. Formation of nanophase iron in the lunar regolith. In *Lunar and Planetary Conference XXXII* Abstract 2097.
- Keller L. P. and Berger E. L. 2014. A transmission electron microscope study of Itokawa regolith grains. *Earth, Planets and Space* **66**: 1-7.
- Keller L. P., Christoffersen R., Dukes C., Baragiola R., and Rahman Z. 2015. Ion irradiation experiments on the Murchison CM2 carbonaceous chondrite: Simulating space weathering of primitive asteroids. *Lunar and Planetary Science Conference XXXXVI* Abstract 1913.
- Keller L. P., Berger E., Christoffersen R., and Zhang S. 2016. Direct determination of the space weathering rates in lunar soils and Itokawa regolith from sample analyses. *Lunar and Planetary Science Conference XXXXVII* Abstract 2525.
- Kolopus J., Kline D., Chatelain A., and Weeks R. 1971. Magnetic resonance properties of lunar samples: mostly Apollo 12. In *Lunar and Planetary Science Conference Proceedings*, pp. 2501.

- Krivanek O. L., Dellby N., Murfitt M. F., Chisholm M. F., Pennycook T. J., Suenaga K., and Nicolosi V. 2010. Gentle STEM: ADF imaging and EELS at low primary energies. *Ultramicroscopy* **110**: 935-945.
- Li R., Ye Z., Kong W., Wu H., Lin X., and Fang W. 2015. Controllable synthesis and growth mechanism of dual size distributed PbSe quantum dots. *RSC Advances* **5**: 1961-1967.
- Liu Y, Guan Y., Zhang Y., Rossman G. R., Eiler J. M., and Taylor L. A. 2012. Direct measurement of hydroxyl in the lunar regolith and the origin of lunar surface water. *Nature Geoscience* **5**: 779-782.
- Loeffler M., Dukes C., and Baragiola R. 2009. Irradiation of olivine by 4 keV He⁺: Simulation of space weathering by the solar wind. *Journal of Geophysical Research: Planets* **114**: E03003.
- Lucey P. G., Blewett D. T., Taylor G. J., and Hawke B. 2000. Imaging of lunar surface maturity. *Journal of Geophysical Research: Planets*: **105**: 20377-20386.
- Lucey P. G. and Noble S. K. 2008. Experimental test of a radiative transfer model of the optical effects of space weathering. *Icarus* **197**: 348-353.
- Matsumoto T., Tsuchiyama A., Miyake A., Noguchi T., Nakamura M., Uesugi K., Takeuchi A., Suzuki Y., and Nakano T. 2015a. Surface and internal structures of a space-weathered rim of an Itokawa regolith particle. *Icarus* **257**: 230-238.
- Matsumoto T., Tsuchiyama A., Watanabe N., Yasuda K., Miyake A., Nakauchi Y., Okada T., Abe M., Yada T., and Uesugi M. 2015b. Systematic ion irradiation experiments to olivine: Comparison with space weathered rims of Itokawa regolith particles. *LPI Contributions* 2045.

- Matsuno J., Miyake A., Tsuchiyama A., Messenger S., and Nakamura-Messenger K. 2015. Complete TEM-Tomography: 3D Structure of GEMS Cluster. *Lunar and Planetary Science Conference XXXXVI* Abstract 2177.
- Matsuoka M., Nakamura T., Kimura Y., Hiroi T., Nakamura R., Okumura S., and Sasaki S. 2015. Pulse-laser irradiation experiments of Murchison CM2 chondrite for reproducing space weathering on C-type asteroids. *Icarus* 254: 135-143.
- McFadden L.-A., Johnson T., and Weissman P. (2006) *Encyclopedia of the solar system*. Academic Press.
- McKay D. S., Heiken G., Basu A., Blanford G., Simon S., Reedy R., French B. M., and Papike J. J. (1991) The lunar regolith. In *Lunar Sourcebook: A User's Guide to the Moon* (ed. G. Heiken et al.), pp. 285-356. Cambridge University Press.
- Menke W. 2012. *Geophysical Data Analysis: Discrete Inverse Theory*. Academic Press.
- Morris R. 1978. The surface exposure/maturity/of lunar soils-Some concepts and I_s/FeO compilation. *Lunar and Planetary Science Conference Proceedings*, pp. 2287-2297.
- Morris R. 1980. Origins and size distribution of metallic iron particles in the lunar regolith. *Lunar and Planetary Science Conference Proceedings*, pp. 1697-1712.
- Muller D., Kourkoutis L. F., Murfitt M., Song J., Hwang H., Silcox J., Dellby N., and Krivanek O. 2008. Atomic-scale chemical imaging of composition and bonding by aberration-corrected microscopy. *Science* **319**: 1073-1076.
- Nakamura T., Noguchi T., Tanaka M., Zolensky M. E., Kimura M., Tsuchiyama A., Nakato A., Ogami T., Ishida H., Uesugi M., Yada T., Shirai K., Fujimura A., Okazaki R., Sandford S. A., Ishibashi Y., Abe M., Okada T., Ueno M., Mukai T.,

- Yoshikawa M., and Kawaguchi J. 2011. Itokawa dust particles: A direct link between S-Type asteroids and ordinary chondrites. *Science* **333**:1113-1116.
- Nakashima D., Kita N. T., Ushikubo T., Noguchi T., Nakamura T., and Valley J. W. 2013. Oxygen three-isotope ratios of silicate particles returned from asteroid Itokawa by the Hayabusa spacecraft: A strong link with equilibrated LL chondrites. *Earth and Planetary Science Letters* **379**:127-136.
- Noble S. K., and Pieters C. 2003. Space weathering on Mercury: Implications for remote sensing. *Solar System Research* **37**: 31-35.
- Noble S. K., Keller L. P., and Pieters C. M. 2005. Evidence of space weathering in regolith breccias I: Lunar regolith breccias. *Meteoritics & Planetary Science* **40**: 397-408.
- Noble S. K., Pieters C. M., and Keller L. P. 2007. An experimental approach to understanding the optical effects of space weathering. *Icarus* **192**: 629-642.
- Noble S. K., Keller L. P., and Pieters C. M. 2011. Evidence of space weathering in regolith breccias II: asteroidal regolith breccias. *Meteoritics & Planetary Science* **45**: 2007-2015.
- Noguchi T., Nakamura T., Kimura M., Zolensky M. E., Tanaka M., Hashimoto T., Konno M., Nakato A., Ogami T., Fujimura A., Abe M., Yada T., Mukai T., Ueno M., Okada T., Shirai K., Ishibashi Y., and Okazaki R. 2011. Incipient Space Weathering Observed on the Surface of Itokawa Dust Particles. *Science* **333**: 1121-1125.
- Noguchi T., Kimura M., Hashimoto T., Konno M., Nakamura T., Zolensky M. E., Okazaki R., Tanaka M., Tsuchiyama A., Nakato A., Ogami T., Ishida H., Sagae R., Tsujimoto S., Matsumoto T., Matsuno J., Fujimura A., Abe M., Yada T., Mukai T., Ueno M., Okada T., Shirai K., and Ishibashi Y. 2014. Space weathered rims found

- on the surfaces of the Itokawa dust particles. *Meteoritics & Planetary Science* **49**: 188-214.
- Papike J., Simon S., White C., and Laul J. 1982. The relationship of the lunar regolith less than 10 micrometer fraction and agglutinates. I-A model for agglutinate formation and some indirect supportive evidence. In *Lunar and Planetary Science Conference Proceedings*, pp. 409-420.
- Pasieczna-Patkowska S., Dąbrowski A., Robens E., and Ryczkowski J. 2008. FT-IR/PAS studies of lunar regolith samples. *Acta Physica Polonica A. Optical and Acoustical Methods in Science and Technology* **114**:A163–A168.
- Pieters C. M., Taylor L. A., Noble S. K., Keller L. P., Hapke B., Morris R. V., Allen C. C., McKay D. S., and Wentworth S. 2000. Space weathering on airless bodies: Resolving a mystery with lunar samples. *Meteoritics & Planetary Science* **35**: 1101-1107.
- Ramdohr P. and El Goresey A. 1970. Opaque minerals of the lunar rocks and dust from Mare Tranquillitatis. *Science* **167**: 615-618.
- Ratke L. and Voorhees P. W. (2013) *Growth and coarsening: Ostwald ripening in material processing*. Springer Science & Business Media.
- Robinson M. S., Brylow S. M., Tschimmel D., Humm D., Lawrence S. J., Thomas P. C., Denevi B. W., Bowman-Cisneros E., Zerr J., Ravine M. A., Caplinger M. A., Ghaemi F. T., Schaffner J. A., Malin M.C., Mahanti P., Bartels A., Anderson J., Tran T. N., Eliason E. M., McEwen A. S., Turtle E., Jolliff B. L. and Hiesinger H. 2010. Lunar reconnaissance orbiter camera (LROC) instrument overview. *Space Science Reviews* **150**: 81-124.

- Roy S., Roy B., and Chakravorty D. 1996. Magnetic properties of iron nanoparticles grown in a glass matrix. *Journal of Applied Physics* **79**: 1642-1645.
- Runcorn S., Collinson D., O'Reilly W., Stephenson A., Battey M., Manson A., and Readman P. 1971. Magnetic properties of Apollo 12 lunar samples. *Proceedings of the Royal Society* **3258**:157-174.
- Sasaki S., Nakamura K., Hamabe Y., Kurahashi E., and Hiroi T. 2001. Production of iron nanoparticles by laser irradiation in a simulation of lunar-like space weathering. *Nature* **410**: 555-557.
- Shearer C., Sharp Z., Burger P., McCubbin F., Provencio P., Brearley A., and Steele A. 2014. Chlorine distribution and its isotopic composition in “rusty rock” 66095. Implications for volatile element enrichments of “rusty rock” and lunar soils, origin of “rusty” alteration, and volatile element behavior on the Moon. *Geochimica et Cosmochimica Acta* **139**: 411-433.
- Tanaka T. 1979. Optical constants of polycrystalline 3d transition metal oxides in the wavelength region 350 to 1200 nm. *Japanese Journal of Applied Physics* **18**: 1043.
- Triaud A. H. M. J. Database of Optical Constants for Cosmic Dust. Date Accessed: April 27, 2015. <http://www.astro.uni-jena.de/Laboratory/OCDB/oxsul.html>.
- Taylor L. A., Pieters C. M., Keller L. P., Morris R. V., and McKay D. S. 2001. Lunar mare soils: Space weathering and the major effects of surface-correlated nanophase Fe. *Journal of Geophysical Research: Planets* **106**: 27985-27999.
- Thompson M. S., Christoffersen R., Zega T. J., and Keller L. P. 2014. Microchemical and structural evidence for space weathering in soils from asteroid Itokawa. *Earth, Planets and Space* **66**: 1-10.

- Thompson M. S. and Zega T. J. 2015. The Oxidation State of Nanophase Fe Particles Produced by Space Weathering as Revealed Through Aberration-Corrected Transmission Electron Microscopy. *Microscopy and Microanalysis* **21**: 1525-1526.
- Thompson M. S., Zega T. J., Becerra P., Keane J. T., and Byrne S. 2016. The Oxidation State of Nanophase Fe Particles in Lunar Soil: Implications for Space Weathering. *Meteoritics and Planetary Science* (accepted).
- van Aken P., Liebscher B., and Styrsa V. 1998. Quantitative determination of iron oxidation states in minerals using Fe $L_{2,3}$ -edge electron energy-loss near-edge structure spectroscopy. *Physics and Chemistry of Minerals* **25**: 323-327.
- van Aken P., Styrsa V., Liebscher B., Woodland A., and Redhammer G. 1999. Microanalysis of $\text{Fe}^{3+}/\Sigma\text{Fe}$ in oxide and silicate minerals by investigation of electron energy-loss near-edge structures (ELNES) at the Fe $M_{2,3}$ edge. *Physics and Chemistry of Minerals* **26**: 584-590.
- Varela M., Oxley M., Luo W., Tao J., Watanabe M., Lupini A. R., Pantelides S., and Pennycook S. 2009. Atomic-resolution imaging of oxidation states in manganites. *Physical Review B* **79**: 085117.
- Vasavada, A.R., Bandfield, J.L., Greenhagen, B.T., Hayne, P.O., Siegler, M.A., Williams, J.P. and Paige, D.A. 2012. Lunar equatorial surface temperatures and regolith properties from the Diviner Lunar Radiometer Experiment. *Journal of Geophysical Research: Planets* **117**: E12.
- Wang L. M., and Ewing R. C. 1992. Ion-beam-induced amorphization of complex ceramic materials—minerals. *Materials Science Research Bulletin* **17**:38-44.

- Wang S. X., Wang L. M., Ewing R. C., and Doremus R. H. 1998a. Ion beam-induced amorphization in MgO–Al₂O₃–SiO₂. I. Experimental and theoretical basis. *Journal of Non-Crystalline Solids* **238**:198-213.
- Wang S. X., Wang L. M., Ewing R. C., and Doremus R. H. 1998b. Ion beam-induced amorphization in MgO–Al₂O₃–SiO₂. II. Empirical model. *Journal of Non-Crystalline Solids* **238**:214-224.
- Weeks R., Kolopus J., Kline D., and Chatelain A. 1970. Apollo 11 lunar material: nuclear magnetic resonance of ²⁷Al and electron resonance of Fe and Mn. *Geochimica et Cosmochimica Acta Supplement* **1**: 2467.
- Weeks R. 1972. Magnetic phases in lunar material and their electron magnetic resonance spectra: Apollo 14. In *Lunar and Planetary Science Conference Proceedings*, pp. 2503.
- Williams D. and Carter C. 1996. *Transmission Electron Microscopy: A Textbook for Material Science*. Plenum Press.
- Yakovlev O., Dikov Y. P., and Gerasimov M. 2009. Effect of the disproportionation reaction of ferrous iron in impact-evaporation processes. *Geochemistry International* **47**: 134-142.
- Yamada M., Sasaki S., Nagahara H., Fujiwara A., Hasegawa S., Yano H., Hiroi T., Ohashi H., and Otake H. 1999. Simulation of space weathering of planet-forming materials: Nanosecond pulse laser irradiation and proton implantation on olivine and pyroxene samples. *Earth Planets and Space* **51**: 1255-1265.
- Yurimoto H., Abe K.-I., Abe M., Ebihara M., Fujimura A., Hashiguchi M., Hashizume K., Ireland T. R., Itoh S., and Katayama J. 2011. Oxygen isotopic compositions of

asteroidal materials returned from Itokawa by the Hayabusa mission. *Science* **333**:1116-1119.

Zega T. J. 2003. Transmission electron microscopy and electron energy-loss spectroscopy of fine-grained materials in primitive meteorites. *Dissertation, Arizona State University*.

Zega T. J., Garvie L. A., and Buseck P. R. 2003. Nanometer-scale measurements of iron oxidation states of cronstedtite from primitive meteorites. *American Mineralogist* **88**: 1169-1172.

Zega T. J., Nittler L. R., Busemann H., Hoppe P., and Stroud R. M. 2007. Coordinated isotopic and mineralogic analyses of planetary materials enabled by in situ lift-out with a focused ion beam scanning electron microscope. *Meteoritics & Planetary Science* **42**: 1373-1386.

Zhang S. and Keller L. P. 2010. Formation of ilmenite rims in lunar soils: Vapor deposition, irradiation and thermal effects. *Lunar and Planetary Science Conference XXXXI* Abstract 1432.

Zhang S., and Keller L. P. 2012. Rates of space weathering in lunar regolith grains. *Meteoritical Society Meeting LXXV* Abstract 5267.

Ziegler JF, Biersack JP, Ziegler MD (2008) *SRIM, the stopping and range of ions in matter*. Lulu press.

Zolensky M. E., Zega T. J., Yano H., Wirick S., Westphal A. J., Weisberg M. K., Weber I., Warren J. L., Velbel M. A., Tsuchiyama A., Tsou P., Toppani A., Toka N., Tomeoka K., Teslich N., Taheri M., Susini J., Stroud R., Stephan T., Stadermann F. J., Snead C. J., Simon S. B., Simionovici A., See T. H., Robert F., Rietmeijer F.

J. M., Rao W., Perronnet M. C., Papanastassiou D. A., Okudaira K., Ohsumi K., Ohnishi I., Nakamura-Messenger K., Nakamura T., Mostefaoui S., Mikouchi T., Meibom A., Matrajt G., Marcus M. A., Leroux H., Lemelle L., Le L., Lanzirotti A., Langenhorst F., Krot A. N., Keller L. P., Kearsley A. T., Joswiak D., Jacob D., Ishii H., Harvey R., Hagiya K., Grossman L., Grossman J. N., Graham G. A., Gounelle M., Gillet P., Genge M. J., Flynn G., Ferroir T., Fallon S., Ebel D. S., Dai Z. R., Cordier P., Clark B., Chi M., Butterworth A. L., Brownlee D. E., Bridges J. C., Brennan S., Brearley A., Bradley J. P., Bleuet P., Bland P. A., and Bastien R. 2006. Mineralogy and petrology of Comet 81P/Wild 2 nucleus samples. *Science* **314**:1735-1739.

Zolensky M., Nakamura-Messenger K., Fletcher L., and See T. 2008. Curation, spacecraft recovery, and preliminary examination for the Stardust mission: A perspective from the curatorial facility. *Meteoritics & Planetary Science* **43**: 5-21.